NUREG/CR-0126
ORNL/NUREG/TM-196

Crack Extension and Arrest Tests of Axially Flawed Steel Model Pressure Vessels

G. C. Smith
P. P. Holz
W. J. Stelzman

Prepared for the U.S. Nuclear Regulatory Commission
Office of Nuclear Regulatory Research
Under Interagency Agreements DOE 40-551-75 and 40-552-75

OAK RIDGE NATIONAL LABORATORY
OPERATED BY UNION CARBIDE CORPORATION · FOR THE DEPARTMENT OF ENERGY

Printed in the United States of America. Available from
National Technical Information Service
U.S. Department of Commerce
5285 Port Royal Road, Springfield, Virginia 22161

NUREG/CR-0126
ORNL/NUREG/TM-196
Dist. Category R5

Contract No. W-7405-eng-26

Engineering Technology Division

CRACK EXTENSION AND ARREST TESTS OF AXIALLY FLAWED STEEL MODEL PRESSURE VESSELS

G. C. Smith P. P. Holz
W. J. Stelzman

Manuscript Completed — September 22, 1978
Date Published — October 1978

Prepared for the
U.S. Nuclear Regulatory Commission
Office of Nuclear Regulatory Research
Washington, D.C. 20555
Under Interagency Agreements DOE 40-551-75 and 40-552-75

NRC FIN No. B0119

Prepared by the
OAK RIDGE NATIONAL LABORATORY
Oak Ridge, Tennessee 37830
operated by
UNION CARBIDE CORPORATION
for the
DEPARTMENT OF ENERGY

CONTENTS

FOREWORD

The work reported here was performed primarily at Oak Ridge National Laboratory (ORNL) under sponsorship of the U.S. Nuclear Regulatory Commission's (NRC's) Heavy-Section Steel Technology (HSST) Program, which is directed by ORNL. The program is conducted as part of the ORNL Pressure Vessel Technology Program, of which G. D. Whitman is manager. The manager for the NRC is E. K. Lynn.

This report is designated Heavy-Section Steel Technology Program Technical Report No. 50. Prior reports in this series are listed below.

1. S. Yukawa, *Evaluation of Periodic Proof Testing and Warm Prestressing Procedures for Nuclear Reactor Vessels*, HSSTP-TR-1, General Electric Company, Schenectady, N.Y. (July 1, 1969).
2. L. W. Loechel, *The Effect of Section Size on the Transition Temperature in Steel*, MCR-69-189, Martin Marietta Corporation, Denver, Colo. (Nov. 20, 1969).
3. P. N. Randall, *Gross Strain Measure of Fracture Toughness of Steels*, HSSTP-TR-3, TRW Systems Group, Redondo Beach, Calif. (Nov. 1, 1969).
4. C. Visser, S. E. Gabrielse, and W. VanBuren, *A Two-Dimensional Elastic-Plastic Analysis of Fracture Test Specimens*, WCAP-7368, Westinghouse Electric Corporation, PWR Systems Division, Pittsburgh, Pa. (October 1969).
5. T. R. Mager, F. O. Thomas, and W. S. Hazelton, *Evaluation by Linear Elastic Fracture Mechanics of Radiation Damage to Pressure Vessel Steels*, WCAP-7328 (Rev.), Westinghouse Electric Corporation, PWR Systems Division, Pittsburgh, Pa. (October 1969).
6. W. O. Shabbits, W. H. Pryle, and E. T. Wessel, *Heavy-Section Fracture Toughness Properties of A533, Grade B, Class 1 Steel Plate and Submerged Arc Weldment*, WCAP-7414, Westinghouse Electric Corporation, PWR Systems Division, Pittsburgh, Pa. (December 1969).
7. F. J. Loss, *Dynamic Tear Test Investigations of the Fracture Toughness of Thick-Section Steel*, NRL-7056, U.S. Naval Research Laboratory, Washington, D.C. (May 14, 1970).
8. P. B. Crosley and E. J. Ripling, *Crack Arrest Fracture Toughness of A533, Grade B, Class 1 Pressure Vessel Steel*, HSSTP-TR-8, Materials Research Laboratory, Inc., Glenwood, Ill. (March 1970).
9. T. R. Mager, *Post-Irradiation Testing of 2 T Compact Tension Specimens*, WCAP-7561, Westinghouse Electric Corporation, PWR Systems Division, Pittsburgh, Pa. (August 1970).
10. T. R. Mager, *Fracture Toughness Characterization Study of A533, Grade B, Class 1 Steel*, WCAP-7578, Westinghouse Electric Corporation, PWR Systems Division, Pittsburgh, Pa. (October 1970).

11. T. R. Mager, *Notch Preparation in Compact Tension Specimens*, WCAP-7579, Westinghouse Electric Corporation, PWR Systems Division, Pittsburgh, Pa. (November 1970).

12. N. Levy and P. V. Marcal, *Three-Dimensional Elastic-Plastic Stress and Strain Analysis for Fracture Mechanics, Phase I: Simple Flawed Specimens*, HSSTP-TR-12, Brown University, Providence, R.I. (December 1970).

13. W. O. Shabbits, *Dynamic Fracture Toughness Properties of Heavy-Section A533, Grade B, Class 1 Steel Plate*, WCAP-7623, Westinghouse Electric Corporation, PWR Systems Division, Pittsburgh, Pa. (December 1970).

14. P. N. Randall, *Gross Strain Crack Tolerance of A533-B Steel*, HSSTP-TR-14, TRW Systems Group, Redondo Beach, Calif. (May 1, 1971).

15. H. T. Corten and R. H. Sailors, *Relationship between Material Fracture Toughness Using Fracture Mechanics and Transition Temperature Tests*, T&AM Report 346, University of Illinois, Urbana, Ill. (Aug. 1, 1971).

16. T. R. Mager and V. J. McLoughlin, *The Effect of an Environment of High-Temperature Primary Grade Nuclear Reactor Water on the Fatigue Crack Growth Characteristics of A533, Grade B, Class 1 Plate and Weldment Material*, WCAP-7776, Westinghouse Electric Corporation, PWR Systems Division, Pittsburgh, Pa. (October 1971).

17. N. Levy and P. V. Marcal, *Three-Dimensional Elastic-Plastic Stress and Strain Analysis for Fracture Mechanics, Phase II: Improved Modeling*, HSSTP-TR-17, Brown University, Providence, R.I. (November 1971).

18. S. C. Grigory, *Six-Inch-Thick Flawed Tensile Tests, First Technical Summary Report, Longitudinal Specimens 1 through 7*, HSSTP-TR-18, Southwest Research Institute, San Antonio, Tex. (June 1972).

19. P. N. Randall, *Effects of Strain Gradients on the Gross Strain Crack Tolerance of A533-B Steel*, HSSTP-TR-19, TRW Systems Group, Redondo Beach, Calif. (May 1, 1972).

20. S. C. Grigory, *Tests of Six-Inch-Thick Flawed Tensile Specimens, Second Technical Summary Report, Transverse Specimens Numbers 8 through 10, Welded Specimens Numbers 11 through 13*, HSSTP-TR-20, Southwest Research Institute, San Antonio, Tex. (June 1972).

21. L. A. James and J. A. Williams, *Heavy-Section Steel Technology Program Technical Report No. 21, The Effect of Temperature and Neutron Irradiation upon the Fatigue-Crack Propagation Behavior of ASTM A533, Grade B, Class 1 Steel*, HEDL-TME-72-132, Hanford Engineering Development Laboratory, Richland, Wash. (September 1972).

22. S. C. Grigory, *Tests of Six-Inch-Thick Flawed Tensile Specimens, Third Technical Summary Report, Longitudinal Specimens Numbers 14 through 16, Unflawed Specimen Number 17*, HSSTP-TR-22, Southwest Research Institute, San Antonio, Tex. (October 1972).

23. S. C. Grigory, *Tests of Six-Inch-Thick Flawed Tensile Specimens, Fourth Technical Summary Report, Tests of One-Inch-Thick Flawed Tensile Specimens for Size Effect Evaluation*, HSSTP-TR-23, Southwest Research Institute, San Antonio, Tex. (June 1973).

24. S. P. Ying and S. C. Grigory, *Tests of Six-Inch-Thick Tensile Specimens, Fifth Technical Summary Report, Acoustic Emission Monitoring of One-Inch and Six-Inch-Thick Tensile Specimens*, HSSTP-TR-24, Southwest Research Institute, San Antonio, Tex. (November 1972).

25. R. W. Derby et al., *Test of 6-Inch-Thick Pressure Vessels. Series 1: Intermediate Test Vessels V-1 and V-2*, ORNL-4895, Oak Ridge National Laboratory, Oak Ridge, Tenn. (February 1974).

26. W. J. Stelzman and R. G. Berggren, *Radiation Strengthening and Embrittlement in Heavy-Section Plates and Welds*, ORNL-4871, Oak Ridge National Laboratory, Oak Ridge, Tenn. (June 1973).

27. P. B. Crosley and E. J. Ripling, *Crack Arrest in an Increasing K-Field*, HSSTP-TR-27, Materials Research Laboratory, Glenwood, Ill. (January 1973).

28. P. V. Marcal, P. M. Stuart, and R. S. Bettes, *Elastic-Plastic Behavior of a Longitudinal Semi-Elliptical Crack in a Thick Pressure Vessel*, Brown University, Providence, R.I. (June 1973).

29. W. J. Stelzman, *Characterization of HSST Plates 01, 02, and 03*, Oak Ridge National Laboratory, Oak Ridge, Tenn. (in preparation).

30. D. A. Canonico, *Characterization of Heavy-Section Weldments in Pressure Vessel Steels*, Oak Ridge National Laboratory, Oak Ridge, Tenn. (in preparation).

31. J. A. Williams, *The Irradiation and Temperature Dependence on Tensile and Fracture Properties of ASTM A533, Grade B, Class 1 Steel Plate and Weldment*, HEDL-TME 73-75, Hanford Engineering Development Laboratory, Richland, Wash. (August 1973).

32. J. M. Steichen and J. A. Williams, *High Strain Rate Tensile Properties of Irradiated ASTM A533, Grade B, Class 1 Pressure Vessel Steel*, HEDL-TME 73-7[illegible], Hanford Engineering Development Laboratory, Richland, Wash. (July 1973).

33. P. C. Riccardella and J. L. Swedlow, *A Combined Analytical-Experimental Fracture Study*, WCAP-8224, Westinghouse Electric Corporation, PWR Systems Division, Pittsburgh, Pa. (October 1973).

34. R. J. Podlasek and R. J. Eiber, *Final Report on Investigation of Mode III Crack Extension in Reactor Piping*, Battelle Columbus Laboratories, Columbus, Ohio (May 1974).

35. T. R. Mager et al., *Interim Report on the Effect of Low Frequencies on the Fatigue Crack Growth Characteristics of A533, Grade B, Class 1 Plate in an Environment of High-Temperature Primary Grade Nuclear Reactor Water*, WCAP-8256, Westinghouse Electric Corporation, Pittsburgh, Pa. (December 1973).

36. J. A. Williams, *The Irradiated Fracture Toughness of ASTM A533, Grade B, Class 1 Steel Measured with a Four-Inch-Thick Compact Tension Specimen*, HEDL-TME 75-10, Hanford Engineering Development Laboratory, Richland, Wash. (January 1975).

37. R. H. Bryan, J. G. Merkle, M. N. Rattenberg, G. C. Robinson, and J. E. Smith, *Test of 6-in.-Thick Pressure Vessels, Series 2: Intermediate Test Vessels V-3, V-4, and V-6*, ORNL-5059, Oak Ridge National Laboratory, Oak Ridge, Tenn. (November 1975).

38. T. R. Mager, S. E. Yanichko, and L. R. Singer, *Fracture Toughness Characterization of HSST Intermediate Pressure Vessel Material*, WCAP-8456, Westinghouse Electric Corporation, Pittsburgh, Pa. (December 1974).

39. J. G. Merkle, G. D. Whitman, and R. H. Bryan, *An Evaluation of the HSST Program Intermediate Pressure Vessel Tests in Terms of Light-Water-Reactor Pressure Vessel Safety*, ORNL/TM-5090, Oak Ridge National Laboratory, Oak Ridge, Tenn. (November 1975).

40. J. G. Merkle, G. C. Robinson, P. P. Holz, J. E. Smith, and R. H. Bryan, *Test of 6-In.-Thick Pressure Vessels. Series 3: Intermediate Test Vessel V-7*, ORNL/NUREG-1, Oak Ridge National Laboratory, Oak Ridge, Tenn. (August 1976).

41. J. A. Davidson, L. J. Cheschini, R. P. Shogan, and G. V. Rao, *The Irradiated Dynamic Fracture Toughness of ASTM A533, Grade B, Class 1 Steel Plate and Submerged-Arc Weldment*, WCAP-8775, Westinghouse Electric Corporation, Pittsburgh, Pa. (October 1976).

42. R. D. Cheverton, *Pressure Vessel Fracture Studies Pertaining to a PWR LOCA-ECC Thermal Shock: Experiments TSE-1 and TSE-2*, ORNL/NUREG/TM-3, Oak Ridge National Laboratory, Oak Ridge, Tenn. (September 1976).

43. J. G. Merkle et al., *Test of 6-Inch-Thick Pressure Vessels. Series 4: Intermediate Test Vessels V-5 and V-9*, ORNL/NUREG-7, Oak Ridge National Laboratory, Oak Ridge, Tenn. (August 1977).

44. J. A. Williams, *The Ductile Fracture Toughness of Heavy-Section Steel Plate*, Hanford Engineering Development Laboratory, Richland, Wash. (in preparation).

45. R. H. Bryan et al., *Test of 6-In.-Thick Pressure Vessels. Series 3: Intermediate Test Vessel V-7A under Sustained Loading*, ORNL/NUREG-9, Oak Ridge National Laboratory, Oak Ridge, Tenn. (February 1978).

46. R. D. Cheverton and S. E. Bolt, *Pressure Vessel Fracture Studies Pertaining to a PWR LOCA-ECC Thermal Shock: Experiments TSE-3 and TSE-4, and Update of TSE-1 and TSE-2 Analysis*, ORNL/NUREG-22, Oak Ridge National Laboratory, Oak Ridge, Tenn. (December 1977).

47. D. A. Canonico, *Significance of Reheat Cracks to the Integrity of Pressure Vessels for Light-Water Reactors*, ORNL/NUREG-15, Oak Ridge National Laboratory, Oak Ridge, Tenn. (July 1977).

48. G. C. Smith and P. P. Holz, *Repair Weld Induced Residual Stresses in Thick-Walled Steel Pressure Vessels*, ORNL/NUREG/TM-153, Oak Ridge National Laboratory, Oak Ridge, Tenn. (in preparation).

49. P. P. Holz and S. W. Wismer, *Half-Bead (Temper) Repair Welding for HSST Vessels*, ORNL/NUREG/TM-177, Oak Ridge Nation ` Laboratory, Oak Ridge, Tenn. (in preparation).

ACKNOWLEDGMENTS

The authors wish to thank J. W. Dally and T. Kobayashi of the University of Maryland for their assistance in evaluating strain gages as crack extension indicators. We are also indebted to G. Greene for instrumentation advice and assistance and to R. Crouse for preparing the scanning electron micrographs included in this report. A note of thanks also goes to R. H. Bryan, J. G. Merkle, and D. A. Canonico for their many helpful suggestions and stimulating discussions.

CRACK EXTENSION AND ARREST TESTS OF AXIALLY FLAWED STEEL MODEL PRESSURE VESSELS

G. C. Smith P. P. Holz
W. J. Stelzman

ABSTRACT

Three essentially identical steel pressure vessel models 254 mm (10 in.) in diameter, 38 mm (1.5 in.) in wall thickness, and containing long, through-the-wall machined and sharpened axial flaws were tested to failure at different test temperatures. The principal objective of the tests was to assess the adequacy of a particular design configuration for additional larger-scale tests. The goal of achieving both arrest and nonarrest of a rapidly propagating crack in a pressurized vessel configuration was met, with qualifications. The results suggest that design modifications should be considered for further testing.

The vessels consisted of cylindrical sections joined together by electron-beam welding, with the sections having substantially different toughnesses as a result of different heat treatments. Crack extension initiated in relatively brittle sections, and the cracks extended both stably and unstably, depending on the test temperature, toward the tougher sections and then arrested in two of the models. Charpy V impact specimens and both slow-bend and dynamic precracked Charpy V specimens were used extensively for material characterization.

1. INTRODUCTION AND SUMMARY

Dynamic crack propagation and arrest have received increased attention in recent years, and significant advances have been made in understanding the phenomena. Concurrent with these advances, there has been an increased awareness of the potential usefulness of a crack-arrest analytical basis for establishing confidence in the integrity and reliability of large structural components. This awareness has been particularly true for nuclear and aerospace structures where safety and reliability are paramount considerations.

The Heavy-Section Steel Technology (HSST) Program, which is conducted at the Oak Ridge National Laboratory (ORNL) under the sponsorship

of the U.S. Nuclear Regulatory Commission (NRC), has the responsibility for developing and verifying methods for assessing the inherent structural reliability of nuclear pressure vessels. Small models* have been used extensively in the HSST Program as an aid in the development and testing of proposed analytical and experimental methods and procedures. The crack-arrest model tests described in this report represent a continuation of that approach and were performed in anticipation of demonstrating the applicability of the crack-arrest technology to thick-walled vessels under sustained loading. The specific purpose of these model tests was to provide insight and experience, at a relatively low cost, that could be applied to the planning and configuring of a large-scale demonstration test. An additional purpose was to test a particular structural configuration that was being considered for the large-scale test.

Three crack-arrest models, each 38 mm (1.5 in.) in wall thickness, were tested. The three models were of identical configurations, including the size and shape of the starter crack. The only significant variable between tests was the test temperature, which can be characterized as an upper-shelf temperature, a transition temperature, and a lower-shelf temperature. In the order of descending test temperature and the order of testing, the model tests resulted in (1) extensive slow, stable crack extension with slowly increasing vessel internal pressure, (2) slow, stable crack extension interrupted by two short bursts of fast fracture and arrest, and (3) fast fracture and destruction of the model. Chapter 2 gives the background of the rationale used in designing the model configuration. Chapter 3 discusses the basis used for selecting the initial flaw size and target crack length at arrest. The calculations in Chapter 3 were performed using material-property data for a material similar to that which was used for the models. Chapter 4 describes the fabrication of the models, and Chapter 5 gives the material-property data for the steels actually used to construct the crack-arrest models. Chapter 5 also contains the results of a heat treatment study that was carried out in order to explain the unexpected high toughnesses found

---

*A summary of 45 HSST small-scale steel model tests, compiled by J. G. Merkle, is contained in Ref. 1.

in the quenched-only brittle crack-starter material used in the models. The rationale used in selecting a test temperature for the individual model tests is discussed in Chapter 6. The instrumentation and experimental procedures used are discussed in Chapter 7. Chapter 8 describes the test results for the three crack-arrest models. Chapter 9 discusses the experiments, and Chapter 10 summarizes the conclusions drawn from this work.

2. BACKGROUND AND CONFIGURATION

Recent studies[2] relating to rapidly propagating cracks have significantly advanced the understanding of the crack-arrest phenomenon. It is becoming increasingly well accepted that for cases which can be characterized as being linear elastic plane strain, a method for predicting the conditions necessary for the arrest of a rapidly propagating crack does, in principle, exist. The method is based on equating a dynamic stress-intensity factor, which is calculated from geometric and loading parameters and characterizes the state of stress or strain at the crack tip, with a governing material property (toughness) that can be determined from laboratory specimens. For a complex structure containing a propagating crack, the calculation of the relevant stress-intensity factor can be very complicated and likely involve some numerical scheme unless the problem could be simplified by means of suitable assumptions.

The material property governing arrest has been reported for reactor pressure vessel steels[3,4] and for two photoelastic materials.[5,6] The photoelastic material property was determined directly as a function of crack velocity by interpreting fringe patterns or shadows captured on film during propagation by means of high-speed photography. The photographic framing rate combined with crack length measurements taken from individual frames were used to calculate average crack velocities. Figure 1, which is taken from a University of Maryland (UM) report,[6] shows typical material-property data determined by the method described above for Homalite 100, a thermosetting polymeric material. Several specimen types have been used by the UM investigators, and the directly measured values of crack velocity and corresponding instantaneous toughness support the hypothesis that the relationship between toughness and crack tip velocity is independent of specimen geometry.[7] Figure 2, which is taken from a Battelle Columbus Laboratories (BCL) report,[3] shows, for A533, grade B, class 1 steel, the relationship between the material toughness (determined by means of a dynamic finite-difference analysis of a dynamic fracture experiment) and the measured corresponding crack tip velocity. The BCL data indicate that a functional relationship

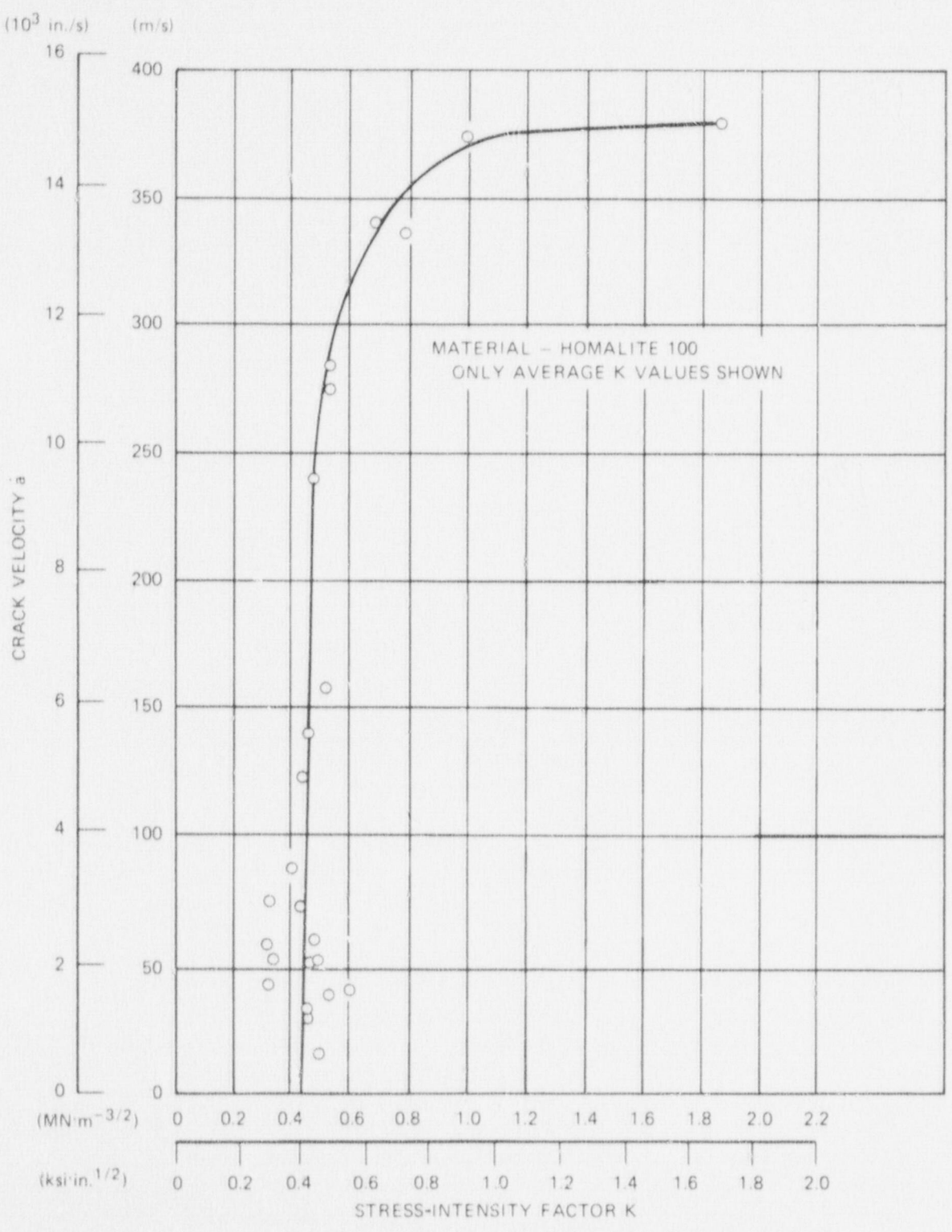

Fig. 1. Crack velocity, ȧ, as a function of instantaneous stress-intensity factor, K, as determined from photoelastic experiments (Ref. 6).

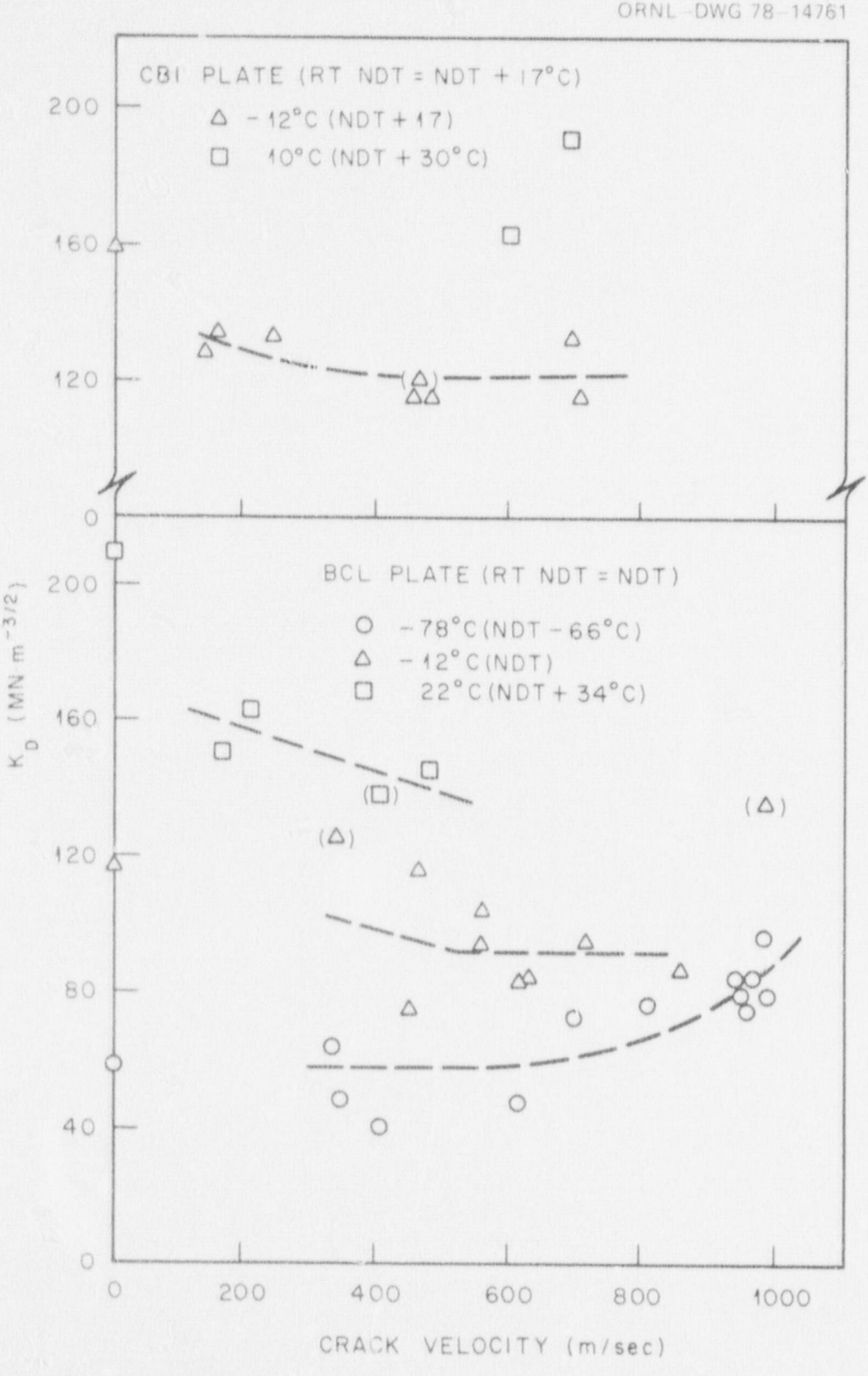

Fig. 2. Dependence of fast fracture resistance, K_D, on crack velocity and temperature for two heats (CBI and BCL) of A533B steel (Ref. 3) (1 m = 3.28 ft; 1 MN·m$^{-3/2}$ = 0.91 ksi·in.$^{1/2}$).

exists between crack tip velocity and the toughness of a steel (i.e., a result comparable to that found for Homalite 100). From the point of view of designing a crack-arrest test configuration, a significant difference between the data for Homalite 100 and for A533, grade B, class 1 steel is that the data for steel at temperatures close to and above the nil-ductility temperature (NDT) indicate a very pronounced minimum value in toughness at crack velocities on the order of 500 m/sec (20,000 in./sec). Although the toughnesses shown in Figs. 1 and 2 are strictly associated with running cracks, they are also presumed to be the values that determine whether a crack will or will not arrest.

The significant facts that are generally accepted concerning crack arrest were reviewed because of their influence on the design of the three crack-arrest pressure vessel models discussed in this report. For example, at the temperatures of interest (i.e., NDT and above), the crack-arrest toughness could be substantially below the crack-initiation fracture toughness K_{Ic}.* This meant that special attention had to be given to including a transition from brittle to tougher material if crack arrest were to be possible for a pressure vessel subjected to a sustained load. The sustained or nearly sustained loading feature was considered necessary for the test because this feature would likely provide the most severe test of crack methodology for an actual reactor pressure vessel.

Two approaches were considered for incorporating toughness transition in the model design: the use of a temperature gradient and the use of a duplex-type specimen made from dissimilar metals. The temperature gradient approach has been used successfully to achieve crack arrest for the thermal shock experiments at ORNL.[8,9] The test material used in those experiments was a steel that had been reaustenitized and water quenched but not tempered. The quenched-only heat treatment provided low toughness similar to that associated with extensive radiation damage and thereby reduced the severity of the thermal shock required to achieve

---

*It should be noted that the values of the stress-intensity factor in Figs. 1 and 2 which correspond to zero crack tip velocity are by definition the nominal static plane-strain fracture toughness, K_{Ic}.

crack initiation to a level that was possible with the thermal shock test loop at ORNL at the time.

In the proposed large-scale crack-arrest test, it would be necessary to compare the test result with the existing reactor pressure vessel (RPV) material data base. At the time the model tests were being planned, it seemed that a thermal shock facility large enough to develop the more severe shock necessary for typical RPV steels was not likely to be built,* and thus it was decided to explore the possibility of the duplex-type pressure vessel configuration.

The idea of placing a small brittle weldment in an otherwise sound pressure vessel was advanced early in the planning, but it was ruled out because of the uncertainty in the crack-initiation conditions that might result from variations in weld metal, residual streses, and crack-initiation toughnesses. The choice was thus narrowed down to a duplex-type configuration in which a brittle cylindrical section would be welded between two tougher sections. Electron-beam (EB) welding is frequently used for the fabrication of duplex specimens because the heat input resulting from the weld is relatively low, thereby minimizing the extent of tempering in the brittle material.

The choice of a brittle cylindrical section for the crack-starting region meant that a fairly large crack jump could be accommodated provided the initiation toughness of the brittle section was sufficiently low relative to the arrest toughness of the tougher material. A large crack jump would presumably enhance the prospects of the crack accelerating up to a velocity corresponding to the minimum running-crack toughness. The choice of a brittle cylindrical starter section also meant that the crack in the cylindrical starter section would likely be a through-the-wall type crack for reasons which will become apparent in Chapter 3. Although this meant that some type of liner would be needed to prevent the loss of the pressurizing fluid, it was considered a net benefit because "break wires" could then be attached to the surface across the expected path of crack propagation, and the crack velocity

---

*Since that time, there have been advances involving cryogenics that may lead to a revised assessment of those prospects.

during the propagation phase could be directly determined through the use of electronic circuitry and high-speed recorders.

Although it was recognized that the duplex configuration posed some difficulties, particularly with respect to scaling to the large-scale experiment, it was decided that at least an initial feasibility effort involving three crack-arrest models was warranted. A factor that made the duplex approach appear particularly attractive was that large thick-walled vessels and cylinders were available for subsequent testing using the large duplex-type configuration. Also, brittle cylindrical sections made from A508 steel that had been water quenched but not tempered were available in sizes that could be used as the insert for an intermediate vessel similar to that shown in Fig. 3. Two of these brittle cylinders (Fig. 4) were ∿610 mm (24 in.).

Since the small models were to be fabricated from 152-mm-thick (6-in.) plate with the longitudinal axes of the model cylinders normal to the plate surfaces, it seemed that the cylindrical sections should be one-fourth-scale models of the intermediate vessels. That is, the 152-mm axial length of the brittle center section of the model was one-fourth the size of the brittle cylinders being considered for the large-scale test. The choice of the one-fourth scale resulted in a wall thickness of 38 mm (1.5 in.) for the crack-arrest models. This wall thickness was considered advantageous, at least relative to that for previous models with much thinner walls, because it would tend to reduce the possible effects of shear lips and would thus better represent plane-strain conditions. A schematic of the model configuration that was finally selected for the three crack-arrest models is shown in Fig. 5. Chapter 3 discusses the basis used for selecting the initial crack length and the crack jump distance. Since the flaw is basically a through-the-wall flaw, a stainless steel liner (shown schematically in Fig. 5) was fillet welded (leaktight) inside the vessel to maintain pressure. Figure 6 shows additional details regarding the initial flaw. The ligament at the base of the machined notch was left in place in order to provide support for the stainless steel liner so that it would not extrude through the notch. A sharp crack was developed along the periphery of the machined notch (as shown in Fig. 6) by making a shallow

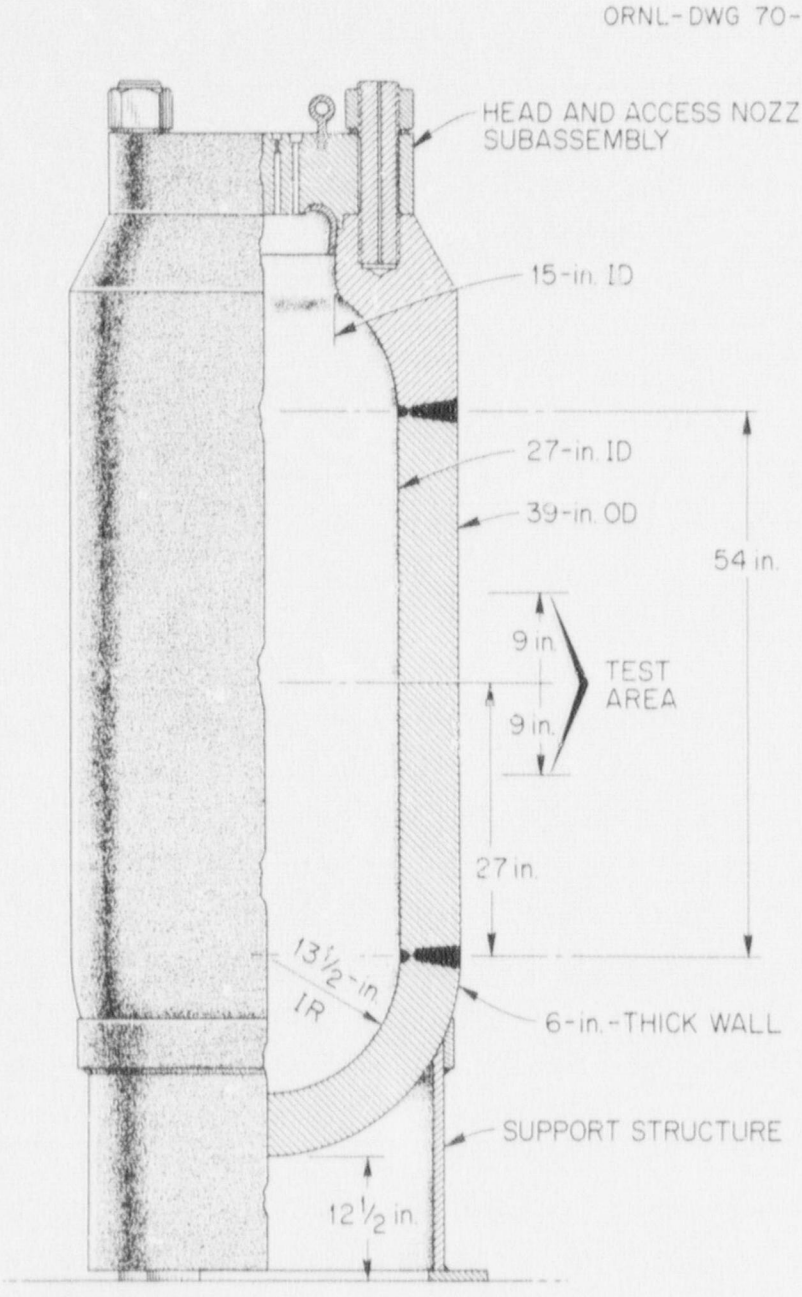

Fig. 3. Typical HSST intermediate test vessel (1 in. = 25.4 mm).

EB weld. Details relating to the fabrication of the models are contained in Chapter 4.

An additional consideration in the choice of the crack-arrest model design was the need for side grooves along the anticipated path of crack propagation. Side grooves are generally used for steel crack-arrest

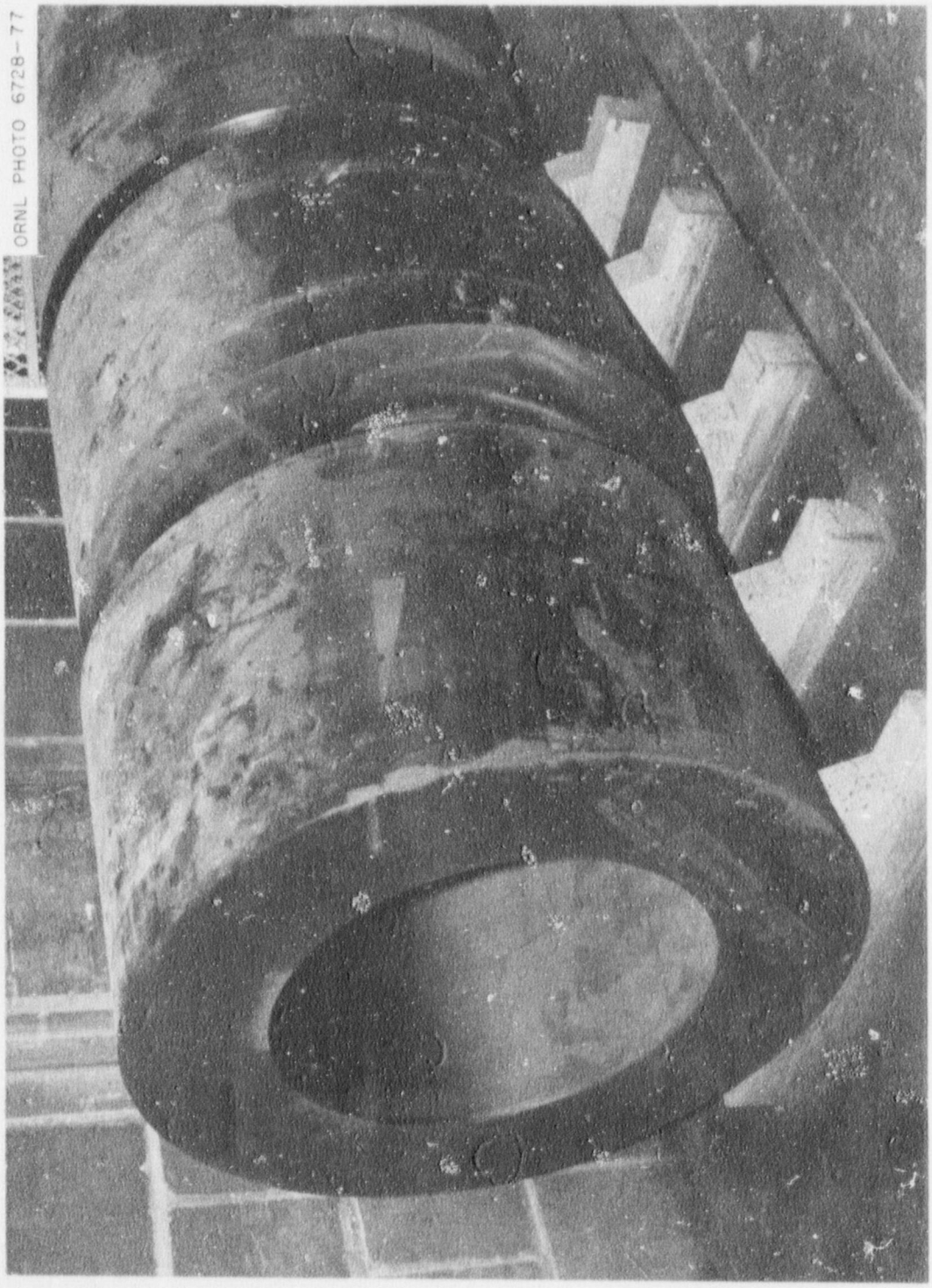

Fig. 4. Quenched-only prolongations that were considered for a large-scale crack-arrest test.

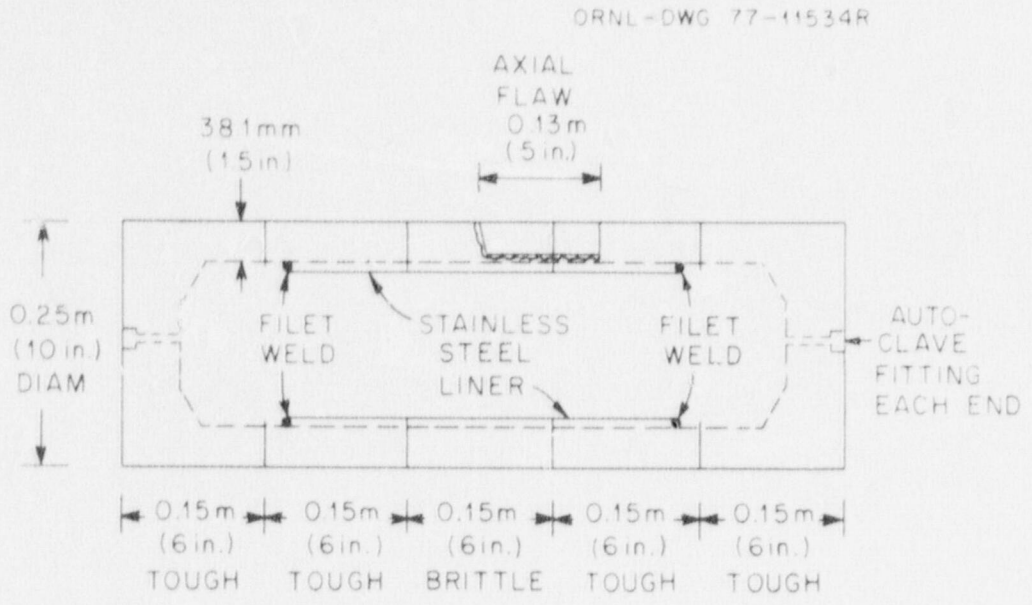

Fig. 5. Schematic of the crack-arrest models.

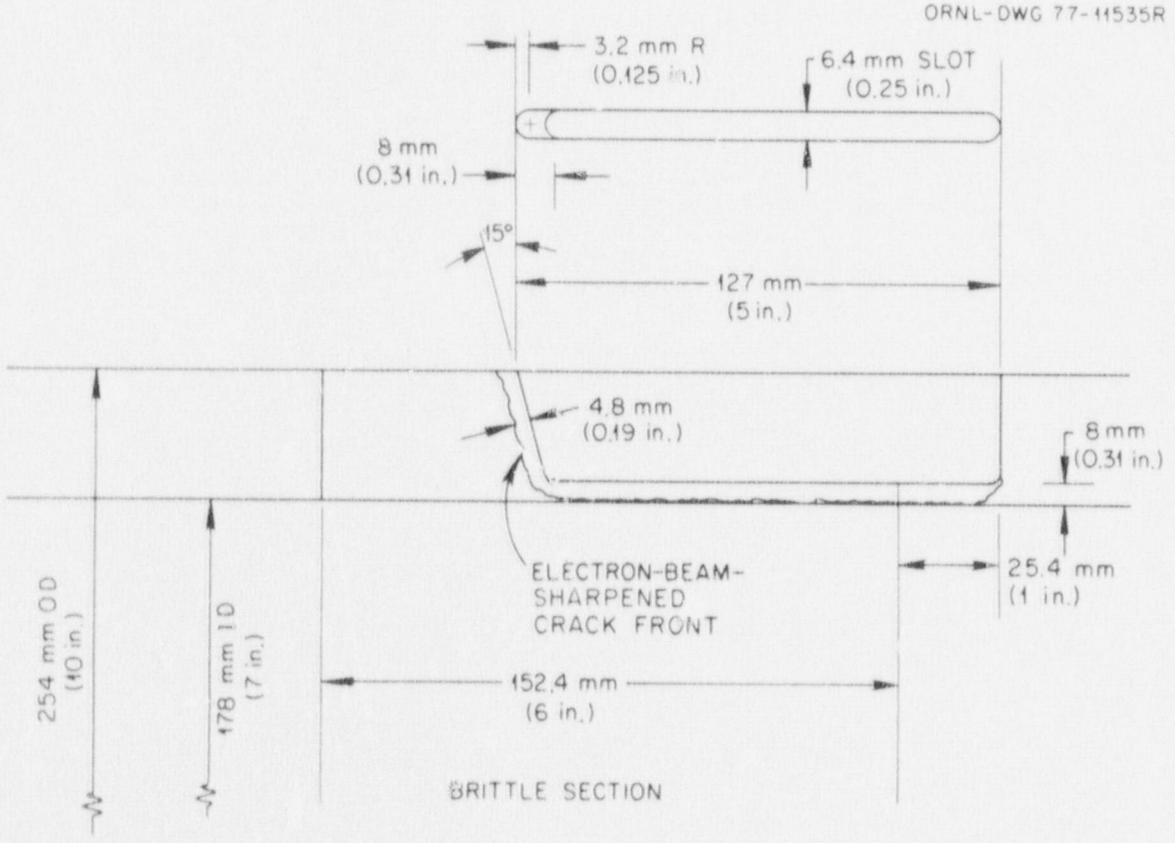

Fig. 6. Schematic of the starter crack that was placed in the three crack-arrest models.

laboratory specimens because they tend to guide the crack tip along the desired path and, more importantly, also tend to reduce the free surface effect on crack propagation by reducing the development of shear lips. The argument is frequently made that, although crack-arrest laboratory specimens are commonly used, they are not wide enough to be considered plane-strain specimens (at least by ASTM standard E-399); a close approximation is nonetheless obtained by means of the side grooves. Although this argument would seem to have merit, some question concerning the claim does remain; thus the first three models were configured without side grooves in an attempt to determine whether they could be eliminated for the large-scale experiment.

3. BASIS FOR SELECTION OF FLAW SIZE

Appendix A of this report discusses a simplified method that was developed to analyze rapidly propagating axial cracks in cylinders having a circumference several times the length of the crack jump.* Sample calculations using the simplified method indicated that, during propagation, the crack for a typical crack-arrest model geometry would have a stress-intensity factor less than the statically calculated value for a crack of equal length. Appendix B contains the results of a dynamic finite-element analysis of a propagating axial crack in a typical model. The results in Appendix B tend to support the conclusion from the sample problems in Appendix A (i.e., that the static analysis gives conservative results) and also indicate that, once the crack arrests, there is an excursion of the stress-intensity factor above the statically calculated value on the order of 25% for the model configuration and a particular arrested crack length of 152.4 mm (6.0 in.). This overshoot would be important for determining whether the crack would reinitiate after arrest. From the results discussed above, it was decided that statically calculated stress-intensity factors would be sufficient for the design of the experiments.

For an axial, through-the-wall flaw in a thin shell, Folias[10] has shown that the stress-intensity factor K_I can be expressed as

$$K_I = \sigma \sqrt{\pi a}\, M \,, \tag{1}$$

where the hoop stress σ is given by $\sigma = PR/t$ and the bulging factor M by

$$M = \left(1 + 1.61 \frac{a^2}{Rt}\right)^{1/2} . \tag{2}$$

The symbols P, R, t, and a are vessel internal pressure, vessel mean radius, vessel wall thickness, and crack half-length, respectively. The

---

*For the simplified analysis, it was assumed that radial inertia could be ignored.

bulging factor M was derived for radius-to-thickness ratios of 100 but has been used with some success on much thicker-walled cylinders.[11] For convenience, the symbol $K_I(a_i)$ will be used to identify K_I when the initial crack length (a_i) is substituted in Eqs. (1) and (2), and $K_I(a_f)$ will be used to identify K_I when the arrested crack length (a_f) is substituted. For the purpose of designir the experiment, a useful expression is the ratio of $K_I(a_f)$ to $K_I(a_i)$, which is given by

$$\frac{K_I(a_f)}{K_I(a_i)} = \frac{\sqrt{a_f}\left(1 + 1.61\,\frac{a_f^2}{Rt}\right)^{1/2}}{\sqrt{a_i}\left(1 + 1.61\,\frac{a_i^2}{Rt}\right)^{1/2}} \tag{3}$$

when the internal pressure of the model is assumed to be constant. Equation (3) is shown plotted for three assumed final arrested crack lengths as a function of the initial crack length in Fig. 7. For arrest to occur, the A533, grade B, class 1 crack-arrest toughness, which is currently denoted by K_{Im}, must exceed the static fracture toughness K_{Ic} of the quenched-only material. Thus, the criterion for crack arrest is given by*

$$\frac{K_{Im}}{K_{Ic}} > \frac{K_I(a_f)}{K_I(a_i)}\,, \tag{4}$$

and for nonarrest by

$$\frac{K_{Im}}{K_{Ic}} < \frac{K_I(a_f)}{K_I(a_i)}\,. \tag{5}$$

---

*Since $K_{Ic} = K_I(a_i)$ at initiation, the arrest criterion can be expressed in the normalized form of Eq. (4). Similarly, nonarrest can be expressed in the normalized form of Eq. (5).

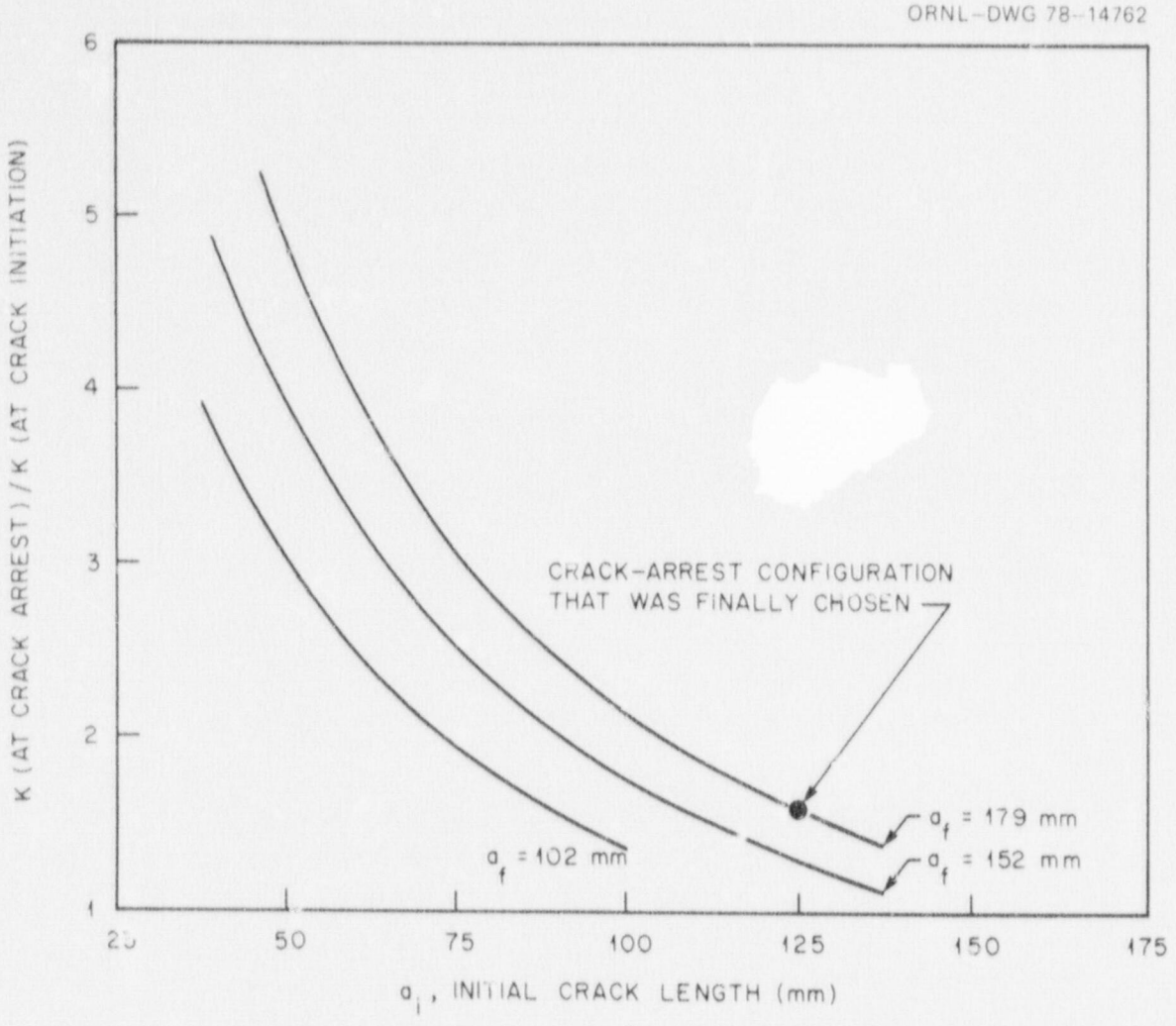

Fig. 7. Results of a parametric study relating initial crack length, a_i, to the final (arrested) crack length, a_f (1 mm = 0.039 in.).

The above equations do not take into account dynamic effects or the variation of hoop stress through the thickness of the vessel wall. Nevertheless, Eqs. (4) and (5) were considered adequate for the purpose of choosing the initial and final flaw sizes for the model tests.

The method for selecting the crack size then depends on knowing K_{Ic} of the brittle material and K_{Im} for the quenched-and-tempered material where the crack is to arrest. The best K_{Ic} data available at the time the model tests were being planned was the K_{Ic} curve for the quenched-only A508 and A533 material that was developed for the ORNL thermal

shock experiments. This curve is shown in Fig. 8, which is taken from Ref. 8. There are two well-known estimates of K_{Im} for quenched-and-tempered A533. The BCL estimate, $K_{ID(min)}$, was taken from Ref. 3 and is shown plotted in Fig. 9 as a function of temperature. The data originally presented by BCL was plotted against temperature minus the nil-ductility temperature (i.e., T - NDT). For the work here, the NDT of the quenched-and-tempered material is known to be -23°C (-10°F) (see Chapter 5), and, as a convenience, the BCL data have been replotted with the temperature T as the independent variable. The other estimate of K_{Im} is the Materials Research Laboratory (MRL) value, known as K_{Ia} (Ref. 4), which is plotted vs temperature in Fig. 10.

The data shown in Figs. 8 to 10 were used to calculate values of $K_{Id(min)}/K_{Ic}$ and K_{Ia}/K_{Ic} as a function of temperature, where the K_{Ia} values were taken to be the average of the scatter bands shown in Fig. 10. These ratios are shown plotted in Fig. 11. As is evident from the curves in Fig. 11, the ratios are not strongly dependent on temperature. It should be noted that the thermal shock K_{Ic} values are for material that was quenched in 203-mm-thick (8-in.) thicknesses. It was planned that the center cylindrical sections of the models, which were to be brittle, would be quenched after they were machined to shape. Quenching after machining would reduce costs significantly (inasmuch as the quenched-only material is extremely hard and thus difficult to machine) and presumably would result in a more rapid and uniform quench. The more rapid quench was expected to result in static fracture toughness values that would be more highly degraded than the values shown in Fig. 8. If, in fact, the initiation toughness of the brittle starter material were lower, the curve in Fig. 11 would be effectively raised and thereby allow a better chance for a propagating crack to be arrested. The actual curve is discussed in Chapter 6, which follows the chapter describing the material properties of the steels used in constructing the models.

Since the goal of the crack-arrest model tests was to demonstrate both crack arrest and nonarrest with a specific configuration using a minimum number of tests, it was decided to use a nominal K_{Im}/K_{Ic} value

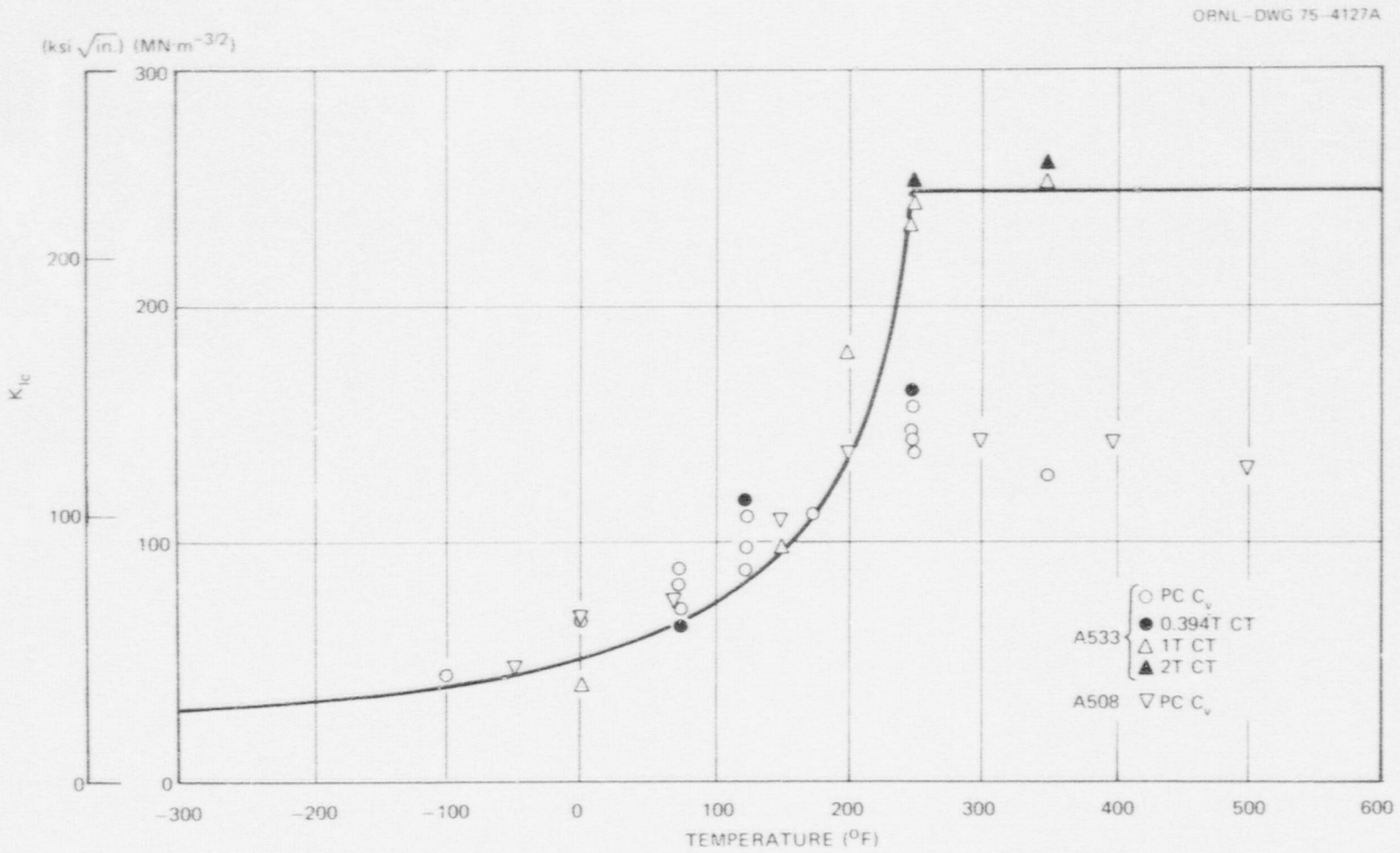

Fig. 8. Static fracture toughness data for A533B and A508 in the as-quenched condition which were developed for the thermal shock program and used for the initial planning of the crack-arrest model tests.

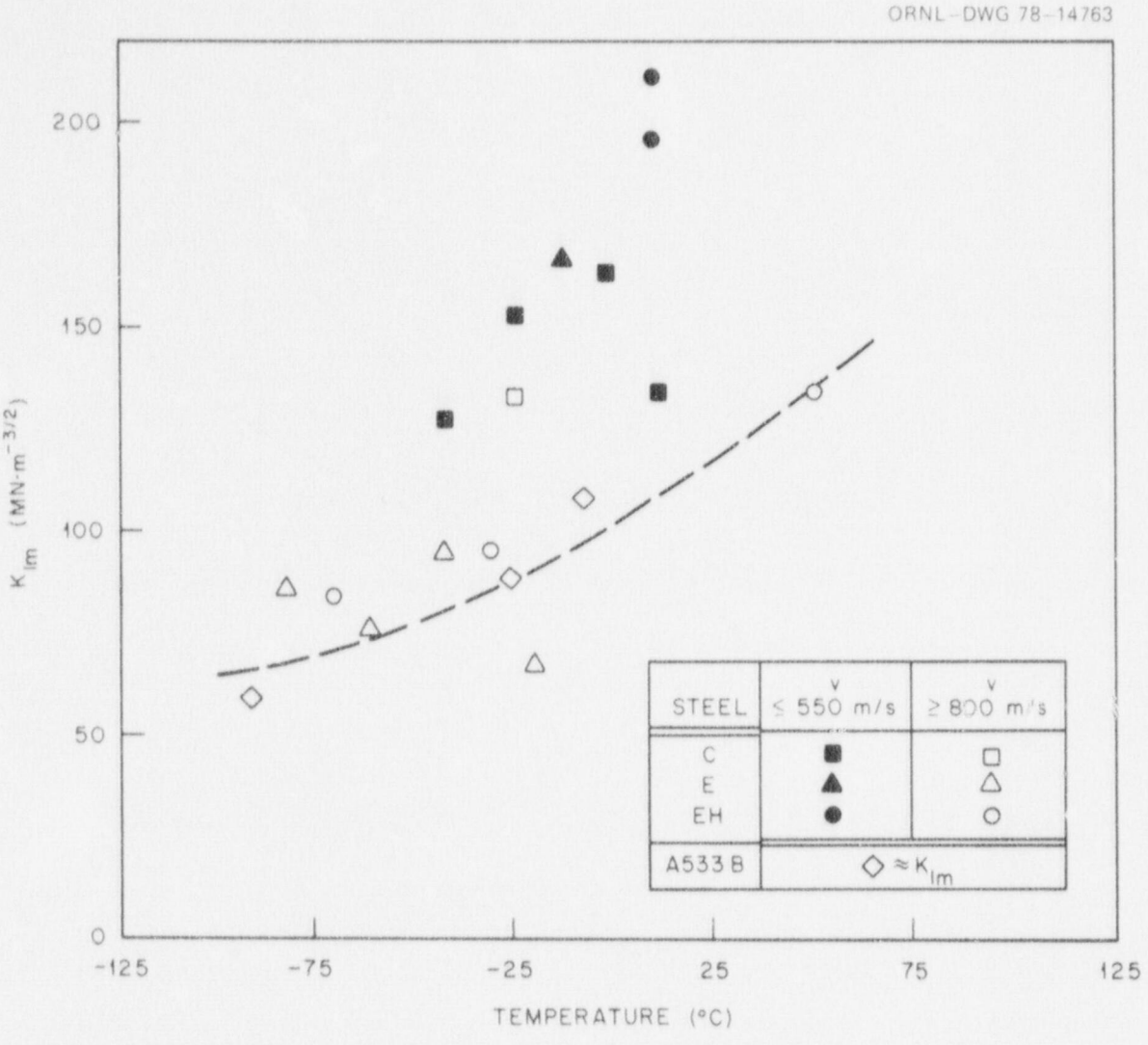

Fig. 9. Temperature dependence of K_{Im} for ABS ship steels and for A533B pressure vessel steel (Ref. 3) (1 MN·m$^{-3/2}$ = 0.91 ksi·in.$^{1/2}$; 1 m = 39.37 in.).

of 1.6 (obtained from the curves in Fig. 11) to establish the flaw size for the first model test.

The plot of the ratio of K_I (at arrest) to K_I (at initiation) as a function of crack length in Fig. 7 shows that a long initial flaw would be necessary and that a modest crack jump on the order of the wall thickness or slightly more could be tolerated and still have a reasonably good chance of arresting. The final choice of crack size is shown in Fig. 6. The crack length at arrest was just beyond the fusion zone of

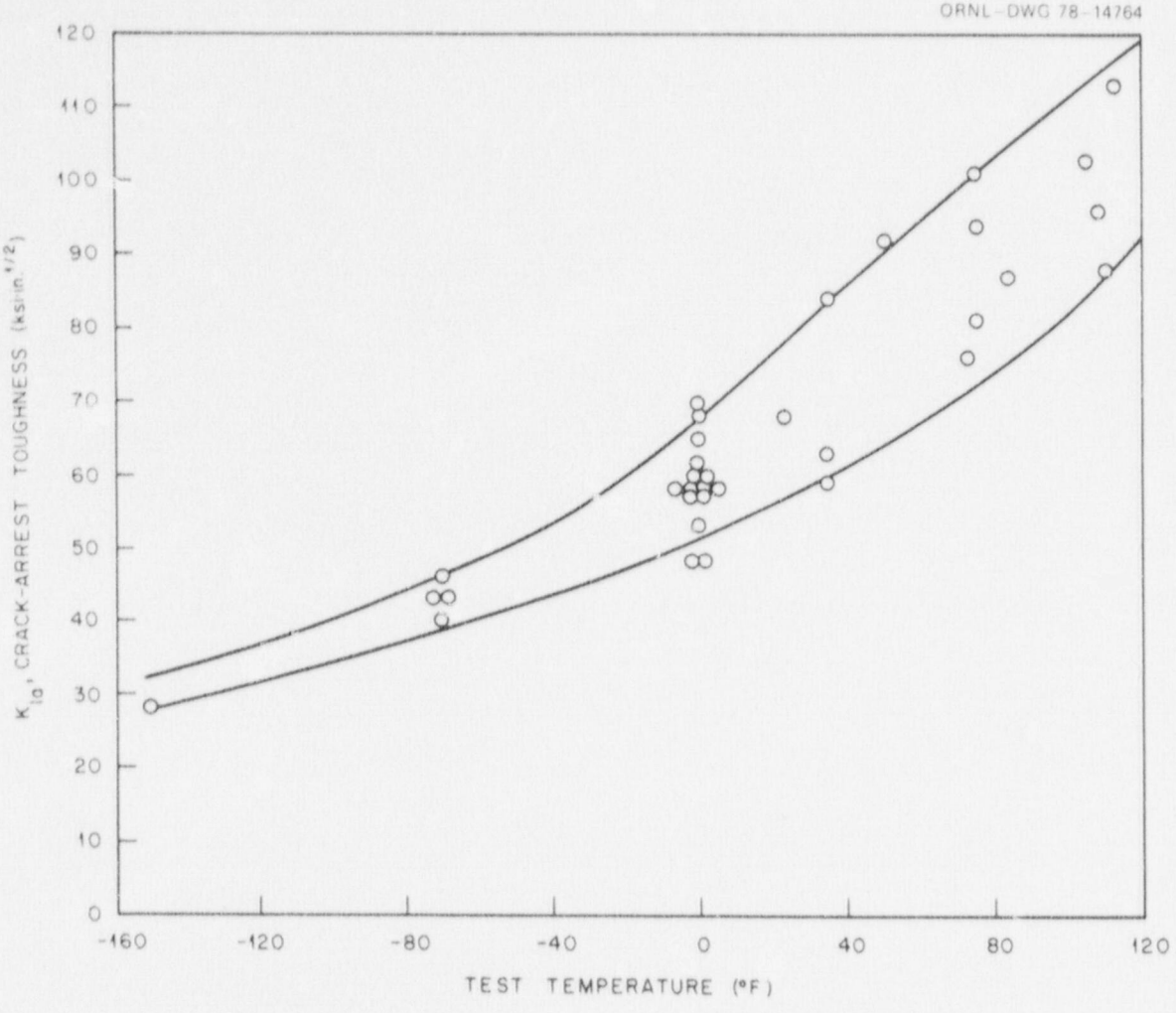

Fig. 10. Crack-arrest toughness (K_{Ia}) as a function of temperature (Ref. 4) [°C = 5/9 (°F - 32); 1 ksi·in.$^{1/2}$ = 1.0988 MN·m$^{-3/2}$].

the EB weld joining the tough material to the brittle starter section [i.e., 179 mm (7 in.)]. Since the brittle section was only 152 mm (6 in.) long, it was necessary that the end of the crack (notch) that did not propagate be located in tough material (see Fig. 5).

If crack arrest had resulted during the first test, it was planned to shorten the initial crack length; this would have increased the pressure at initiation and thereby increased the probability of nonarrest. If the second test also resulted in the arrest of the propagating crack, it would have been possible to reduce the initial crack length even further for the third test. The optimum outcome for the test series was

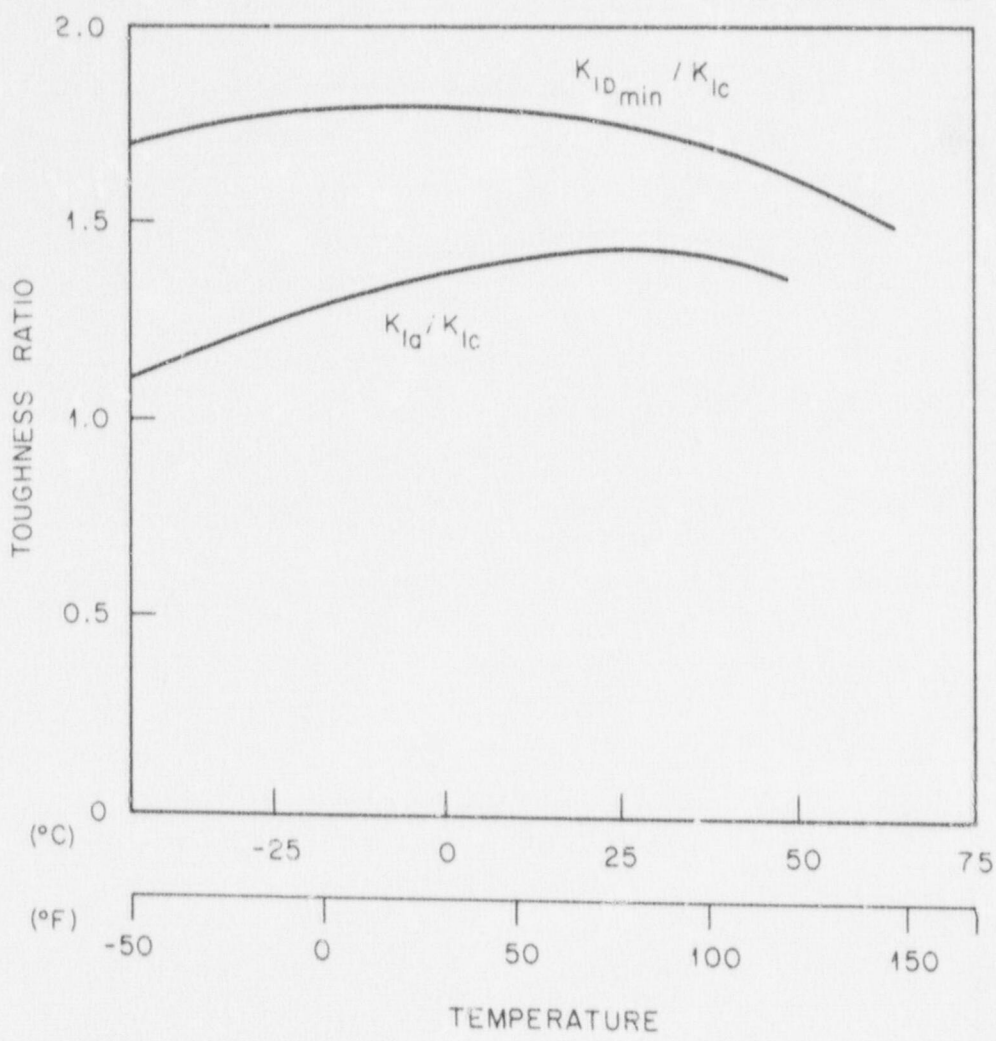

Fig. 11. Toughness (K) ratios based on the material properties $K_{ID(min)}$ and K_{Ia} for the quenched and tempered material, and K_{Ic} for the quenched-only material (thermal shock material).

considered to be arrest and nonarrest at not greatly different test pressures. Bracketing the pressure at which arrest could occur permits a more critical assessment to be made of the crack-arrest technology and the suitability of the proposed configuration for large-scale experiment(s).

It will be recalled that the crack-arrest technology that was to be tested was limited to linear elastic conditions. Thus, it was necessary to determine if the pressure at crack initiation was less than the pressure at which yielding developed. Since the crack-arrest models are

one-fourth-scale models of intermediate test vessels, the structural behavior would be similar to that of the larger vessels, at least in the cylindrical core section. The intermediate test vessels have been extensively studied.[12-14] For the cylindrical region of the model away from the ends, the state of stress under internal pressure in the elastic range is almost the same as that for an infinitely long, thick-walled hollow cylinder with closed ends. The equation for the circumferential stress is then

$$\sigma = P \frac{(r_o/r)^2 + 1}{(r_o/r_i)^2 - 1} , \qquad (6)$$

where r_i, r_o, and r are the inside, outside, and general radii, respectively, and P is the vessel internal pressure. The stress given by Eq. (6) is plotted as a function of the general radius in Fig. 12. A

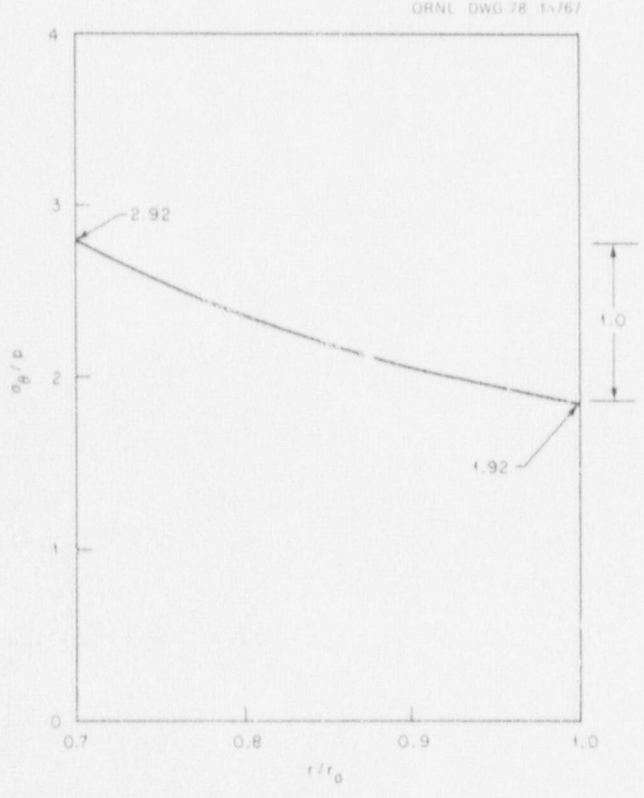

Fig. 12. Circumferential stress distribution in the cylindrical region of the crack-arrest models.

reasonable lower yield strength of the quenched-and-tempered A533 material is 435 MPa (63 ksi). Thus, yielding on the vessel inside surface would be expected at a pressure of 149 MPa (21.6 ksi). The maximum pressure that could be expected can be found by taking a nominal value of K_{Ic} from Fig. 8 and calculating the vessel internal pressure using Eq. (1). For a K_{Ic} of 220 MPa (200 ksi), the maximum pressure that would likely be achieved without crack propagation occurring would be 131 MPa (19 ksi), which is below the onset of yielding. Consideration would also have to be given to the size of the plastic zone that would develop about the crack tip as a result of pressurizing the flawed vessel. That aspect is covered in Chapter 8. Chapter 6 covers the test temperature selection, which was made when actual material properties were available.

The pressure allowed by ASME Boiler and Pressure Vessel Code is calculated here only for reference purposes, since the models are experimental hardware intended for pressurization to failure. The Code-allowable pressure for a cylindrical vessel is determined by the general primary membrane stress intensity, which is given by[15]

$$S = \frac{Pr_i}{r_o - r_i} + \frac{P}{2} . \tag{7}$$

Setting $S = S_m$, the allowable stress intensity from Ref. 15 gives

$$P_{allowable} = \frac{S_m}{r_i/(r_o - r_i) + (1/2)} . \tag{8}$$

For the models, considering only the stress intensity for A533, grade B, class 1. S_m equals 184 MPa (26.7 ksi), which gives a $P_{allowable}$ of 65 MPa (9.4 ksi). The yield strength of the quenched-only material is considerably higher (see Chapter 5) than that for A533, grade B, class 1; thus, the quenched-only material properties were not needed to establish this benchmark Code-allowable pressure for the models.

4. MODEL FABRICATION

The modular assembly approach was selected for the fabrication of the crack-arrest models for the following economic and technical reasons: (1) the capability to readily saw out component sections from the tested models for reuse and (2) the ability to pre-prepare well-defined, brittle crack-starter sections (i.e., the centermost cylinder of each test assembly) and use them interchangeably in test assemblies.

The need to preserve the brittle material characteristics in the crack-starter module called for the selection of a welding process requiring minimum heat input. Electron-beam (EB) welding is a joining process in which the workpiece is bombarded with a dense stream of high-velocity electrons. Welding is normally done in an evacuated chamber with both the beam-generating devices and the workpiece in a vacuum environment to prevent contamination during welding. Figure 13 illustrates the EB welding process. The outstanding feature of this process is its ability to make very narrow, deep, full-penetration, single-pass welds, thereby minimizing heat input to the materials being welded. The electron beam is capable of producing intense, concentrated local heating that can almost instantly vaporize a hole through the entire joint

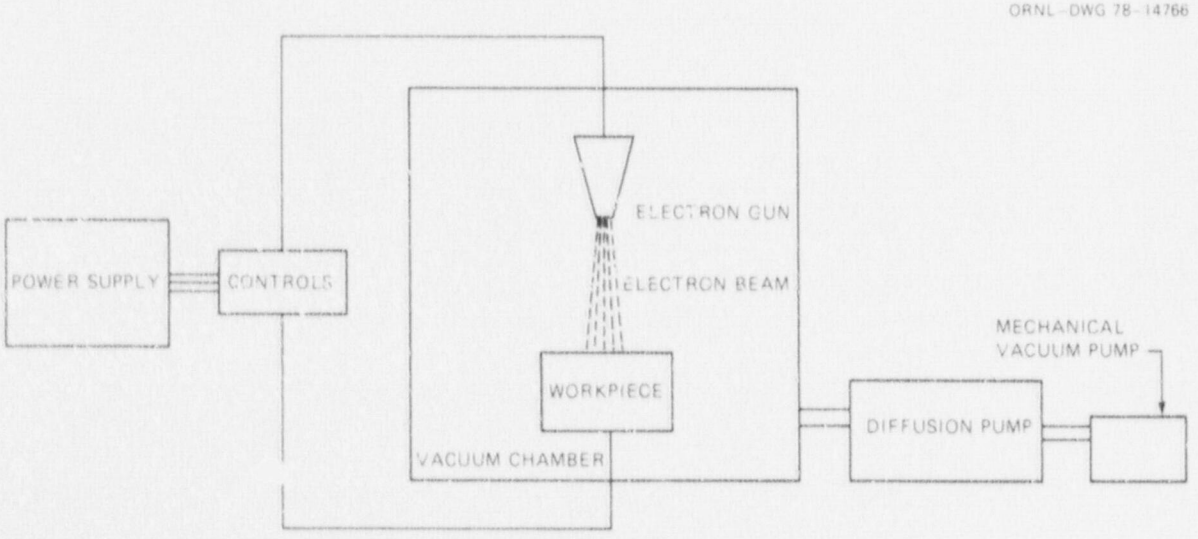

Fig. 13. Schematic of the electron-beam welding facility.

thickness. The walls of such a hole are molten and, as the beam is moved along the joint, more metal on the advancing side of the hole is melted. The melted material flows around the bore of the beam and solidifies along the rear, thus making the weld. Heat input in EB welding is controlled by four basic variables: (1) the number of electrons per second (beam current) impinging on the workpiece; (2) the electron speed at the moment of impact (accelerating potential); (3) the diameter of the beam at, or within, the workpiece (beam focus or beam spot size); and (4) the traverse speed.

Electron-beam welding development efforts at the "large Sciaky facility" at the Y-12 Plant of Union Carbide Corp.-Nuclear Division established highly successful, repetitive, single-pass, full-penetration weldments of x-ray grade quality for joints between low- and high-toughness sections and between two high-toughness sections. The incorporation of a copper chill ring about the inner cylinder joints greatly reduced the problem of welding heat spreading to adjacent cylinder sections. Tempstik indicators at both inside and outside diameter surface locations adjacent to the weld joint registered temperatures of 290°C (550°F) at locations 19 mm (3/4 in.) removed from the joint center for 38-mm (1 1/2-in.) wall-thickness steel sections. EB welding was used for fusion-joining all crack-arrest model components. Sound joints were made without postweld heat treatment, which, of course, could not have been achieved if the starter section were to remain brittle.

The high-toughness cylindrical sections and the caps were machined from HSST plate W57, and the center cylinders were machined from HSST plate 03 (models 1 and 2) or plate 04 (model 3). The axes of the cylinders were normal to the surfaces of the 152-mm-thick (6-in.) plates. The cylinders were stenciled so that the roll direction of the original plate could be referenced for subsequent crack orientation. Flaws were RT-oriented* for the test assemblies. The plate 03 and 04 cylinders were reaustenitized for 1.5 hr at 871°C (1600°F) and water quenched.

---

*The R and T orientations are defined in Chapter 5.

The caps and one of the two intermediate cylinder units of assembly 1 were reused for model 3. Sawcuts were taken through butt-weld centers of the tested model, followed by ∿8-mm-deep (∿5/16-in.) end cleanup lathe cuts and minimal inside and outside diameter cosmetic machining to restore the cylinders. The restored components are shown in Fig. 14.

Model fabrication involved a five-step procedure in the following order:

1. subassembly of the three center cylinder sections,
2. slotting and flawing,
3. liner installation to center subassembly,
4. attaching end caps,
5. flaw sharpening.

The center subassembly and component parts are shown in Fig. 15 along with the support jig used for EB flaw welding. Copper chill rings were used to align component cylinders for subassembly. These rings were made from 6.4 × 51 mm (1/4 × 2 in.) bar stock and rolled to snap into cylinder interiors. These rings also supported the center three cylinders for assembly mounting into the lathe. The lathe shown in Fig. 16 rotated the subassembly under the stationary EB gun, which was mounted so as to emit electrons vertically down onto the horizontal cylinder joints.

A highly defocused beam (focusing current set 25 mA above that required to obtain sharp focus on the outside surface of the cylinder) was used to ensure full penetration with a single pass without preheating. This defocus setting provided sharp focus approximately one-third of the way through the cylinder wall. The copper rings prevented interior "suckback" and served to blend the interior contours with minimal "push-through." Defocus parameters were developed to give a uniform, slightly tapered bead of minimum width with minimum top surface crowning. Every effort was made to limit heat during welding in order to minimize tempering of the low-toughness material. The full-penetration, single-pass butt welds were made at 50 kV, 202 mA, and a welding speed of 15.2 cm/min (6 in./min). The applied energy per joint traverse was 40,000 J/cm (101,000 J/in.).

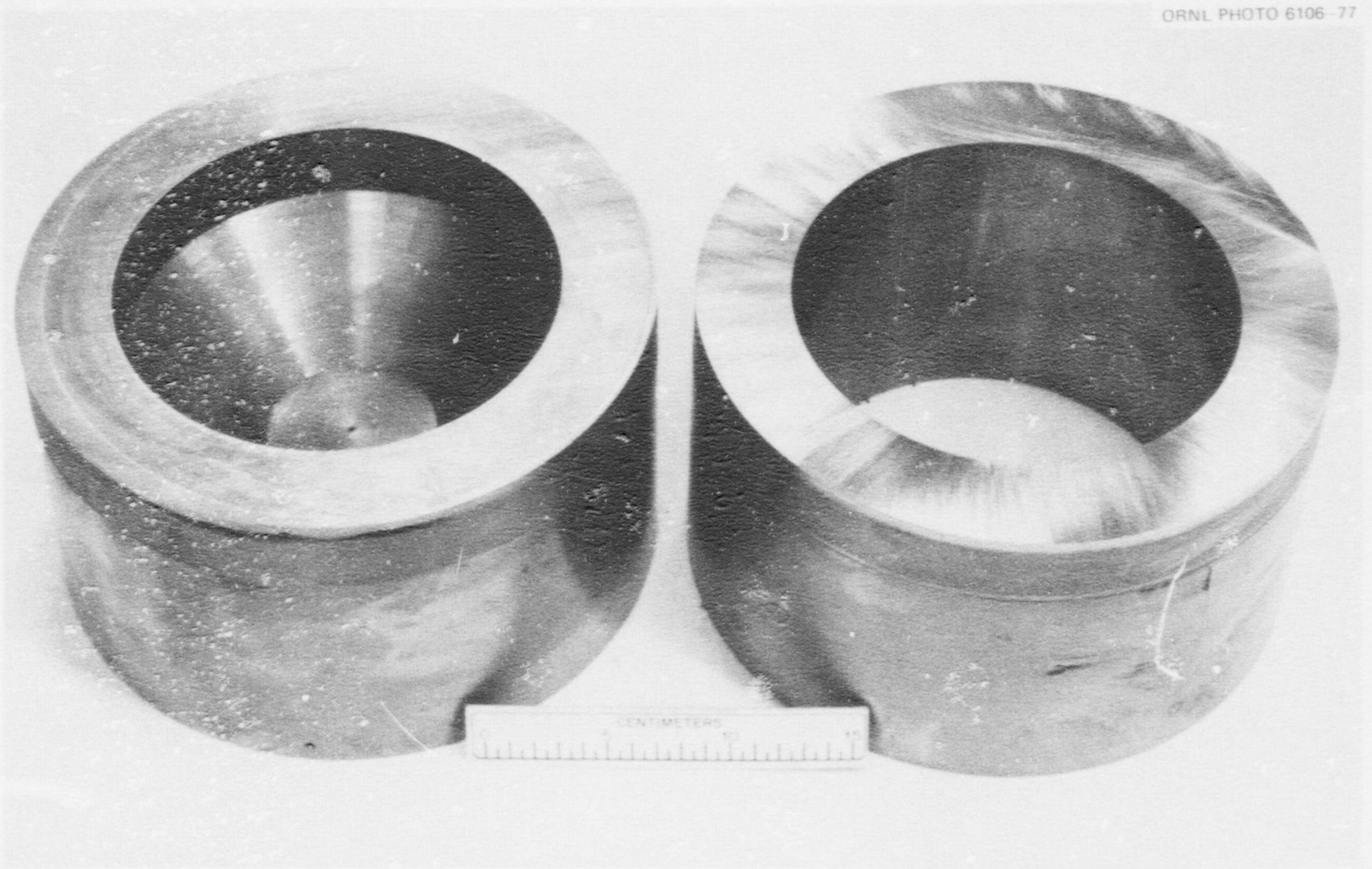

Fig. 14. Crack-arrest model components — restored cap and intermediate cylinder ready for reuse (1 cm = 0.394 in.).

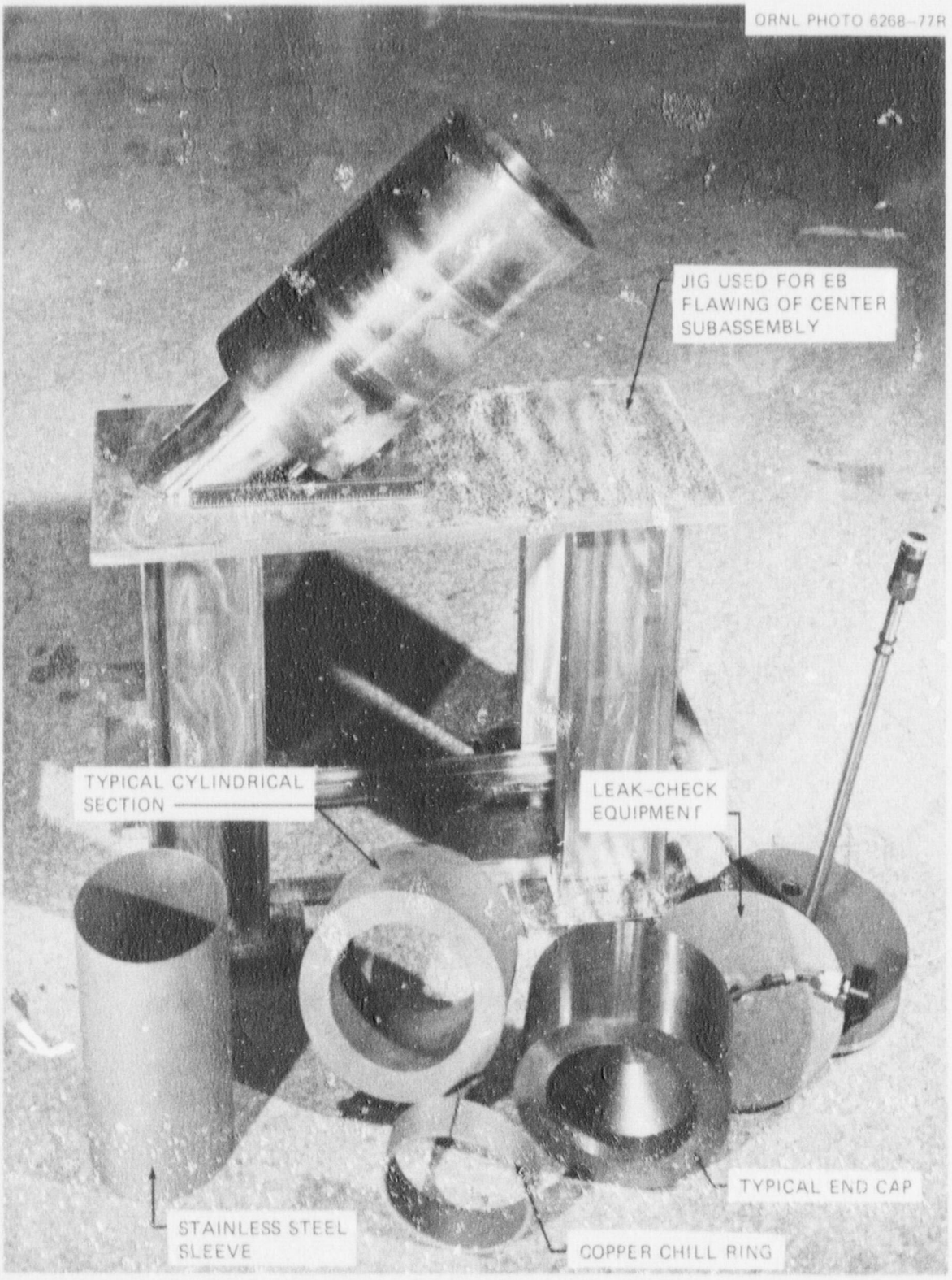

Fig. 15. Center section subassembly and component parts of crack-arrest test model (1 cm = 0.394 in.).

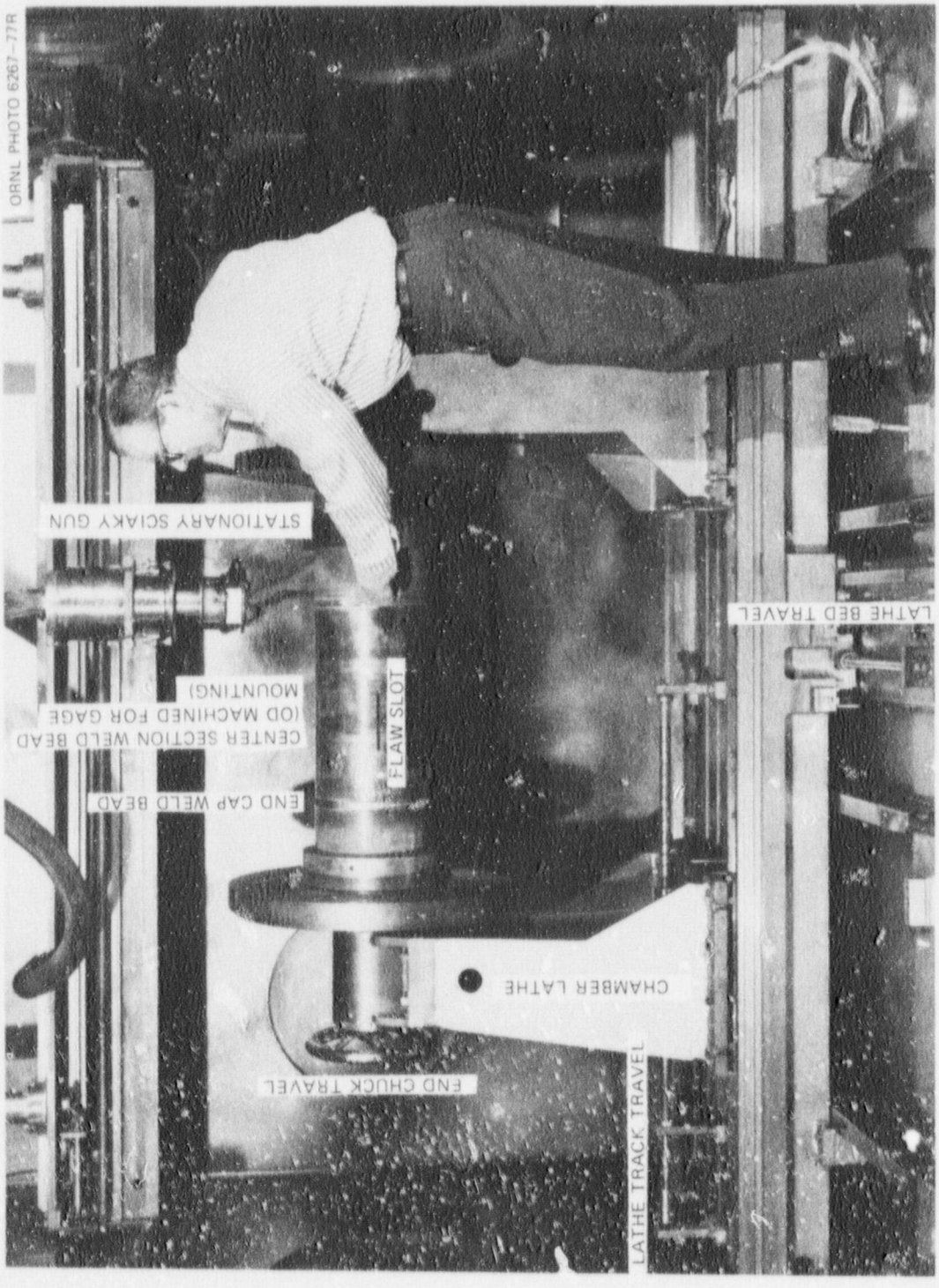

Fig. 16. Crack-arrest test model mounted in lathe within the electron-beam vacuum chamber.

The three-cylinder subassembly was then transferred back to the machine shop for removal of the copper chill rings and for machining on the outside surface in the weld-joint region to provide the smooth exterior surfaces required for mounting the strain gages. Next, it was transferred to a shop milling cutter for milling a 6.4-mm (1/4-in.) slot to a depth of 30.2 mm (1 3/16 in.), as shown schematically in Fig. 6. The slotted subassembly was returned to the weld chamber for a two-step EB weld flawing operation — first on the 15° slope with the subassembly placed on the table jig (Fig. 15) and then on a lathe with the slot placed horizontally and aligned below the gun. Power and speed selections were programmed for a weld of pear-shaped contour and 8-mm (5/16-in.) depth so that, upon hydrogen-charging, the bead would crack and form a through-the-ligament flaw at the bottom of the slot as well as a flaw of equal depth along one slope. EB operations were programmed to 40 kV and 175 mA and to a traverse gun speed of 2280 mm/min (90 in./min) which deposited 1850 J/cm (4700 J/in.) of energy.

A prefabricated 1.6-mm-thick (1/16-in.) 304L stainless steel cylinder was cut about 76 mm (3 in.) shorter than the three-cylinder subassembly length and slipped into the subassembly with a diametral clearance of about 0.76 mm (0.030 in.). The carbon steel cylinders were then preheated to 177°C (350°F), and the stainless steel liner was heliarc tacked, followed by gas-tungsten arc seam welding. A visual weld inspection and a mass spectrometer helium leak check were performed to ensure seal integrity.

End caps were fitted to the lined subassembly with copper chill rings, and the complete test specimen was reinserted into the lathe for transfer into the weld chamber for EB welding, as already described. The cap weldments were used without subsequent postweld machining, since all gage mountings were located well within the central portion of each model assembly. This completed the assembly of the models, and the only operation that remained was sharpening the flaws.

A rapidly placed autogenous EB weld in quenched-only material normally cracks about and along its centerline upon cooldown. It is often difficult, however, to confirm the cracking from a visual inspection. In order to ensure cracking, a hydrogen-charging operation similar to that shown schematically in Fig. 17 can be employed. A

M&C PHOTO Y101804

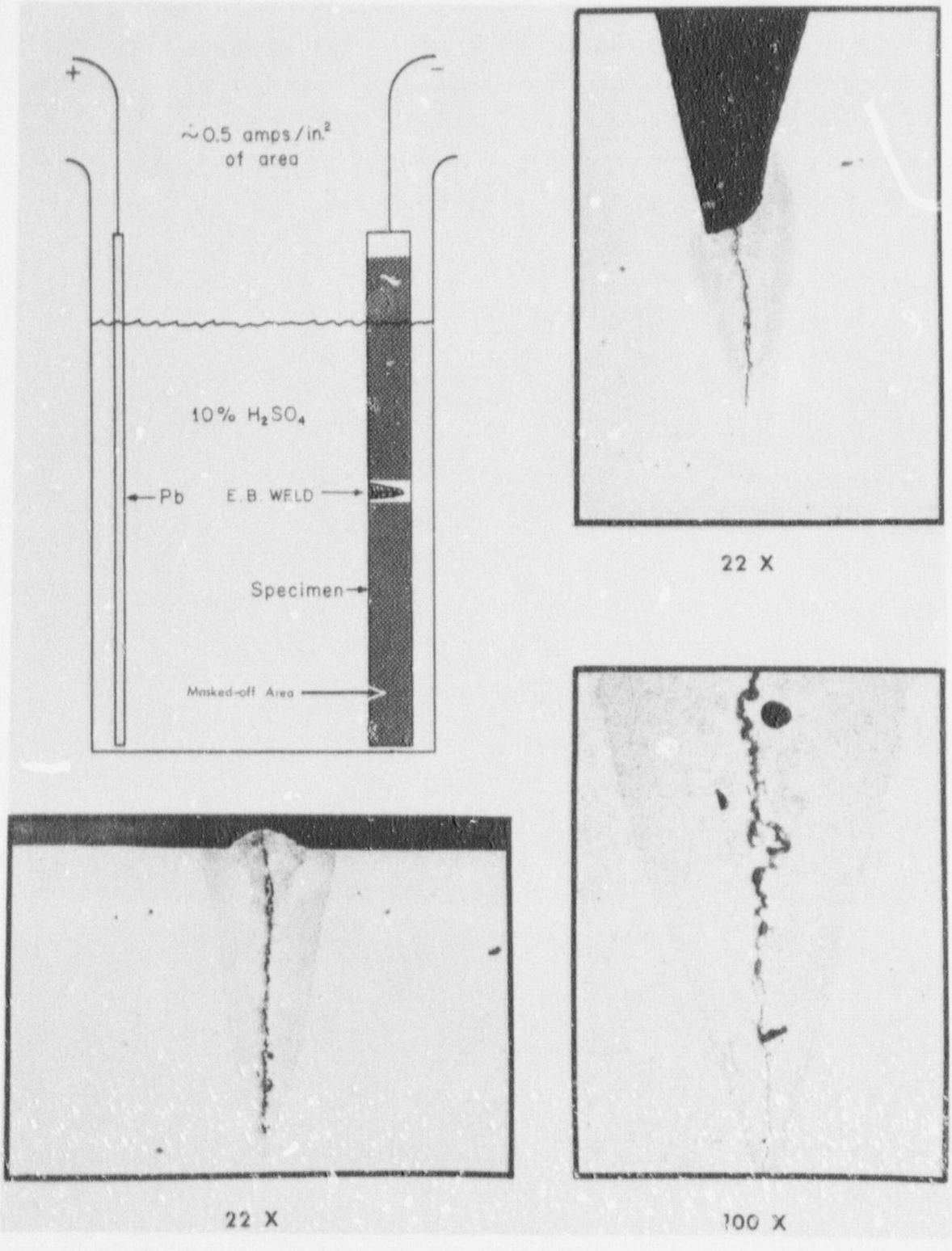

Fig. 17. Illustration of the process used in the production of hydrogen-induced cracks in low-alloy, high-strength steels. The photomicrographs were taken from specimens cracked by this technique (1 in.^{2} = 645 mm^2). (Original reduced 21%)

visual inspection confirmed the existence of a crack in the first model after the EB flawing weld. Hydrogen charging for ∿20 min was required for the second and third models before a crack could be positively identified. Cracks formed by hydrogen-charged EB welds are presumed to be similar to those produced by mechanical means.

5. MATERIALS CHARACTERIZATION

5.1 Source of Materials

The materials used in the crack-arrest models came from three sources: the low-toughness material came from the 305-mm-thick (12-in.) HSST plates 03 and 04; the high-toughness material was obtained from the 152-mm-thick (6-in.) A533 plate material which had been used for HSST submerged-arc weldment W57. All source materials were ASTM A533, grade B, class 1 steel and have been well documented.[16,17] The models were to be fabricated from 152-mm-long (6-in.) cylindrical courses obtained by machining the individual cylinders from 152-mm-thick plate with the longitudinal axes of the cylinders oriented perpendicular to the plate surface. In order to expedite the machining of the cylinders, plates 03 and 04 were split into 152-mm-thick plates and renumbered 03JZ and 04BE. The piece of base plate W57 was designated as 57V.

The applicability of the materials for their intended use in the crack-arrest models was determined by characterizing their toughness properties after heat treatment. The sectioning and specimen preparation of the three source materials are described in Appendix C.

The high-toughness material (57V), which had been quenched and tempered and subjected to postweld heat treatments during the weldment preparation, was used in the as-received (AR) condition (without additional heat treatment). Sectioning and specimen preparation of 57V is shown in Fig. C.1 (Appendix C). The materials to be used for low-toughness components (i.e., from plates 03JZ and 04BE) were cut into 38- to 44-mm-thick (1.5- to 1.75-in.) sections or plates, as shown in Figs. C.2 and C.3. These thicknesses are similar to the wall thickness of the models. The plates were reaustenitized for 1 1/2 hr at 871°C (1600°F) and quenched in chilled, agitated water to provide the low-toughness material, also referred to as as-quenched (AQ) material. This material was cut into specimens, as shown in Figs. C.2 and C.3.

5.2 Orientation

The sections from which the specimens were obtained in all three materials were sawed with their 38- to 44-mm thickness in the rolling direction (R) or transverse to the rolling direction (W) of the original plate, as shown in Figs. C.1 through C.3. The notations used to indicate specimen orientation for all three plates relate to these original plate dimensions, as shown in Fig. 18; however, when the 38- to 44-mm-thick sections from 03JZ and 04BE were reaustenitized and quenched, they developed their own through-the-thickness property distribution. After

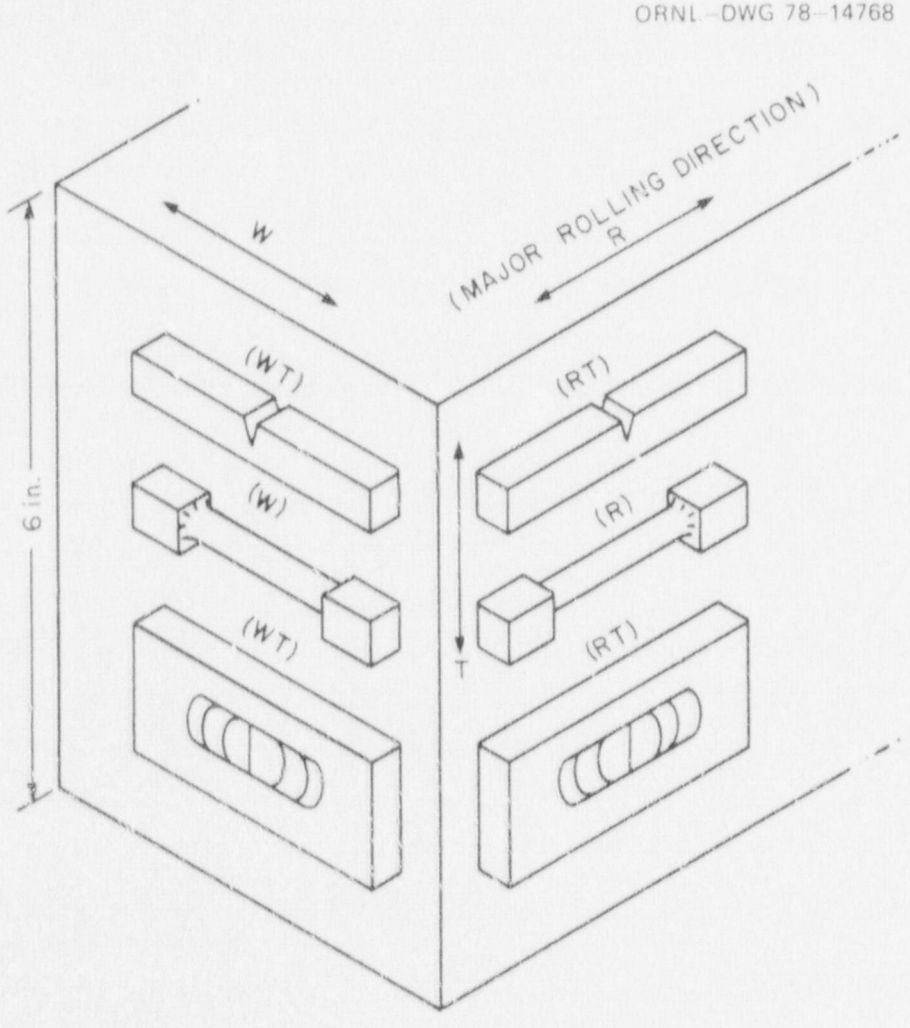

Fig. 18. Specimen orientation notation for HSST plates 03 and 04 and base plate from HSST weldment W57, showing tensile, Charpy V, and drop-weight specimens (1 in. = 25.4 mm).

reaustenitizing and quenching, 03JZ and 04BE were identified as AQ 03 and AQ 04, respectively. To avoid confusion, a lower-case t will be used to identify the through-the-thickness depth location in AQ 03 and AQ 04, and a capital T will refer to the depth in the original 152-mm-thick (6-in.) plate. This method of identification is shown in Fig. 19.

ORNL-DWG 78-14769

Fig. 19. Through-the-thickness depth location notations in AQ 03 and AQ 04 plates.

5.3 Tensile Results

Tensile properties were obtained with the 31.7-mm-gage-length (1.250-in.) by 4.52-mm-gage-diam (0.178-in.) subsize (MT) tensile specimen (L/D = 7). These specimens were tested at a strain rate of 0.016 min^{-1}. The tensile results obtained from the AQ 03 and W57 base plate using R- and W-oriented specimens tested at 20 and 93.3°C (68 and 200°F) are given in Table 1. As expected, large differences exist between the tensile properties of AQ 03 and 57V.

Table 1. Tensile properties of W57 base plate and through-the-thickness slices from as-quenched 03JZ

Specimen No.	Depth	Test temperature [°C (°F)]	Strength properties		Total elongation[a] (%)	Reduction in area (%)
			0.2% offset or lower yield [MPa (ksi)]	Ultimate tensile [MPa (ksi)]		
			W57 (R orientation)			
57V 50	0.40T	20.0 (68)	461 (66.9)	618 (89.7)	18.9	70.9
57V 52	0.59T	20.0 (68)	462 (67.0)	614 (89.1)	20.3	72.1
57V 49	0.31T	93.3 (200)	441 (63.9)	578 (83.9)	17.4	72.1
57V 51	0.49T	93.3 (200)	435 (63.1)	576 (83.6)	17.3	71.7
			W57 (W orientation)			
57V 54	0.40T	20.0 (68)	453 (65.7)	601 (87.2)	20.1	67.1
57V 53	0.31T	93.3 (200)	427 (62.0)	561 (81.3)	17.9	72.0
			AQ 03JZ (R orientation)			
03JZ 14	0.7t (0.2T)	20.0 (68)	1041 (151)[b]	1338 (194)	6.2	29.0
03JZ 17	0.7t (0.5T)	20.0 (68)	1138 (165)[b]	1434 (208)	7.6	44.7
03JZ 7	0.3t (0.2T)	93.3 (200)	1027 (149)[b]	1289 (187)	6.6	42.3
03JZ 10	0.3t (0.5T)	93.3 (200)	1138 (165)[b]	1496 (217)	6.3	29.1
			AQ 03JZ (W orientation)			
03JZ 38	0.3t (0.5T)	20.0 (68)	1069 (155)[b]	1400 (203)	8.0	35.3
03JZ 35	0.3t (0.2T)	93.3 (200)	1082 (157)	1358 (197)	3.7	13.5

[a] Ratio of gage length to gage diameter = 7; strain rate = 0.016 min^{-1}; gage length = 31.7 mm (1.250 in.).

[b] 0.2% offset yield.

A comparison of the tensile properties of R-oriented specimens shows that at room temperature, the average yield and ultimate stresses for the AQ 03 [1089 and 1386 MPa (158 and 201 ksi), respectively] were almost 2 1/2 times higher than the 57V values. The total elongation (6.9%) and the reduction in area (36.8%) were one-third and one-half, respectively. Increasing the test temperature to 93.3°C (200°F) resulted in small decreases in the yield and ultimate stresses and the total elongation, but there was no significant change in the reduction in area of 57V. No significant changes in tensile properties were observed at the higher temperature for AQ 03. A comparison of the tensile results from the R and W orientations at room temperature indicate slightly lower strength and reduction in area and slightly higher total elongation in both materials.

5.4 Charpy V-Notch Impact Results

Initially, the exact location of the flaws in the crack-arrest models was to be determined by a review of the mechanical properties of both materials. However, it was established that the fracture plane would be axial (as discussed in Chapter 3), and this fracture-path orientation is perpendicular to the original plate surfaces. Therefore, the properties were determined in the WT and RT directions with respect to the original plate orientations.

Charpy V impact test results from the RT- and WT-oriented specimens taken from the W57 base metal are shown in Fig. 20. The data for each test point shown in Fig. 20 are given in Appendix C, Table C.1. The transition region appears to be independent of plate orientation (R and W) and occurs between -50 and 50°C (-50 and 100°F). The upper-shelf toughness appears to be dependent on orientation, and the lowest values of upper-shelf energies were obtained for the WT orientation. The onset of upper-shelf energy occurs at about 50°C (122°F). The upper-shelf energy values are about 172 J (127 ft-lb) and 149 J (110 ft-lb), respectively, for the RT- and WT-oriented specimens.

The Charpy V impact test results for the 0.3t and 0.7t depth in AQ 03 were also obtained with RT- and WT-oriented specimens. These

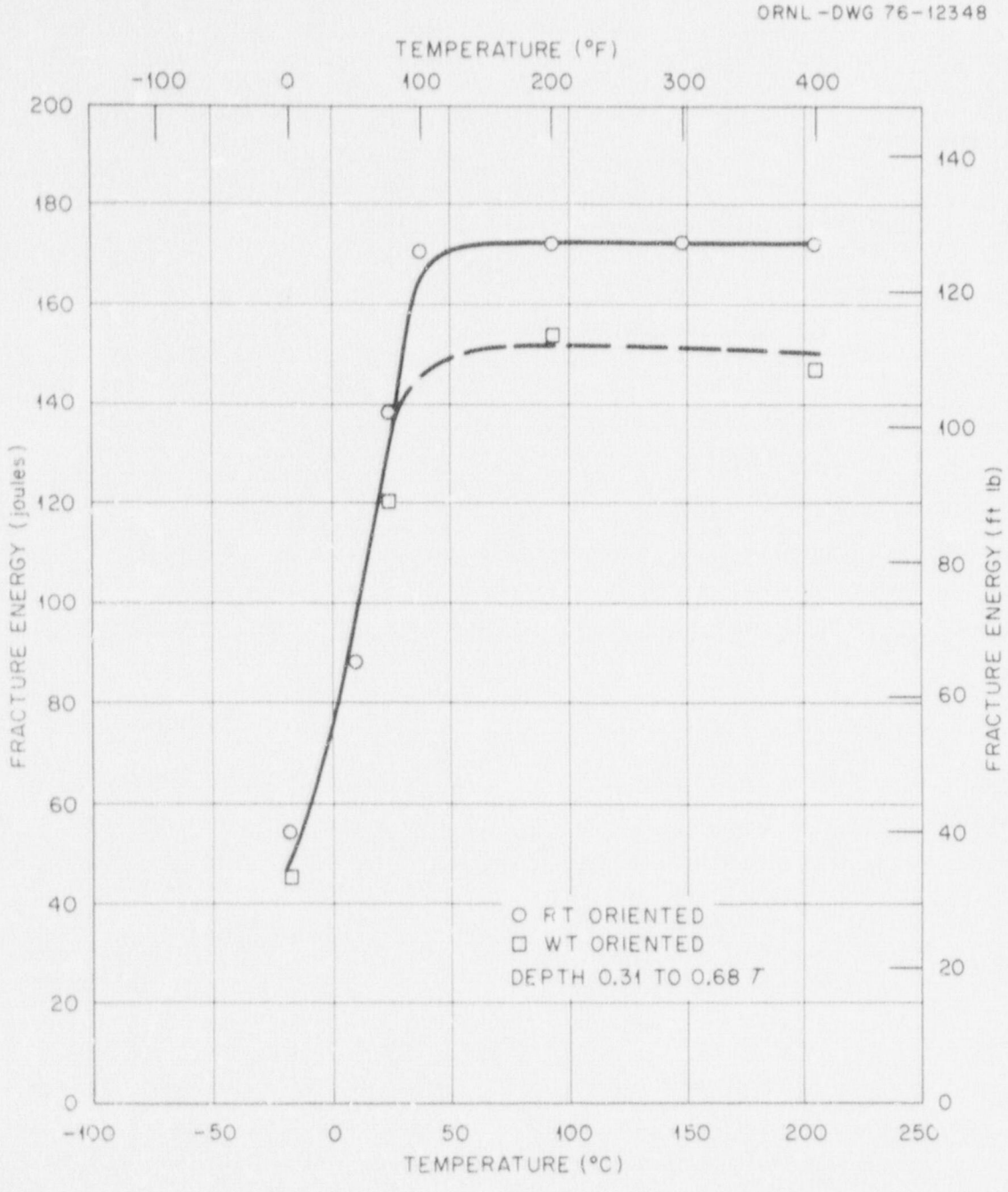

Fig. 20. Variation of Charpy V impact energy with temperature for W57 base plate.

results are listed in Table C.1 and shown in Fig. 21. The Charpy curves for W57 are included in Fig. 21, and the impact energies of the two materials can be compared. The 44-mm-thick (1 3/4-in.) AQ 03 does not exhibit a distinct brittle-to-ductile transition. Further, the impact

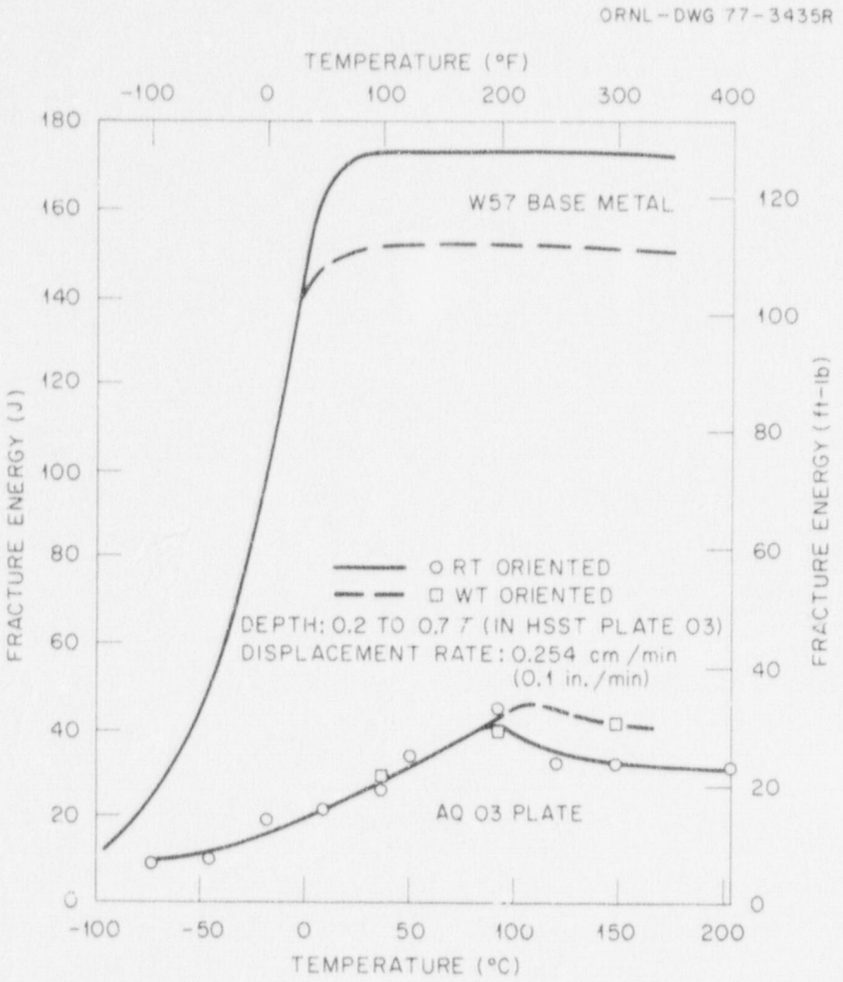

Fig. 21. Variation of Charpy V impact energy for 44-mm-thick (1 3/4-in.) through-the-thickness slices from plate section 03JZ after reaustenitizing for 1 1/2 hr and water quenching. The specimens were all from the 0.3t and 0.7t depth locations in the 44-mm sections. Impact energies for the quenched-and-tempered W57 material are also shown for comparison.

energy in the transition appears to be unaffected by orientation. The upper-shelf energy of AQ 03 is dependent on the original plate orientation; however, unlike the upper-shelf behavior of the W57 base metal, lower upper-shelf values were obtained with the RT orientation. The upper-shelf energy for the WT- and RT-oriented specimens is about 45 J (33 ft-lb) and 41 J (30 ft-lb), respectively; the onset of upper-shelf energy occurs at about 93°C (200°F). The difference between the upper-shelf Charpy V energy of the high- and low-toughness materials is about

133 J (98 ft-lb) in the RT orientation and about 107 J (79 ft-lb) in the WT orientation. At 38°C (100°F) the difference in impact energy between the low-toughness material and the RT and WT orientations of the W57 base plate is 146 and 125 J (108 and 92 ft-lb), respectively.

The AQ 04 plate was included, since limited Charpy V impact results indicated that this material might exhibit poorer transition toughness properties (higher transition temperatures) than the AQ 03 plate. The results from 38-mm-thick (1 1/2-in.) AQ 04 plate are compared with the AQ 03 plate results in Fig. 22. The impact data for each specimen are listed in Table C.1. Because of the limited amount of material and dimensional problems, only W-oriented specimens were prepared. The impact properties of AQ 04 appear to be poorer than those of AQ 03. Based on the fracture appearance of the AQ 04 specimens, the transition region is between -46 and 149°C (-50 and 300°F) and the onset of upper-shelf energy is about 37 J (27 ft-lb).

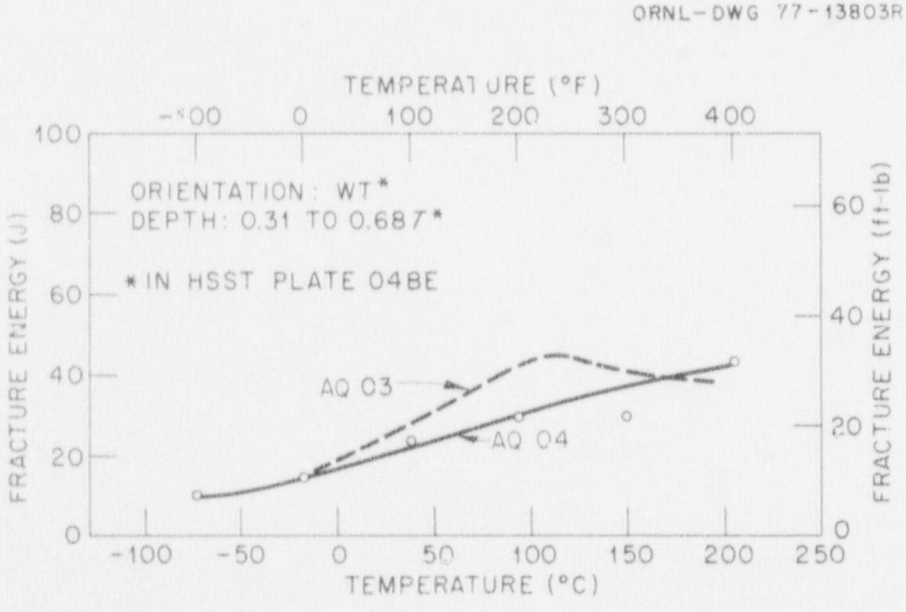

Fig. 22. Variation of Charpy V impact energy with temperature for 38-mm-thick (1 1/2-in.) through-the-thickness slices from plate section 04BE after reaustenitizing for 1 1/2 hr at 981°C (1600°F) and water quenching. For comparison, the trend line for the AQ 03 data is also shown.

5.5 Fracture Toughness

The static and dynamic fracture toughness of precracked Charpy V specimens from the RT and WT orientations of the W57 base plate are shown in Fig. 23 and listed in Tables C.2 and C.3 of Appendix C. The dynamic results from the RT-oriented specimens show that the transition region at the 150 $MN \cdot m^{-3/2}$ (136 $ksi \cdot in.^{1/2}$) level occurs at a temperature about 56°C (100°F) higher than that for the static transition region

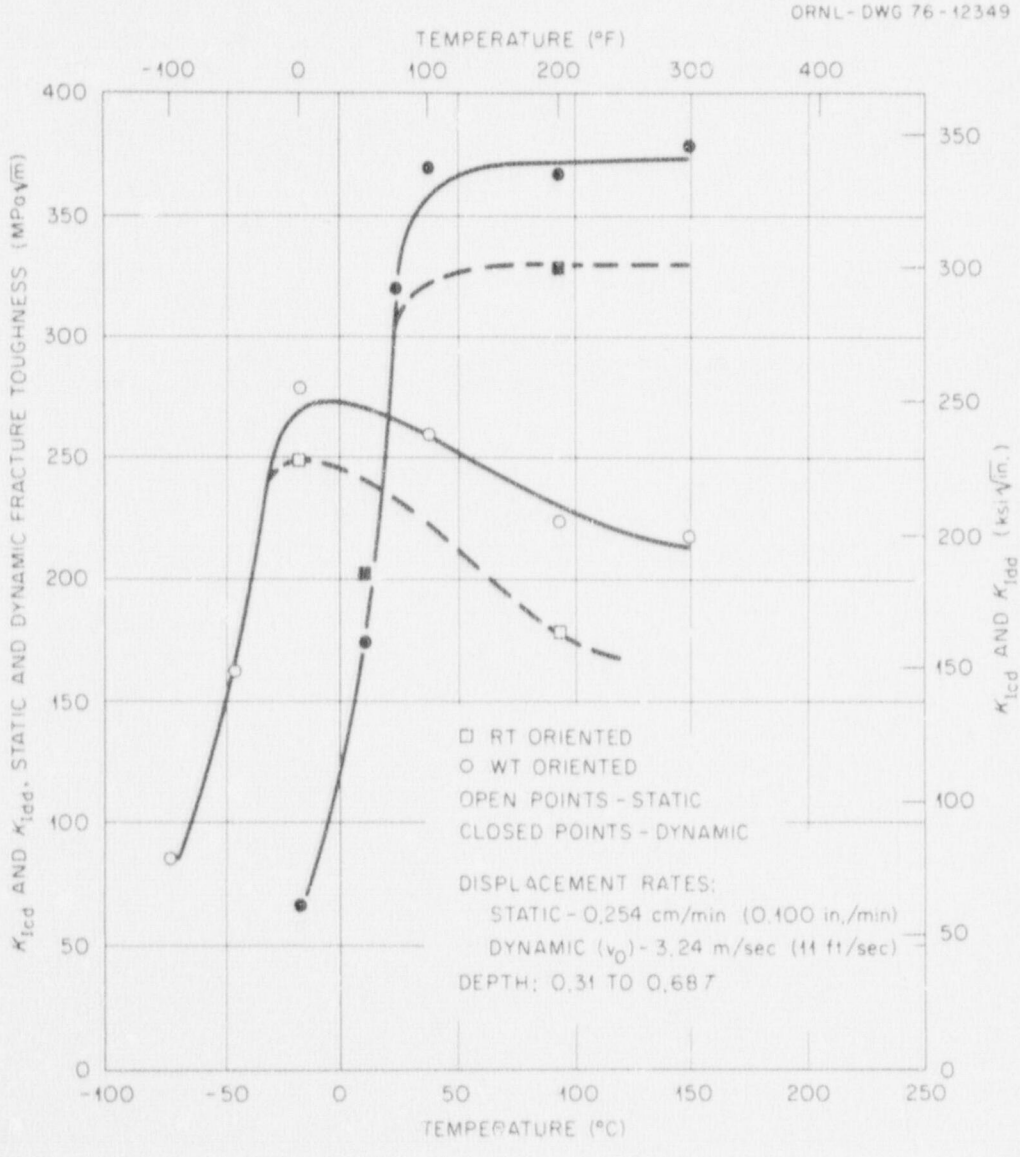

Fig. 23. Variation of precracked Charpy V static and dynamic fracture toughness with temperature for W57 base plate.

[-51°C (-60°F) and 44°C (40°F), respectively] and that the upper-shelf energies at the onset of upper-shelf conditions increased from 275 $MN \cdot m^{-3/2}$ (250 $ksi \cdot in.^{1/2}$) to 374 $MN \cdot m^{-3/2}$ (340 $ksi \cdot in.^{1/2}$). Also, the upper-shelf behavior under dynamic conditions tends to remain fairly constant to 149°C (300°F), while the static upper-shelf values drop fairly rapidly to 220 $MN \cdot m^{-3/2}$ (200 $ksi \cdot in.^{1/2}$) at 149°C. The fracture toughness results from WT-oriented specimens show behavior similar to the Charpy V impact results — no significant difference in the transition regions but lower upper-shelf values for the WT than for the RT orientation.

The static and dynamic fracture toughness of precracked Charpy V specimens from the RT and WT orientations in AQ 03 are shown in Fig. 24 and listed in Tables C.2 and C.3. The K_{Icd} transition regions are the

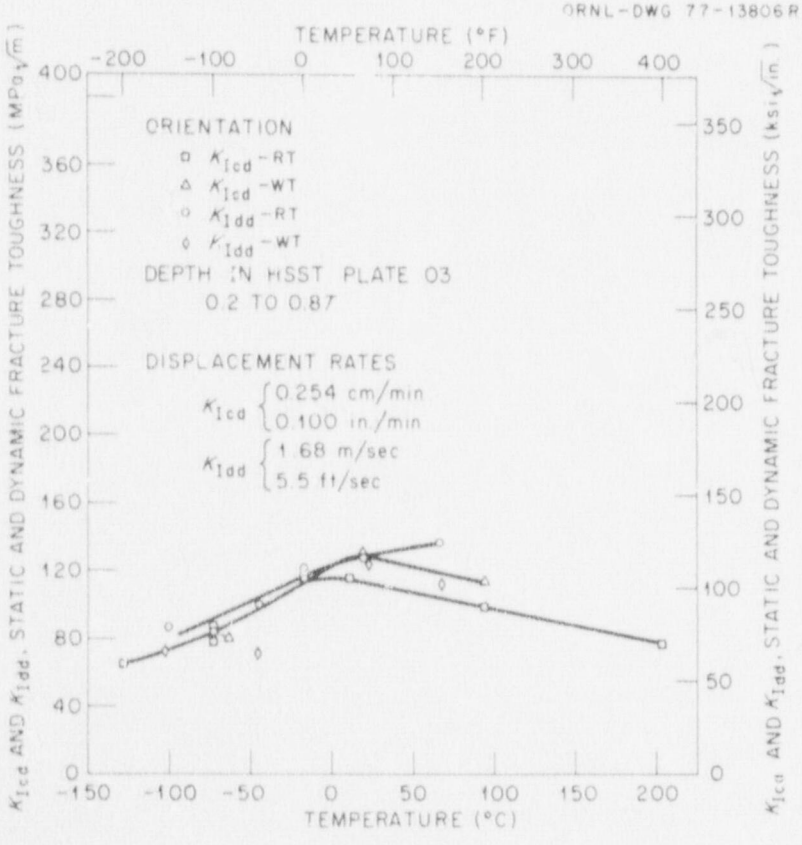

Fig. 24. Variation of precracked Charpy V static and dynamic fracture toughness with temperature for 44-mm-thick (1 3/4-in.) through-the-thickness slices from plate section 03JZ after reaustenitizing for 1 1/2 hr at 876°C (1600°F) and water quenching.

same for both orientations and extend from about -3.9°C (25°F) to below -129°C (-200°F). The upper-shelf K_{Icd} toughness is dependent on orientation. Toughness values of 115 $MN \cdot m^{-3/2}$ (105 $ksi \cdot in.^{1/2}$) at -18°C (0°F) and 130 $MN \cdot m^{-3/2}$ (118 $ksi \cdot in.^{1/2}$) at 10°C (50°F) were obtained for the RW and RT orientations, respectively. The K_{Idd} results from RT-oriented specimens are not significantly different from both K_{Icd} orientations in the transition region but indicate a slightly higher upper shelf. A comparison of the K_{Idd} results from both orientations indicate that the WT transition region occurs at slightly higher temperatures and the upper-shelf toughness is slightly lower.

The static-fracture-toughness results from the W57 base plate and the AQ 03 are compared in Fig. 25. The maximum difference [about 159 $MN \cdot m^{-3/2}$ (145 $ksi \cdot in.^{1/2}$)] is in the RT orientation and occurs at about -12°C (10°F).

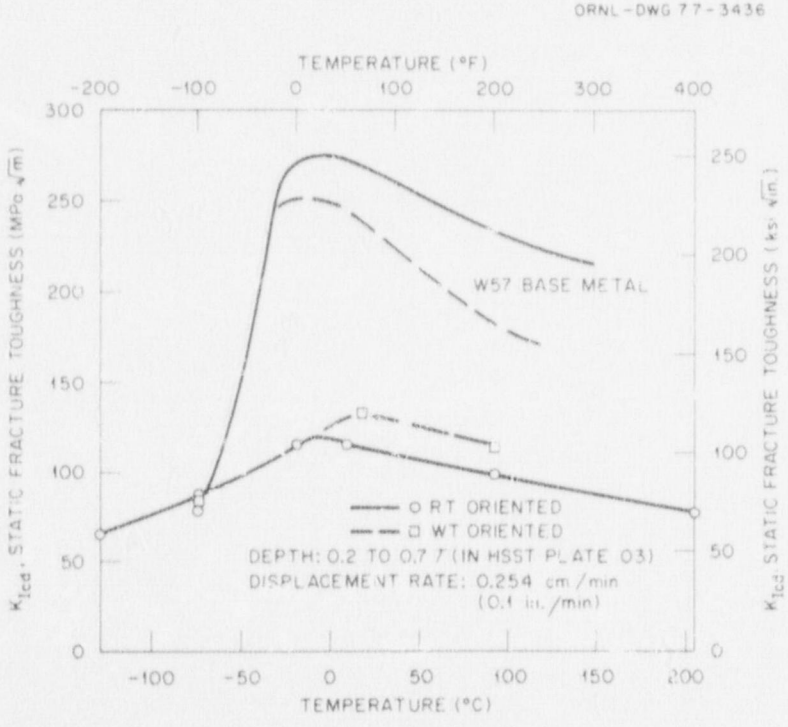

Fig. 25. Variation of precracked Charpy V static fracture toughness with temperature for 44-mm-thick (1 3/4-in.) through-the-thickness slices from plate section 03JZ after reaustenitizing for 1 1/2 hr at 876°C (1600°F) and water quenching. The precracked Charpy V static fracture toughness trend line is also shown for comparison.

The static and dynamic fracture toughness results for WT-oriented specimens from AQ 04 are shown in Fig. 26, and the individual test results are listed in Tables C.2 and C.3. The dynamic fracture toughness is superior to the static fracture toughness. The K_{Idd} temperature at the 82 $MN \cdot m^{-3/2}$ (75 $ksi \cdot in.^{1/2}$) toughness level is 42°C (75°F) lower than the K_{Idd} value, -73 and -32°C (-100 and -25°F), respectively. The K_{Idd} upper shelf is about 11 $MN \cdot m^{-3/2}$ (10 $ksi \cdot in.^{1/2}$) higher than the K_{Icd} upper shelf, 115 and 104 $MN \cdot m^{-3/2}$ (105 and 95 $ksi \cdot in.^{1/2}$), respectively, at 38°C (100°F). A comparison of the AQ 03 and AQ 04 fracture toughness results (i.e., Figs. 24 and 26) indicates that the static fracture toughness of the AQ 04 is somewhat poorer than that of the AQ 03.

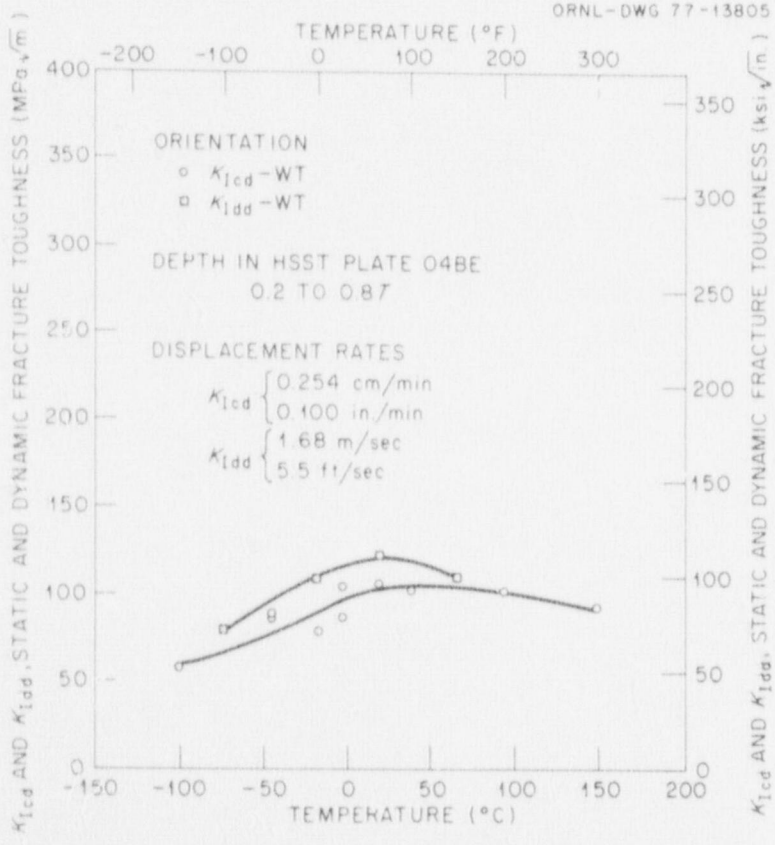

Fig. 26. Variation of precracked Charpy V static and dynamic fracture toughness with temperature for 38-mm-thick (1 1/2-in.) through-the-thickness slices from plate section 04BE after reaustenitizing for 1 1/2 hr at 871°C (1600°F) and water quenching.

The static fracture toughness of the AQ 03 and the W57 base plate was also determined with 0.394T and 1T compact specimens. All calculations were made in accordance with ANSI/ASTM E-399-74 (Ref. 18) for compact specimens, with the load P_Q being given the value P_{EE} as prescribed by the equivalent-energy method for calculating fracture toughness. The equivalent-energy method is described in Appendix C. The J integral (J) was obtained by extrapolating crack-opening displacement values from the front face. The Merkle-Corten relationship[19] was used for the J calculation, and K_J was calculated from J using the expression provided in Appendix C. Results from the AQ 03 and the W57 base plate are all listed in Table 2; where comparison is possible, the static fracture toughnesses compare very well with the static fracture toughness results obtained with precracked Charpy specimens.

5.6 Drop-Weight Measurements

The nil-ductility temperature (NDT) for the W57 base plate was determined in accordance with ASTM E-208-69 (Ref. 20), using RT- and WR-oriented type P-2 drop-weight specimens. The test results at the 1/4T and 3/4T depth locations are given in Appendix C (Table C.4). An NDT between -23.3 and -28.9°C (-10 and -20°F) was obtained for both the RT- and WR-oriented specimens. Because of the limited number of WT specimens, the NDT for this orientation was not obtained.

5.7 Hardness Measurements

Since the fabrication of the small crack-arrest models involved joining the various shell components by electron-beam (EB) welding, an investigation was made of the hardness distribution across the fusion line of an EB weld that joined a quenched-and-tempered plate to a quenched-only plate. The heat treatments were representative of the treatments that the high-toughness (cylinders machined from the W57 base plate) and low-toughness portions of the small crack-arrest models received prior to fabrication. The EB welding procedure was also typical of that which was used to join the cylinders. Both plates were 38-mm-thick (1 1/2-in.) sections of plate 03; the high-toughness material was

Table 2. Static fracture toughness results from compact specimens of as-quenched 03JZ and W57 base plate

Specimen No.	Type	Depth	Orientation	Test temperature [°C (°F)]	K_{Icd} [MN·m$^{-3/2}$ (ksi·in.$^{1/2}$)]	J [kJ/m^2 (in.-lb/in.^{2})]	K_J [MN·m$^{-3/2}$ (ksi·in.$^{1/2}$)]
				As-quenched plate 03JZ			
03JZ 1	1T	0.5t (0.3T)	RT	4.4 (40)	140 (127)	96.4 (551)	142 (129)
03JZ 2	1T	0.5t (0.7T)	RT	-45.6 (-50)	97 (89)	45.8 (262)	98 (89)
03JZ 4	0.394T	0.3t (0.4T)	RT	-101 (-150)		20.5 (117)	65 (59)
03JZ 6	0.394T	0.7t (0.4T)	RT	-20.6 (-5)	133 (121)	85.9 (491)	133 (121)
				W57 base plate			
57V 1	1T	0.4T	RT	-45.6 (-50)	165 (150)	126 (721)	162 (147)
57V 2	1T	0.6T	RT	-73.3 (-100)	102 (93)	48.0 (274)	100 (91)
57V 3	0.394T	0.4T	RT	-45.6 (-50)	115 (105)	64.9 (371)	116 (106)
57V 4	0.394T	0.6T	RT	-73.3 (-100)	91 (82)	39.9 (228)	91 (83)
57V 56	0.374T	0.5T	RT	-129 (-200)	55 (50)	14.7 (84)	55 (50)

as received (quenched and tempered), and the low-toughness material was reaustenitized 1 1/2 hr at 871°C (1600°F) and water quenched. These materials and heat treatments were identical to 57V and AQ 03 previously discussed. Presented in Fig. 27 is a macrophotograph of the major portion of a cross section of the EB weld, showing the location of the indentations from a hardness traverse that was made across the weldment. The hardness indentations were made at 0.254-mm (0.010-in.) intervals and extended from the center of the fusion zone into the quenched material. The hardness values are listed in Table 3. The distribution of the diamond pyramid hardness (DPH) values in the various zones of the weldment are shown in Fig. 28. The regions identified in Fig. 28 can be correlated with the microstructures shown in Fig. 27. These results show that the highest values (508 DPH) occur in the fusion zone and the

Table 3. Diamond pyramid hardness (DPH) values across the heat-affected zone of the electron-beam weld to be used in joining the small crack-arrest models

Indentation location No.	Diamond pyramid hardness	Rockwell C scale hardness[a]	Indentation location No.	Diamond pyramid hardness	Rockwell C scale hardness[a]
1	406	41.5	21	298	29.5
2	406	41.5	22	283	27.5
3	460	46.1	23	302	30.0
4	394	40.3	24	351	35.7
5	453	45.7	25	327	32.9
6	491	48.5	26	323	32.4
7	508	49.7	27	351	35.7
8	425	43.2	28	382	39.1
9	388	39.7	29	361	36.8
10	341	34.6	30	346	35.2
11	439	44.5	31	341	34.6
12	341	34.6	32	366	37.4
13	336	34.0	33	377	38.6
14	314	31.5	34	400	40.8
15	291	28.6	35	388	39.7
16	298	29.5	36	412	42.0
17	298	29.5	37	412	42.0
18	314	31.5	38	382	39.1
19	351	35.7	39	412	42.0
20	366	37.4	40	419	42.7

[a]Converted from DPH values, using equivalent hardness values from *Metals Handbook*, 8th Edition, ASTM, pp. 1234-35, 1961.

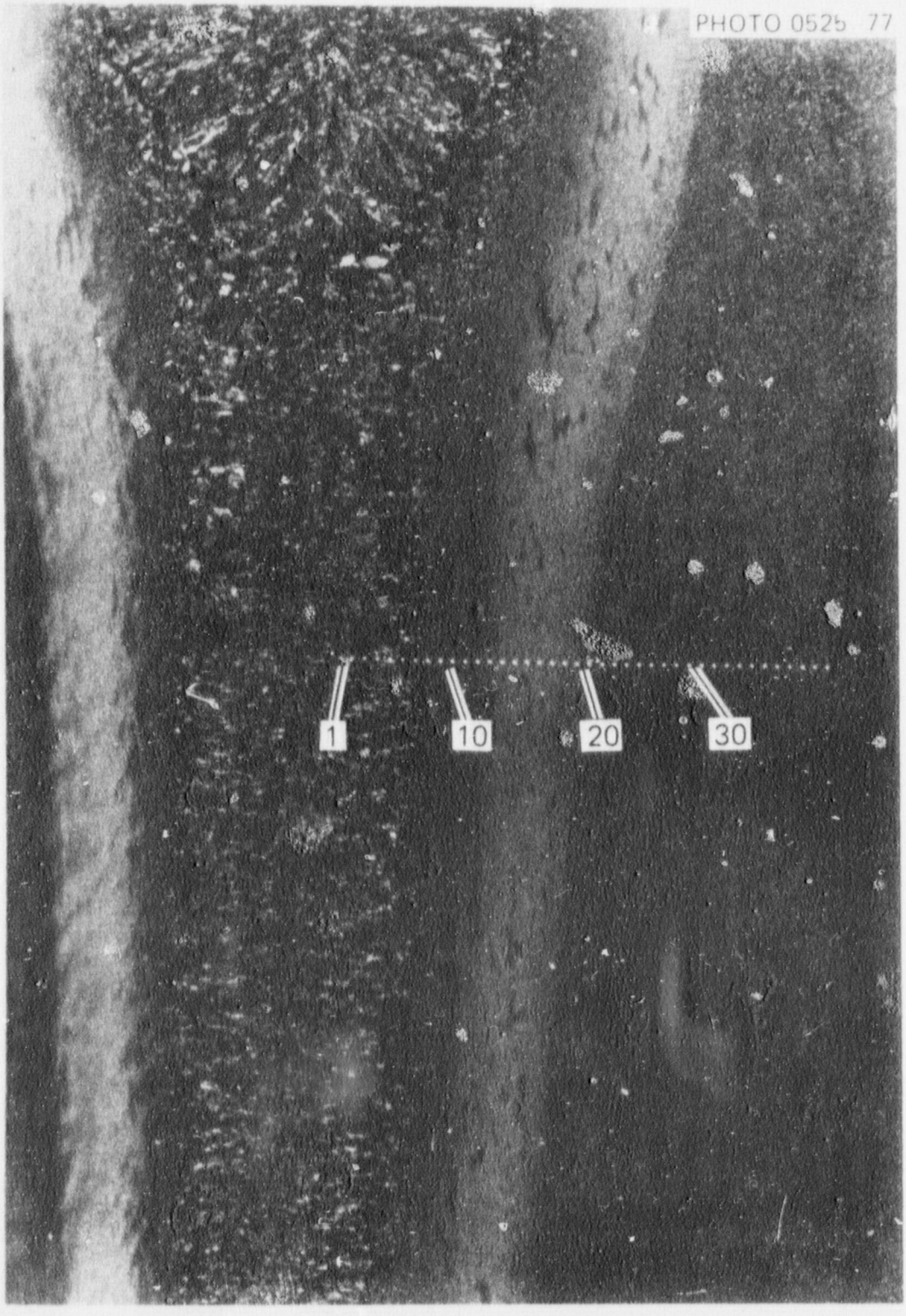

Fig. 27. Location of diamond pyramid hardness indentations across the heat-affected zone and adjacent areas of a cross section of the electron-beam weld to be used in joining the cylinders for the 254-mm (10-in.) crack-arrest models. (Original reduced 21%)

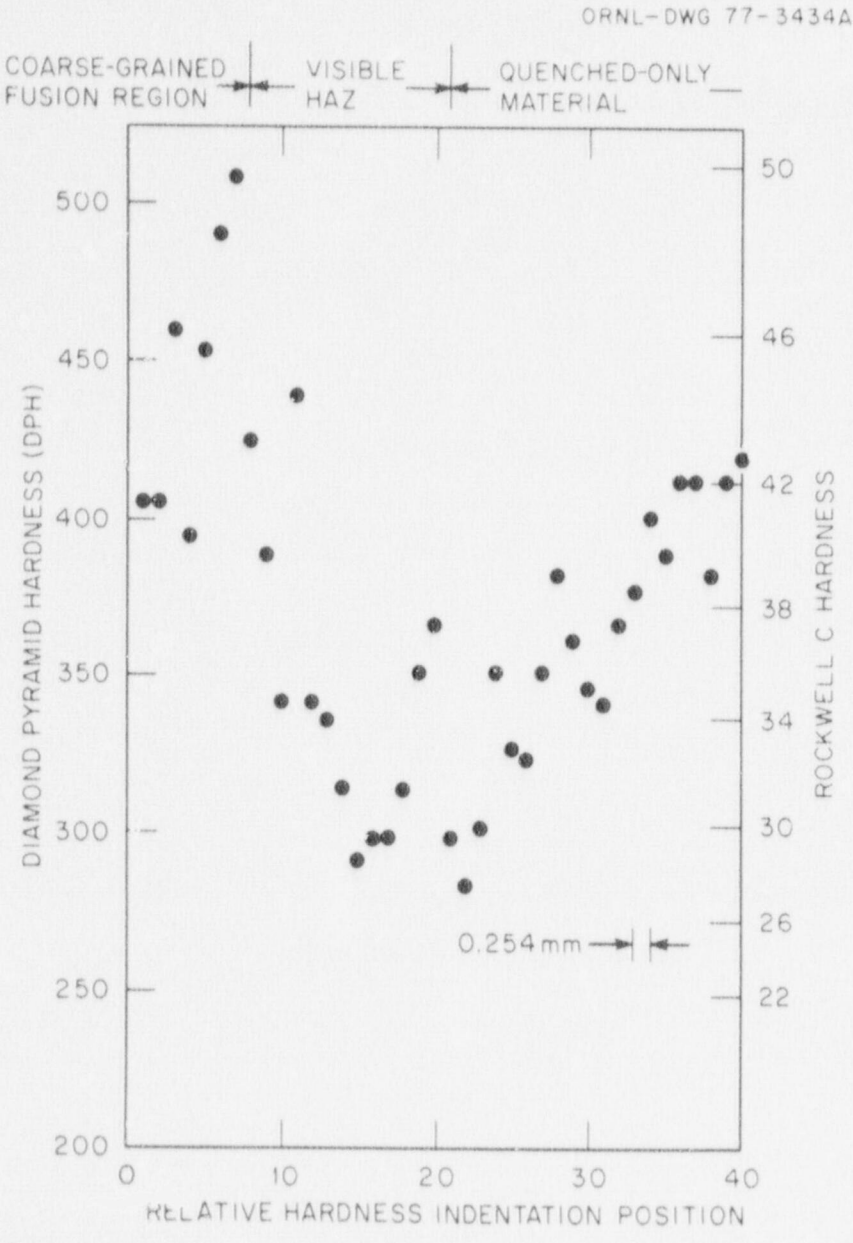

Fig. 28. Hardness traverse across the electron-beam weld to be used in joining the cylinders for the 254-mm (10-in.) crack-arrest models.

lowest values (300 DPH) occur in the optically visible heat-affected zone (HAZ) in the quenched material. The hardness of the quenched-only base material is higher than that of its HAZ. These results suggest that the EB weld has tempered and quenched material. The hardness of the quenched, tempered, and postweld heat-treated plate (W57) is about 200 DPH.

5.8 Cooling Rate Effects

Because of the higher apparent toughness of the as-quenched crack-arrest material relative to the thermal shock as-quenched material (discussed in Chapter 3 and illustrated in Fig. 8), it was decided to investigate the effect of slower cooling rates (from the austenitizing temperature) on the Charpy V impact energy and the precracked Charpy V static fracture toughness of plate 03. A portion of the 44-mm-thick (1 3/4-in.) slices from the AQ 03 plate containing through-the-thickness cracks were cut into 13-mm-square (1/2-in.) DATA TRAK specimen blanks. [Before the AQ 03 plate was cut, it was tempered for 2 hr at 649°C (1200°F) and cooled in still air. This tempering treatment was performed solely to soften the material, thereby facilitating the preparation of the DATA TRAK specimen blanks.] The specimen blanks were heat treated in the DATA TRAK facility at 871°C (1600°F) for 1 hr and then program cooled to ambient temperature. Programmed cooling rates of 0.5, 0.9, and 9.4 K/sec (0.9, 1.6, and 17°R/sec) were investigated. These rates represent estimates of the 1/4-thickness cooling rates in 254-, 203-, and 38-mm-thick (10-, 8-, and 1 1/2-in.) plates, respectively.

Charpy V impact results from RT-oriented specimens are shown in Fig. 29. The test results are given in Table C.1 (Appendix C). There is a major difference between the Charpy V impact energy of the slowly cooled specimens (0.5 and 0.9 K/sec) and the rapidly cooled (9.4 K/sec) specimens, particularly in their upper-shelf energy values. As a consequence of the slow cooling rates, the upper-shelf energy has increased to 127 J (94 ft-lb) [from about 40 J (30 ft-lb)], and the transition temperature [for 27 J (20 ft-lb)] has shifted to lower temperatures [from 37.7 to 15.6°C (100 to 60°F)]. The 9.4-K/sec cooling rate yields a microstructure similar to that obtained in the 38-mm-thick (1 1/2-in.) water-quenched material which was used for the crack-initiation portion of the crack-arrest models. For comparison, the Charpy V data from the 44-mm (1 3/4-in.) water-quenched plate are also plotted in Fig. 29.

The K_{Icd} toughness values from an RT-oriented specimen receiving the same heat treatments as the Charpy V specimens are shown in Fig. 30. Above the 93 $MN \cdot m^{-3/2}$ (85 $ksi \cdot in.^{1/2}$) toughness level, the slower cooling

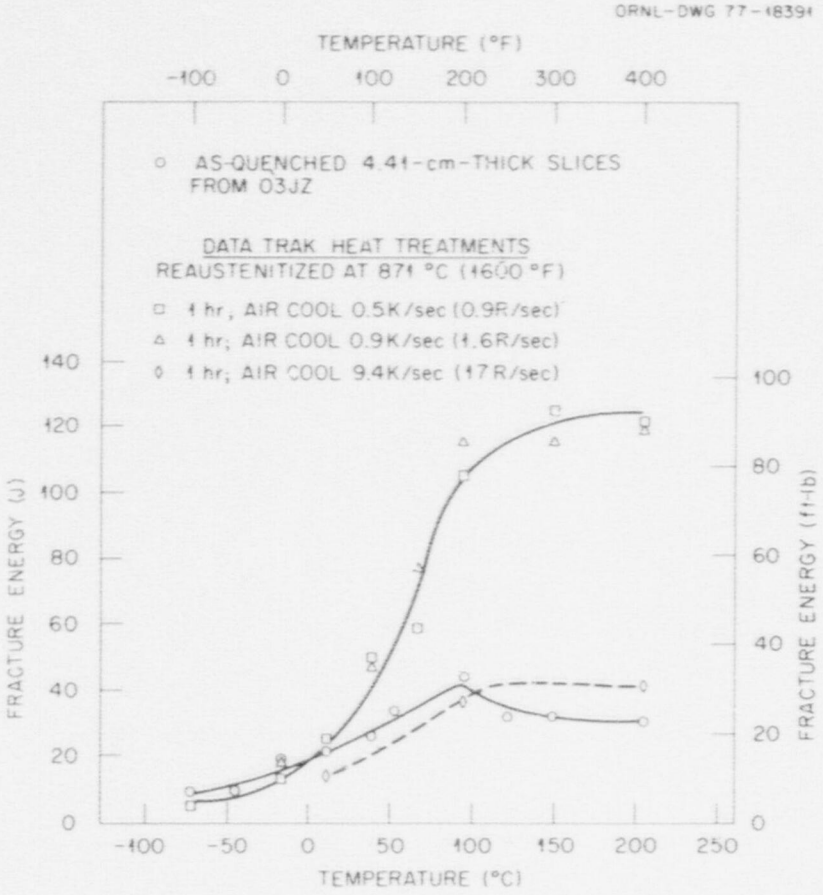

Fig. 29. Effect of cooling rate on the Charpy V impact properties of HSST plate section 03JZ after reaustenitizing at 871°C (1600°F) for 1 hr and program cooling (1 cm = 0.394 in.).

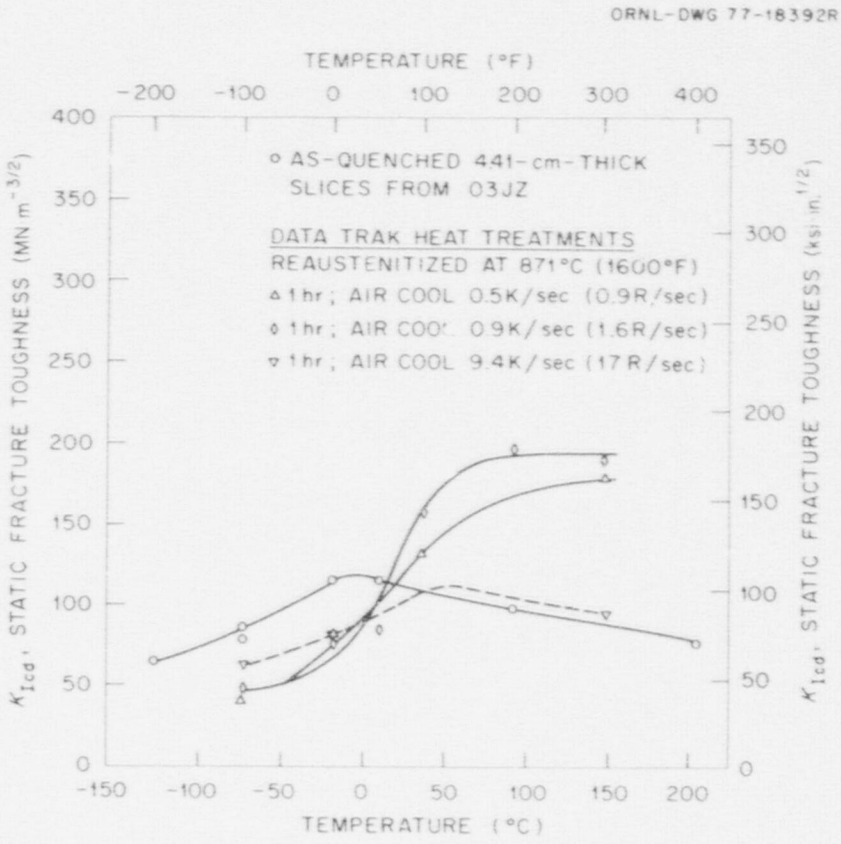

Fig. 30. Effect of cooling rate on the precracked Charpy V static fracture toughness properties of HSST plate section 03JZ after reaustenitizing at 871°C (1600°F) for 1 hr and program cooling.

rates yield superior fracture toughness at a given temperature. The 0.9-K/sec cooling rate provided the highest upper-shelf values. At 149°C (300°F), the upper-shelf toughness values for 0.9, 0.5, and 9.4 K/sec were 188, 179, and 95 $MN \cdot m^{-3/2}$ (171, 163, and 86 $ksi \cdot in.^{1/2}$), respectively. Below 93 $MN \cdot m^{-3/2}$ (85 $ksi \cdot in.^{1/2}$), the specimens that were cooled faster exhibited higher fracture toughness values. At -73°C (-100°F), the fracture toughness of the 9.4-K/sec specimens was 19 $MN \cdot m^{-3/2}$ (17 $ksi \cdot in.^{1/2}$) higher than the average of the specimens subjected to slower cooling rates.

The fracture toughness results from the 44-mm-thick (1 3/4-in.) AQ 03 are also plotted in Fig. 30 for comparison with the data from the DATA TRAK specimens. Upper-shelf fracture toughnesses compare well; however, the values for the specimens cooled at 9.4 K/sec are 67°C (120°F) higher than the AQ 03 values at the 93 $MN \cdot m^{-3/2}$ fracture toughness level. Therefore, the probability exists that the fastest cooling rate attained in the DATA TRAK facility is not as rapid as the actual cooling rate that the 44-mm-thick (1 3/4-in.) AQ 03 experienced during the quench.

Tensile properties were also obtained with R-oriented (MT) tensile specimens machined from blanks which had been cooled at 0.9 K/sec. The results from these specimens, which were tested over a temperature range of -73.3 to 37.8°C (-100 to 100°F), are listed in Table 4.

Table 4. Tensile properties of plate section 03JZ after reaustenitizing at 871°C (1600°F) for 1 hr and air cooling at 0.9 K/sec (1.6°R/sec)

Specimen No.	Depth	Orientation	Test temperature [°C (°F)]	Strength properties		Total elongation[a] (%)	Reduction in area (%)
				0.2% offset yield [MPa (ksi)]	Ultimate tensile [MPa (ksi)]		
03JZ 83	0.7t (0.7T)	R	-45.6 (-50)	834 (121)	1082 (157)	8	47
03JZ 87	0.7t (0.9T)	R	37.8 (100)	758 (110)	979 (142)	11	57
03JZ 89	0.7t (0.2T)	R	-73.3 (-100)	841 (122)	1110 (161)	13	56
03JZ 93	0.7t (0.2T)	R	10.0 (50)	786 (114)	1020 (148)	11	56
03JZ 14[b]	0.7t (0.2T)	R	20.0 (68)	1040 (151)	1340 (194)	62	29

[a] Ratio of gage length to gage diameter = 7; strain rate = 0.016 min^{-1}; gage length = 31.7 mm (1.250 in.).

[b] The tensile results from the as-received 44-mm-thick (1 3/4-in.) section from plate 03. These results can be compared to those obtained from 03JZ 93.

6. TEST TEMPERATURE SELECTION

The preliminary analysis that was used in designing the crack-arrest models (Chapter 3) was made using the material property data for quenched-only material obtained as part of the ORNL Thermal Shock Program. When the actual material properties became available (Chapter 5), it was necessary to reevaluate the test configuration and to select test temperatures that would most satisfactorily meet the test objectives. This chapter discusses that reevaluation and the selection of test temperatures.

It will be recalled that the objective for the first three model tests was to demonstrate dynamic crack propagation followed by arrest in one test and nonarrest in another, with the third model intended to serve as a backup if any difficulty was encountered in either the arrest or nonarrest experiments. The order in which arrest and nonarrest would be demonstrated was not considered critical except that the preliminary analysis indicated that an arrest would probably be the most difficult to achieve and had the greatest uncertainty; therefore, demonstration of arrest was made the objective of the first test. Thus, if the first test resulted in nonarrest, there might be some latitude to configure the second test for another try at demonstrating arrest.

It should also be noted that if the objective of demonstrating arrest and nonarrest were met in what was termed the first phase (i.e., the first three model tests), there would be a second phase of testing, involving additional models to more accurately bracket the demarcation between arrest and nonarrest events.

The criterion for crack arrest, as discussed in Chapter 3, required that the arrest toughness of the material, K_{Im}, exceed the stress-intensity factor that would be calculated for the anticipated arrest crack length; that is,

$$K_{Im} > K_I(a_f) \ , \tag{9}$$

where a_f is the final or arrested crack length. As discussed earlier, it is convenient to employ the criterion for crack initiation in the

brittle material to normalize Eq. (9). Thus, the criterion for arrest becomes

$$\frac{K_{Im}}{K_{Ic}} > \frac{K_I(a_f)}{K_I(a_i)} , \tag{10}$$

where a_i is the crack length at initiation.

The principal result of the preliminary analysis described in Chapter 3 is a plot of Eq. (10) vs temperature, which is shown in Fig. 11. A crucial point to be made about Fig. 11 is that the value for K_{Ic} was the best available (i.e., the thermal shock data) at the time the models were being designed. It was expected that the quenched-only material of the actual crack-arrest model would have lower K_{Ic} values, which would tend to raise the curves in Fig. 11 and thus enhance the prospects for arrest.

The material property data pertaining to the quenched-only material was obtained from specimens machined from the same plates which had been used for the brittle cylindrical section. Those specimens also received quenching that was identical to that received by the brittle sections.

Figure 31 shows a plot of the Charpy impact energy data for quenched-only plates 03 and 04 and the Charpy impact energy for the material that was used to generate the K_{Ic} curve in Fig. 8 (i.e., the K_{Ic} curve that was used for the pretest analysis summarized in Fig. 11). The thermal shock data in Fig. 31 separates from the crack-arrest model data at about 93°C (200°F), and that separation depends on the distance of the thermal shock specimens from the plate surface. For specimens very close to the surface, which presumably had a higher cooling rate than material close to the center of the plate, the upper-shelf impact energy is substantially lower than that for the center material. The quenched-only material in the models would also experience very rapid cooling during the quench, which probably accounts for the low upper-shelf impact energy. One unexpected feature of the data presented in Fig. 31 was the apparent trend of higher impact energies for quenched-only model materials at temperatures below 100°F.

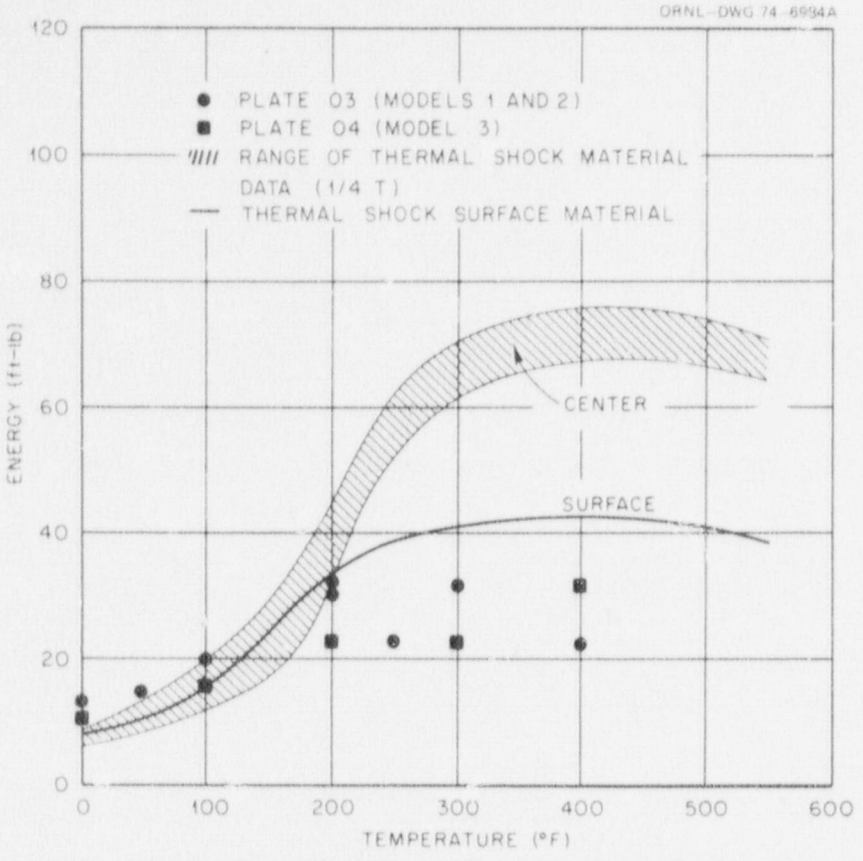

Fig. 31. Effect of plate thickness during quenching on Charpy V impact energies of quenched-only A533B steel [1 ft-lb = 1.36 J; °C = 5/9 (°F - 32)].

Figure 32 shows comparable slow-bend precracked Charpy specimen toughnesses for the quenched-only model material and for the thermal shock material. The data in Fig. 32 was quite surprising at the time in that the very rapidly quenched material had much higher static fracture toughnesses, at least in the transition region, than did the thermal shock material. Originally, it had been planned that only HSST plate 03 in the quenched-only state would be used for the crack-arrest models. After data such as that shown in Fig. 32 was developed, it was decided that HSST plate 04 should also be used for the third model test to see if the unexpected high toughness of the quenched-only model material was due to the difference in cooling rates during quenching or to some anomaly associated with either HSST plate 03 or the A533 material (HSST plate 04) used in the thermal shock study.

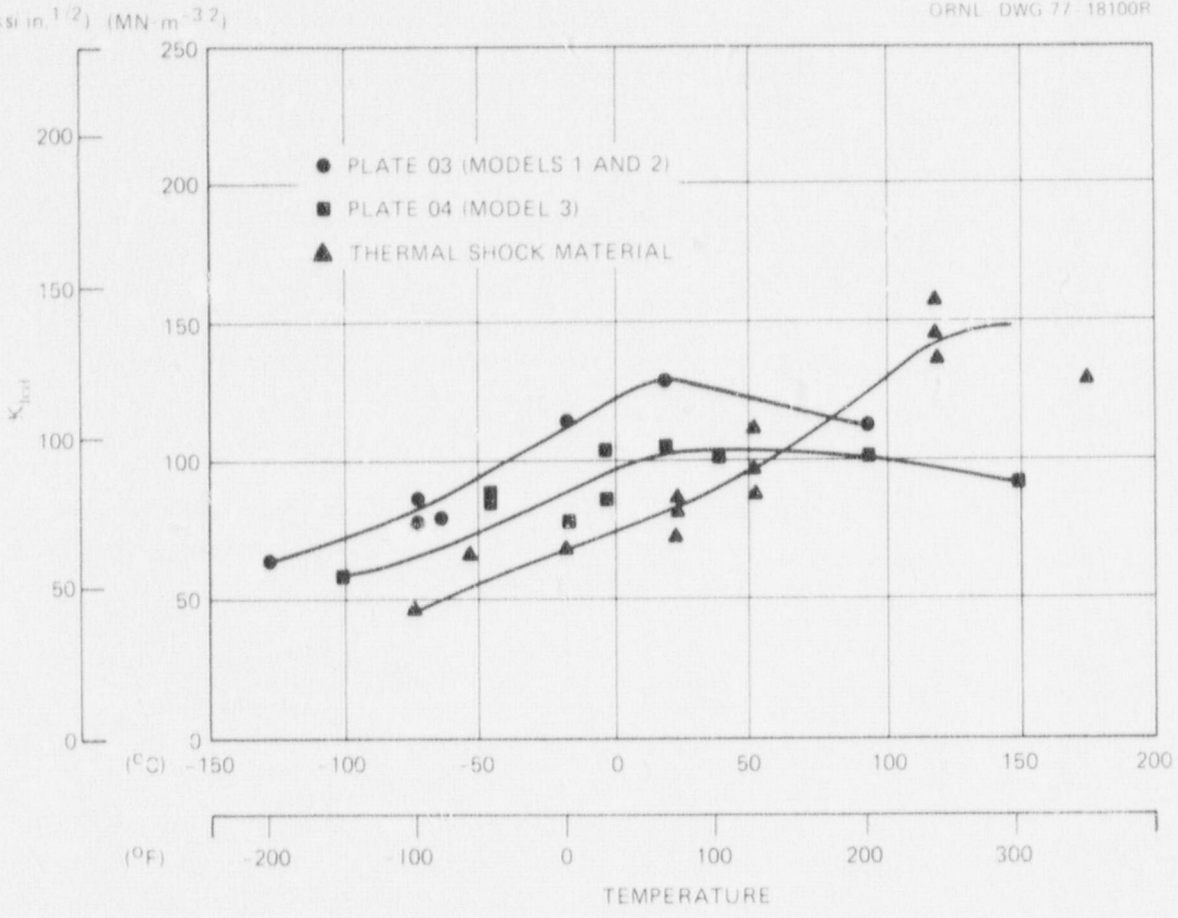

Fig. 32. Slow-bend precracked Charpy specimen toughnesses for HSST plate 03 (model tests 1 and 2), HSST plate 04 (model test 3), and for material (central locations) used to generate the curve in Fig. 8 (thermal shock data).

The data for plate 04 in the quenched-only condition [obtained with a 38-mm (1 1/2-in.) specimen] indicated that the cooling rate was indeed a major factor in the difference between the crack-arrest model material and the thermal shock material. The cooling rate studies described in the preceding chapter were then performed to verify and explain the unexpected behavior that was observed. From the point of view of the model tests, the high static fracture toughness values of quenched-only material was disappointing. The curves shown in Fig. 11 indicated that arrest was possible over a wide range of temperatures for a very large flaw [i.e., $K_I(a_f)/K_I(a_i) = 1.6$] and for a brittle starter section with a toughness considerably less than that which can be inferred from comparing

precracked Charpy-size specimens made from the actual model material with those made from the thermal shock material (Fig. 32).

Curves of $K_{ID(min)}$ and K_{Ia} for the tough material divided by K_{Ic} of the brittle material (based on precracked Charpy specimens made from quenched-only plates 03 and 04) are shown in Figs. 33 and 34. Also shown in these figures is the ratio of $K_I(a_f)$ to $K_I(a_i)$ for the actual model test configuration. The flaw for the configuration had been selected to give a near minimum ratio; therefore, no further advantage [i.e., lowering the $K_I(a_f)/K_I(a_i)$ horizontal line] could be obtained by changing the flaw configuration. This point was discussed in more detail in Chapter 3.

In the temperature range for which arrest data were available, it seemed apparent that crack arrest could not be obtained. The positive

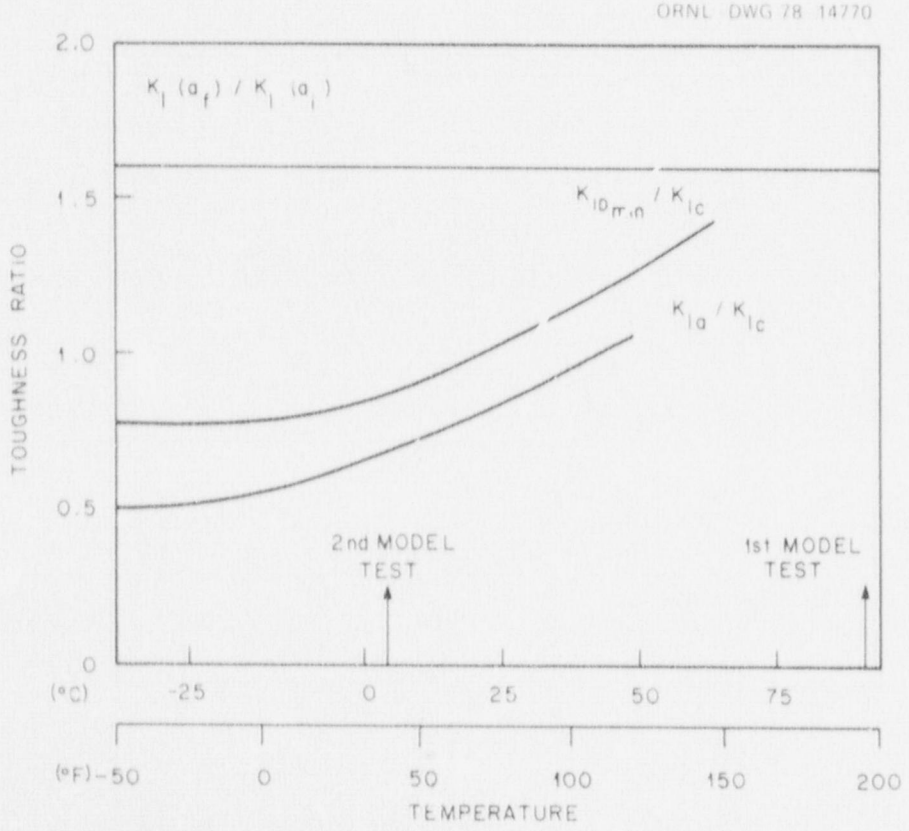

Fig. 33. Toughness (K) ratios based on conditions at arrest (a_f) to conditions at initiation (a_i) and based on the material properties $K_{ID(min)}$ and K_{Ia} for the quenched-and-tempered material; K_{Ic} for quenched-only plate 03 material.

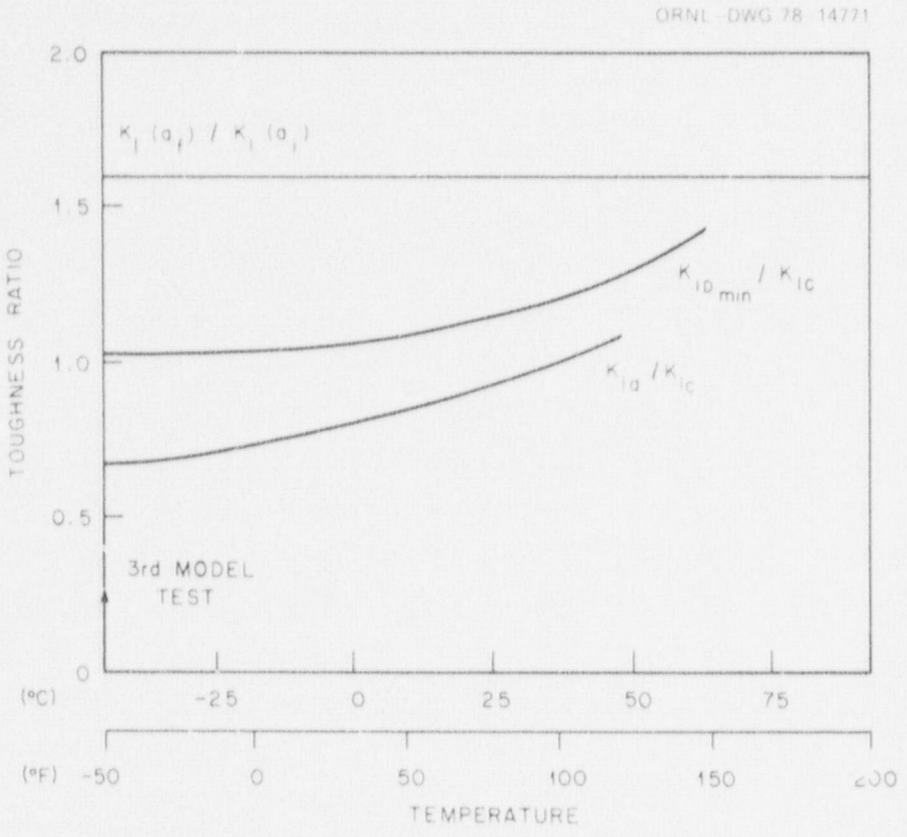

Fig. 34. Toughness (K) ratios based on conditions at arrest (a_f) to conditions at initiation (a_i) and based on the material properties $K_{ID(min)}$ and K_{Ia} for the quenched-and-tempered material; K_{Ic} for quenched-only plate 04 material.

slope in Fig. 33 did, however, suggest that the arrest criterion [Eq. (10)] could possibly be met by raising the test temperature to a nominal value such as 93°C (200°F).

Although the study of low upper-shelf material was not an objective of the model test program, it nevertheless seemed that such a secondary objective could be accommodated without detriment to the primary objective of studying crack arrest. The brittle material had an upper-shelf Charpy impact energy of 41 J (30 ft-lb), as shown in Fig. 21, at 93°C (200°F). Thus, since a high temperature was believed to be needed for a possible crack-arrest outcome, it was decided to test the first crack-arrest model at the temperature where the brittle starter material was on the Charpy impact energy upper shelf. The actual test temperature for the first

model test was 91°C (196°F). Details of the first crack-arrest model test are given in the next two chapters. Since the test temperature for the first model corresponded to the Charpy impact energy upper shelf, it was expected that some stable tearing and/or blunting would precede rapid propagation in the brittle starter material. It turned out, however, that the crack extended stably through the brittle section to the EB weld joining the brittle and tough sections.

Because fast fracture was not achieved during the first test, it was decided to lower the test temperature for the second model test to a value corresponding to the transition region of the Charpy impact energy data. At the lower temperature, crack arrest was not considered likely; however, it was thought worthwhile to conduct the test to demonstrate the conditions necessary for nonarrest. Immersing the model in a water-and-ice bath proved to be a convenient method to maintain a test temperature in the range that was considered appropriate for the second test. The actual temperature for the second test, as determined by five thermocouples attached to the model, was 4°C (39°F). At that test temperature, fast fracture in the brittle section was considered likely. It turned out, however, that while there were two short bursts of crack extension that could be characterized as fast fracture and arrest, the bulk of the crack extension through the brittle starter section during the second model test was slow stable crack extension. The difficulty in achieving fast fracture was a contributing reason for changing from quenched-only plate 03 to quenched-only plate 04 for the brittle starter section. Since two short bursts of fast fracture followed by arrest occurred during the second test, it seemed that a model made with the more brittle as-quenched 04 material (compared to as-quenched 03) and tested at an even lower temperature would likely fail by fast fracture through the brittle region. The test temperature selected for the third test was -22°C (-7°F). From Fig. 34, it can be seen that arrest was an unlikely outcome. This temperature was achieved by adding dry ice to an ethylene glycol-water bath. When the vessel was tested, a short slow stable crack extension was determined from break wires along the expected path of crack extension. The test was terminated after only a very short extension, and the model temperature was reduced even further for a subsequent test. The third crack-arrest model was then

tested at -47°C (-52°F). Details of that test and the first two model tests are given in the following two chapters.

7. INSTRUMENTATION AND EXPERIMENTAL PROCEDURE

The three crack-arrest models were tested at Oak Ridge National Laboratory in a specially designed concrete and steel enclosed pit that had been used for previous HSST Program pressure vessel model tests. The first model was tested at 91°C (196°F). The model was placed on an insulating blanket that rested on the floor of the pit and was enclosed in a metal frame containing four Calrod heaters. Insulating blankets covered the entire assembly. A thermocouple was suspended in the space between the metal frame and the insulating blankets and used for automatic control of the Calrod power supply. A period of ∿24 hr was required to bring the vessel and the pressurizing fluid (water) contained in the model up to test temperature. Five thermocouples attached to the outside surface of the vessel were the basis for establishing a stable test temperature. The thermocouples were connected to a Brown recorder which gave a strip-chart record of temperature. The second and third models were cooled by submersion in a mixture of 50% water and 50% ethylene glycol. Regular ice was then added to the mixture to bring the second model down to the required test temperature. Five thermocouples were attached to the second model and a sixth was suspended in the bath. The third model was cooled by placing dry ice in the water-ethylene glycol bath. One of the six thermocouples used in the third test was located in the pressurizing fluid (water-ethylene glycol mixture) inside the model.

The test pressure was indicated by two pressure transducers connected to the pressure line leading into the models. The distance between the model and pressure transducers was approximately 254 mm (10 in.). For the first two tests, BLH type DHF high-frequency transducers with a capacity of 207 MPa (30 ksi) were used. Because of a conflicting test requirement, Viatran pressure transducers with a capacity of 220 MPa (32 ksi) were used for the third test. An additional difference for the third test was that one of the pressure transducers was connected to the end of the model opposite the end where the pressure inlet line was attached. At the pumping station, which (along with the recording equipment) was located ∿8 m (∿25 ft) from the test bunker, there was a

dial pressure gage attached to the pumping equipment. The pump (American Instrument Company single-ended model 46-13720 plunger type) was an air-driven, positive-displacement, differential piston pump with a 138-MPa (20-ksi) output pressure capacity.

Three or four — depending on the test — foil-type strain gages (Micromeasurements type EA-06-250BG-120) were attached to the models at locations remote from the flaw. Two crack-extension ladders were also attached to the vessel at the sharpened end of the flaw and in the expected path of crack propagation. The crack-extension indicators consisted of individual long slender foil gages (Micromeasurements TK-06-19CDK-350) connected in parallel and to a voltage-dividing circuit. Figure 35, which is a photograph of the first crack-arrest model, shows the arrangement of the 11 crack-extension gages, eight of which were connected in parallel to form one of the ladders. The three remaining gages (i.e., the third, seventh, and ninth from the crack tip) formed an independent ladder that was both recorded by and used to trigger the high-speed recording equipment. The third gage from the crack tip was used to trigger the equipment in order to avoid a premature trigger that might have been caused by either yielding or initial slow crack growth. Figure 36 is a close-up photograph of the crack-extension ladder. J. Dally and T. Kobayashi of the University of Maryland used a high-speed Kranz-Schardin camera to photograph cracks running in three Homalite 100 plates, which had the foil-gage ladders described above attached to them. Crack velocities on the order of 380 m/sec (15,000 in./sec) determined from the camera framing rates agreed with velocities determined from oscilloscope traces of the ladder and electronic circuit output. The ladders that showed good correlations were constructed with gages having epoxy-glass backings. Other gages with polyimide backings were also tested by Dally and Kobayashi, and the velocities determined from the electrical signals for those cases were much lower than what was indicated by photography.

The recording equipment used for the model tests is listed in Table 5. Except for the thermocouples, whose outputs were recorded on the Brown recorder, the output of each transducer was recorded on an instrument that covered periods on the order of milliseconds, seconds,

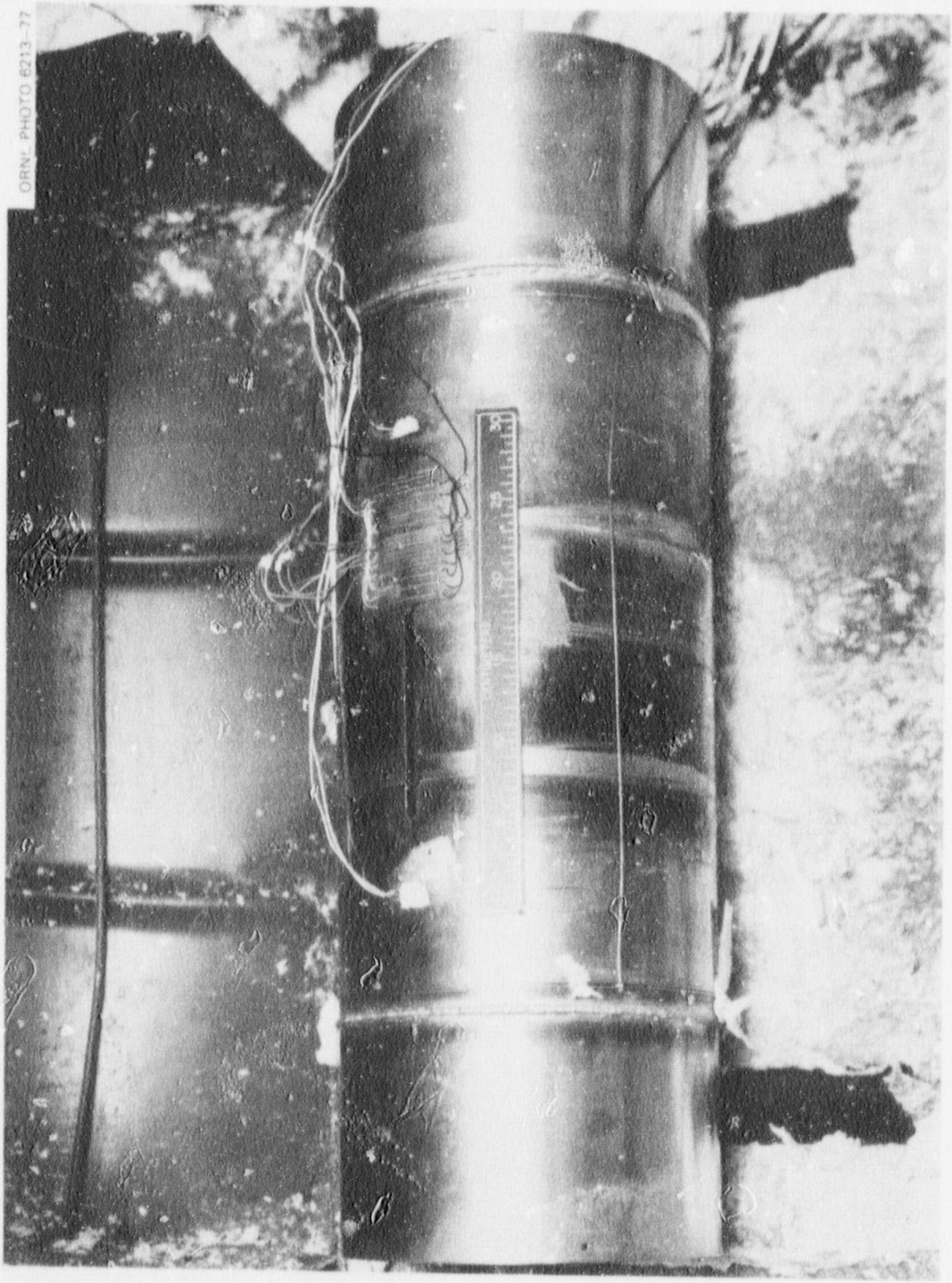

Fig. 35. First crack-arrest model with instrumentation (1 cm = 0.394 in.).

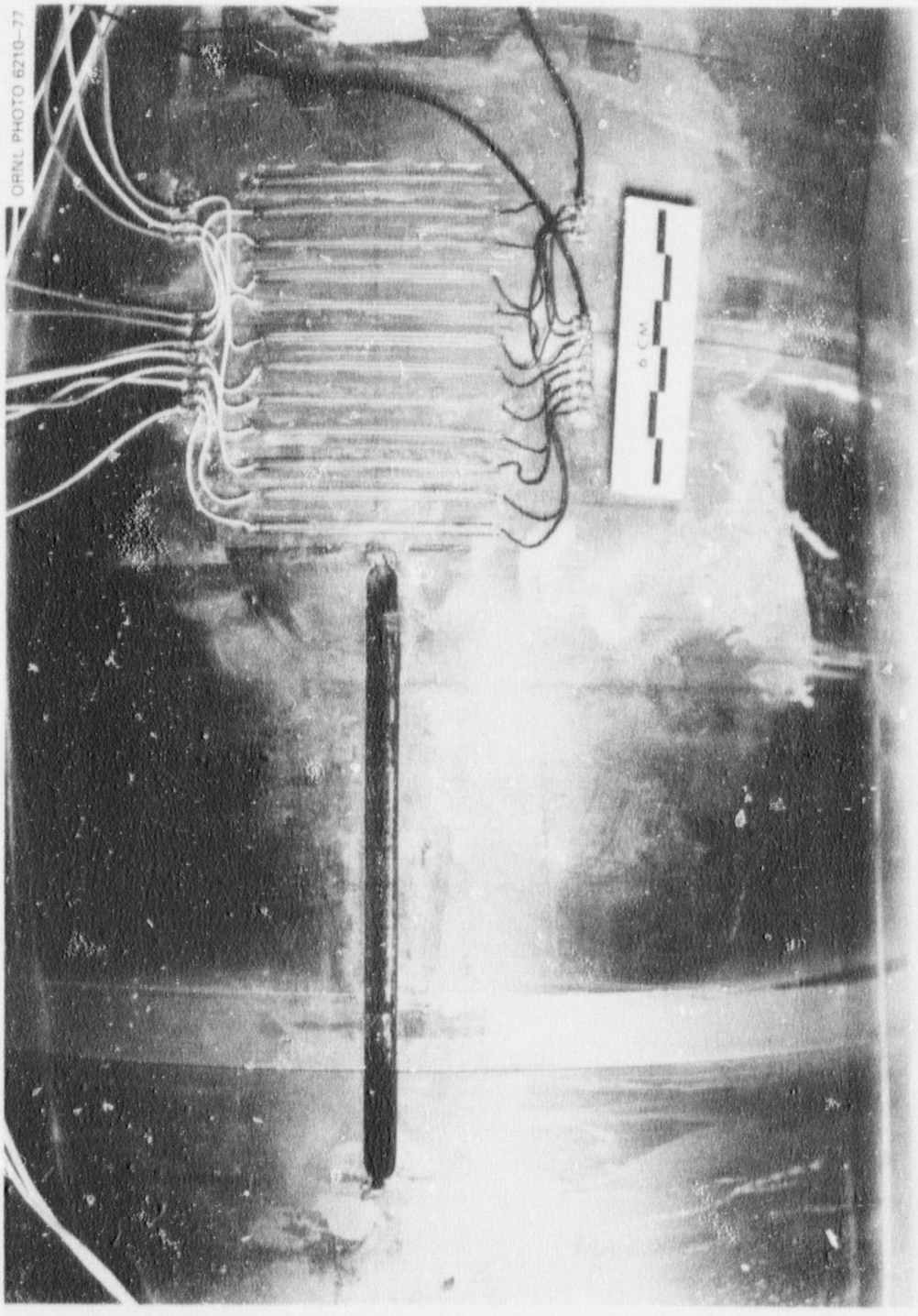

Fig. 36. Close-up view of ladder gage used to monitor crack extension in models (1 cm = 0.394 in.).

Table 5. Instrumentation used in crack-arrest model tests

Equipment	Number of units	Total channels
Biomation 1015	1	4
Biomation 805	2	2
Biomation 8100	1	2
Tektronic storage scopes	2	5
Hewlett-Packard strip charts	3	6
Brown temperature recorder	1	6

and hours (i.e., Hewlett-Packard strip charts). For example, the Biomation 805 can take 2024 samples of information at 0.5 μsec per sample to give a recording period of 1.012 msec. Because of the short periods of recording for some of the devices, it was necessary to trigger them, as mentioned previously, by means of the ladder gages.

In addition to the automatic recording described above, manual record keeping was also employed: the clock time, temperature of one thermocouple, and model pressure indicated by the dial gage were recorded manually, and additional comments related to the test, such as periods of pumping, were included when appropriate.

A typical model test would involve bringing the vessel to the nominal test temperature and allowing it to stabilize for some period of time. In general, the heating or cooling of the model would begin the day before the actual test. The next step would be pressurization of the vessel up to some nominal low pressure and cross-checking of recording equipment and transducer outputs. After it was determined that all equipment was functioning properly, pumping would continue until the model either began to leak or burst. A limit of 104 MPa (15 ksi) was established as the maximum level to which the models would be pressurized.

8. TEST RESULTS

The three crack-arrest models were tested in their numbered order Mar. 3, 1977, Mar. 31, 1977, and May 26, 1977. The three models were identically configured (Fig. 5) and had identically configured flaws (Fig. 6). The center sections (i.e., the brittle starter sections) of the first and second models were made from quenched-only material from HSST plate 03, while the center section for the third model was made from quenched-only material from HSST plate 04. The only significant difference in the model tests was the temperature at which each model was tested: model 1 was tested at 91°C (196°F) and model 2 was tested at 4°C (39°F). Crack-arrest model 3 was tested [after an aborted test at -22°C (-7°F)] at -47°C (-52°F). The rationale for the selection of the three test temperatures is discussed in Chapter 6.

8.1 Crack-Arrest Model 1

Pressure and crack extension (indications from the eight-gage ladder) are shown in Fig. 37 as functions of time for the first model test. Also shown in the figure, as an intermittent horizontal line, are the periods when the pump was actually being used to pressurize the vessel. The first indication of crack extension was recorded ∿10 min into the test when the pressure was 93 MPa (13,400 psi). The pressure was increased uniformly over the next 80 sec to 102 MPa (14,750 psi). Slow, stable crack growth accompanied the increase in pressure. Figure 38 shows the period of initial crack extension on an expanded time scale. Pumping was discontinued at the point shown for ∿18 min. Pressure and crack length remained nearly constant over this period. When pumping was resumed, further crack extension was detected at 107 MPa (15,500 psi). At that point, the stainless steel liner began to leak, and an increase in pressure above 108 MPa (15,600 psi) was not possible.

Figure 39 is a photograph of the first crack-arrest model. The photograph was taken after the test and shows crack extension on the outside surface. Following the test, the model was cut into sections

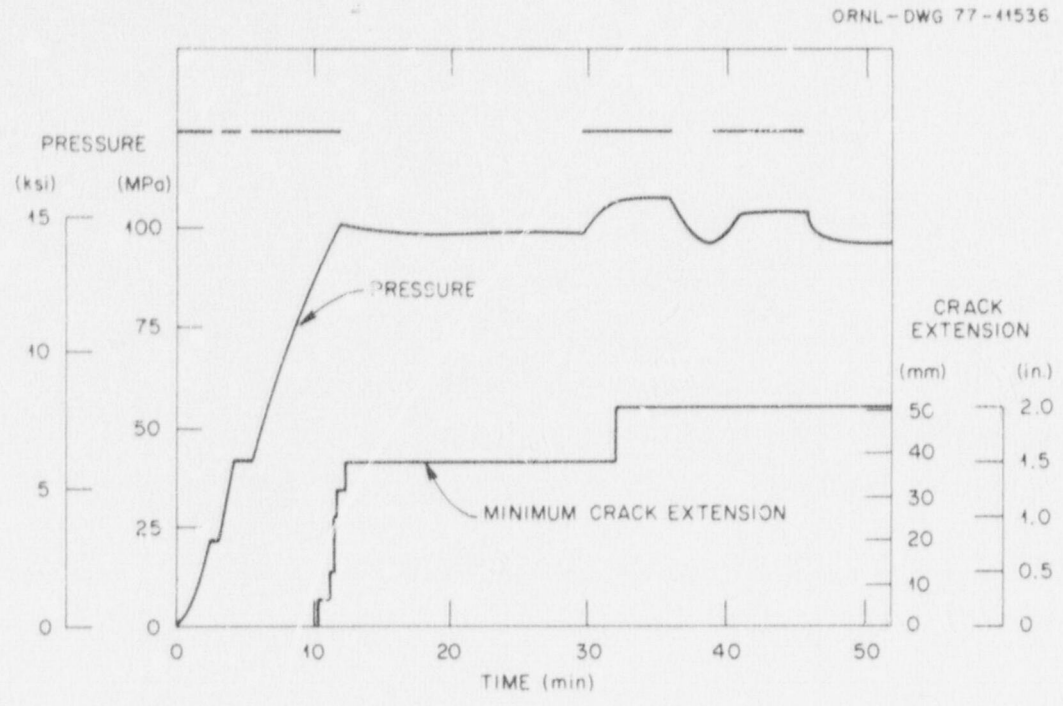

Fig. 37. Pressure and minimum indicated crack extension vs time for the first model test at 91°C (196°F). The horizontal intermittent line indicates periods when pumping occurred.

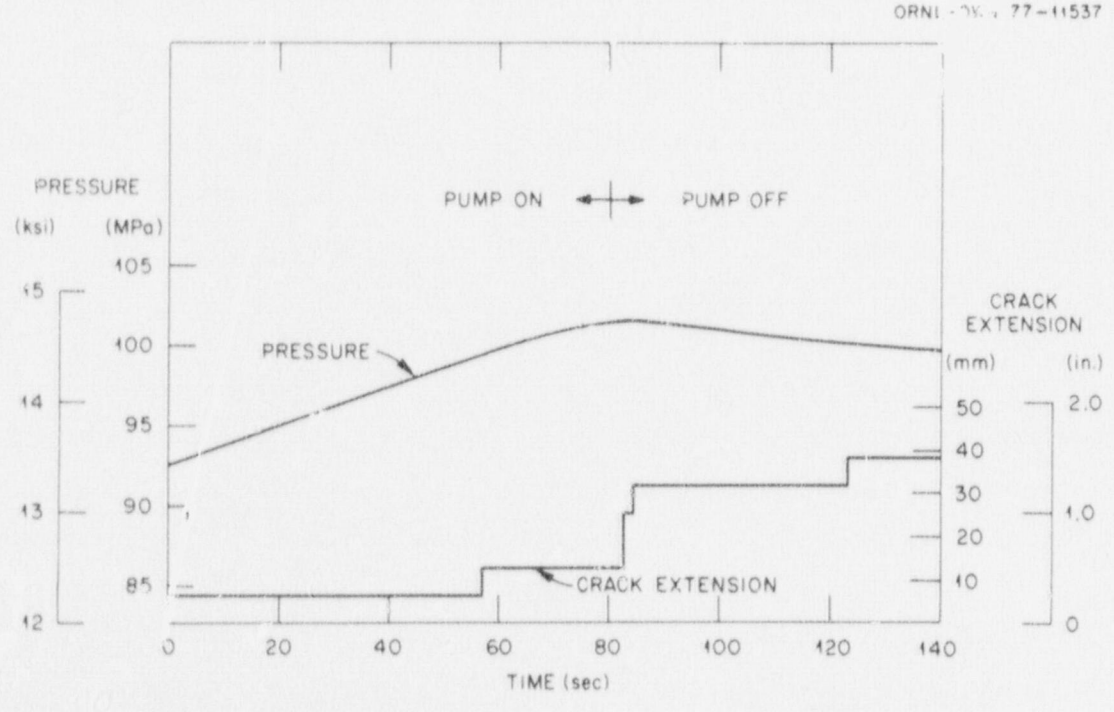

Fig. 38. Expanded pressure and crack extension history from the first crack-arrest model test.

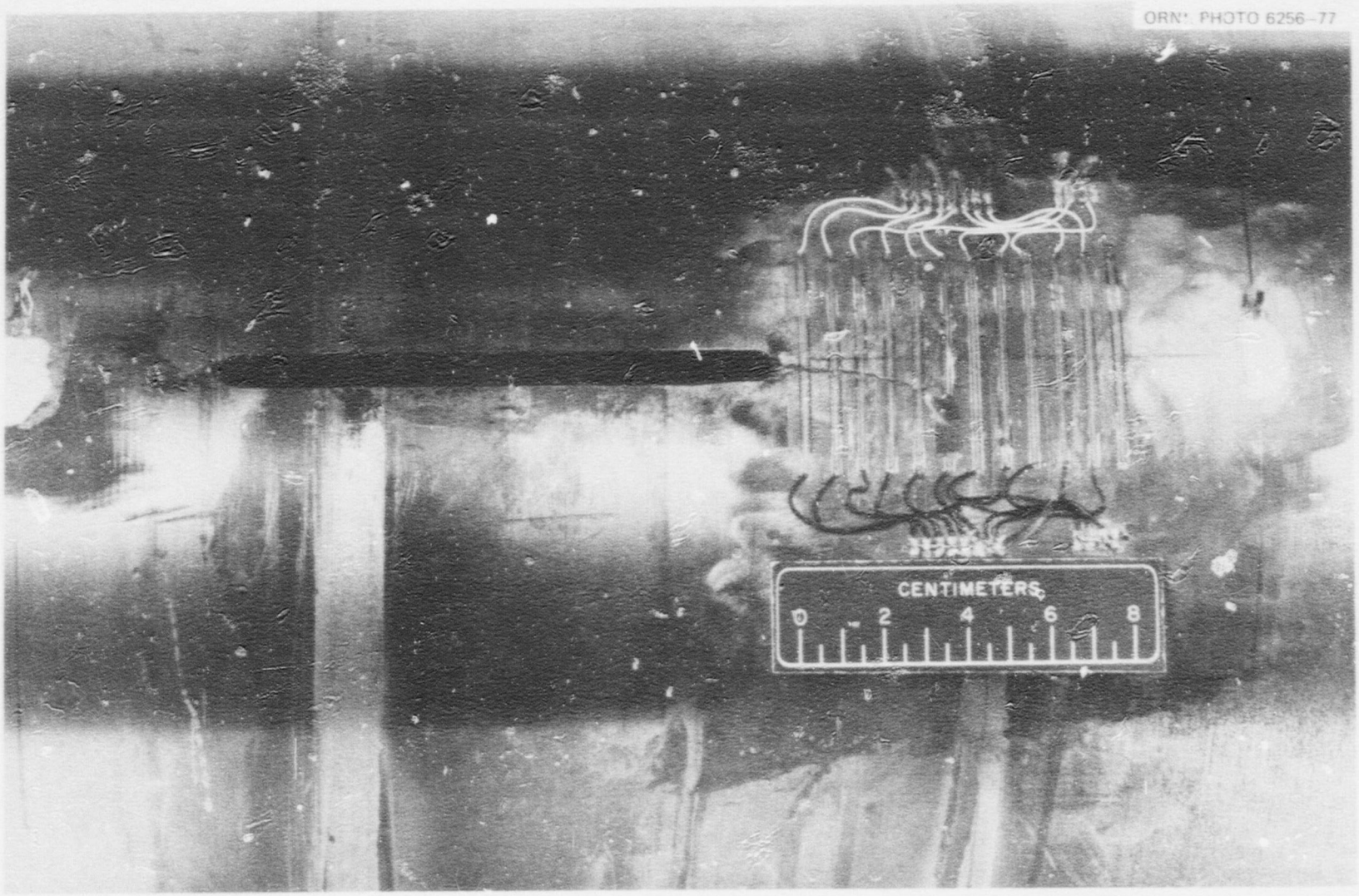

Fig. 39. View of ladder gage after the first model test (1 cm = 0.394 in.).

in order to permit inspection and scanning electron microscopy (SEM) of the fracture surfaces. Figure 40 is a photograph showing a section containing part of the machined flaw and the region of slow, stable crack extension. The darkened area (caused by heat tinting and penetration of dye) is the surface created by the crack extension during pressurization. The light-colored surface at the left of the specimen is the fracture surface created when the piece was broken open after it had been soaked in liquid nitrogen. A shear lip on the upper surface progressively developed with crack extension after ∿25 mm (∿1.0 in.) of flat fracture. A flat portion of crack extension also extended through the EB weld joining the brittle and tough materials. There is an indentation of about 2 mm (0.08 in.) along the path of crack extension on what had been the interior surface of the model which apparently resulted from yielding. Figure 41 shows the three regions (i.e., sections *a*, *b*, and *c*) from which typical scanning electron micrographs were made.[21] The micrographs indicated that a ductile (dimple) mode of failure had occurred. Figure 42 shows such a micrograph of a region in the section labeled *b* in Fig. 41.

8.2 Crack-Arrest Model 2

Figure 43 shows the crack extension, pressure, and pumping periods for the second model test. The long hold period that occurred 10 min into the test was necessitated by difficulties with a strip-chart recorder and is not indicative of any peculiar model behavior. As in the first test, increasing pressure was needed to extend the crack after it had started to propagate. The first indication of crack extension occurred at 76 MPa (11 ksi). Pressurization was continued up to 103 MPa (15 ksi) and held constant at that level for 5 min. The test was then terminated. At each of the two times indicated by the asterisks in Fig. 43, a very loud "ping" was heard. Figure 44 is a photograph of oscilloscope traces made during the first "ping." The horizontal scale is 20 μsec per major division. The top and bottom traces are the outputs of a pressure transducer and an axial strain gage located 180° from the flaw, respectively. The center trace is the output of the eight-gage ladder. The oscilloscope

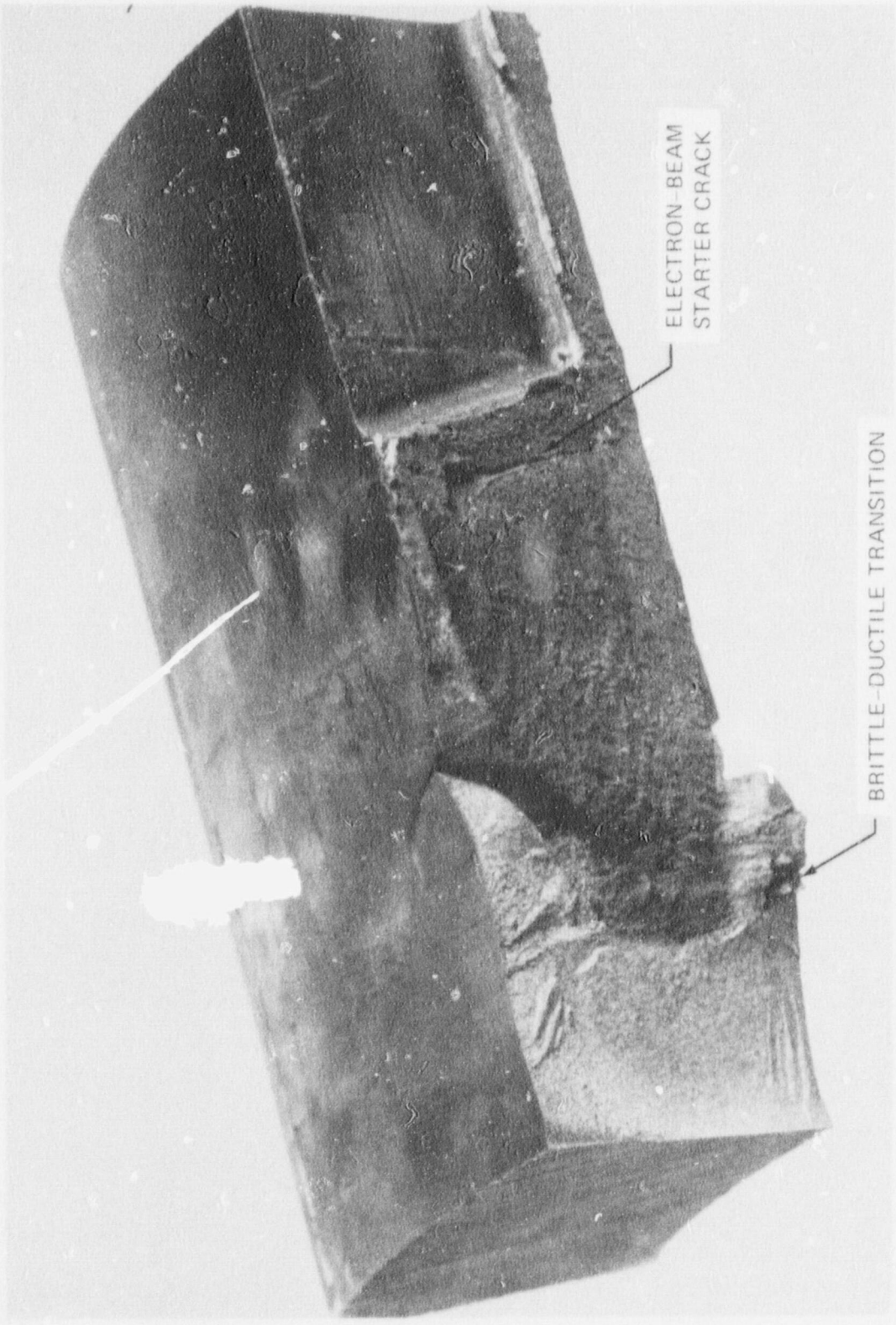

Fig. 40. Fracture surface from the first model test.

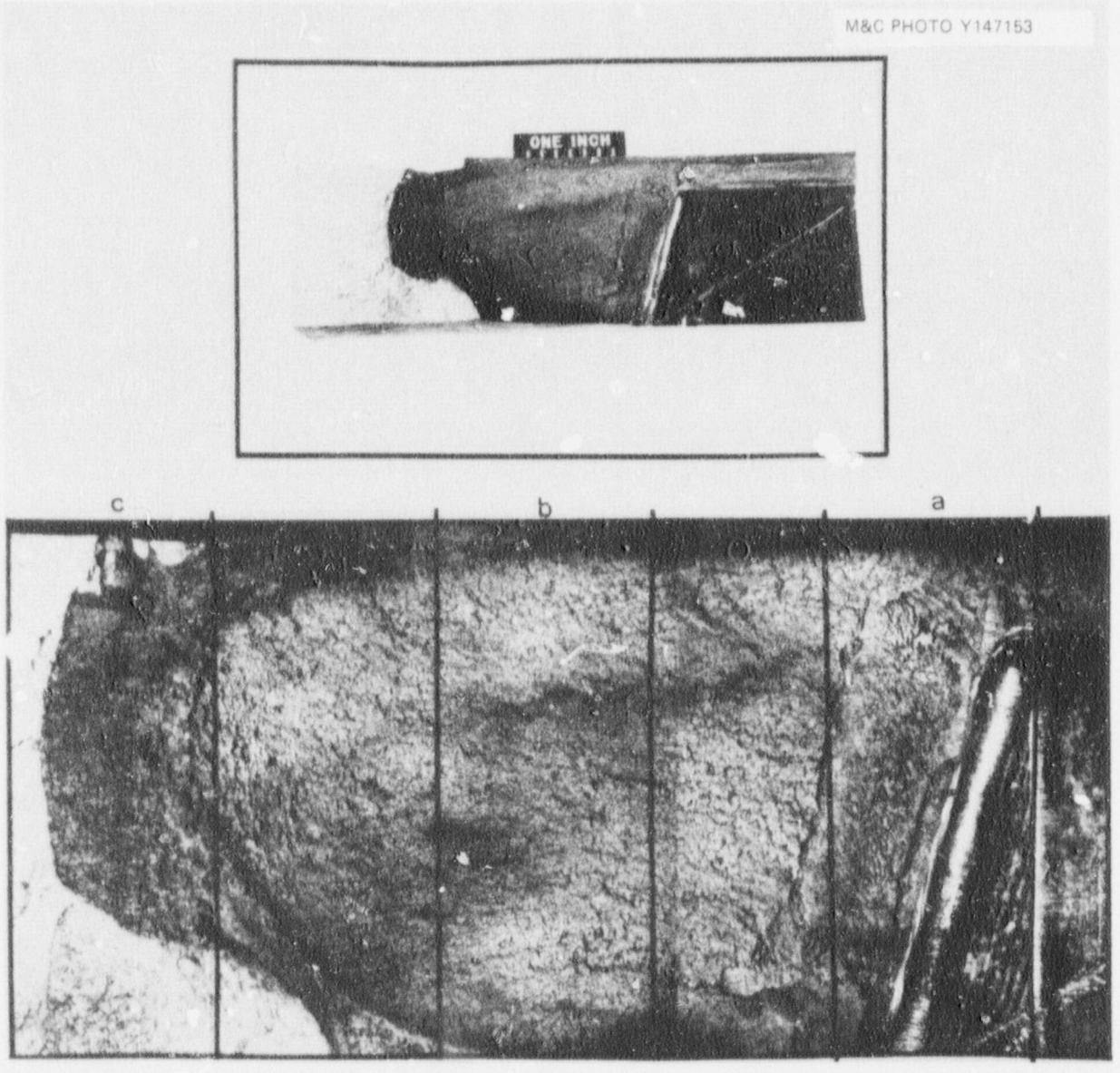

Fig. 41. Sectioning procedure for preparing samples for scanning electron microscopy in the first crack-arrest model test (1 in. = 25.4 mm).

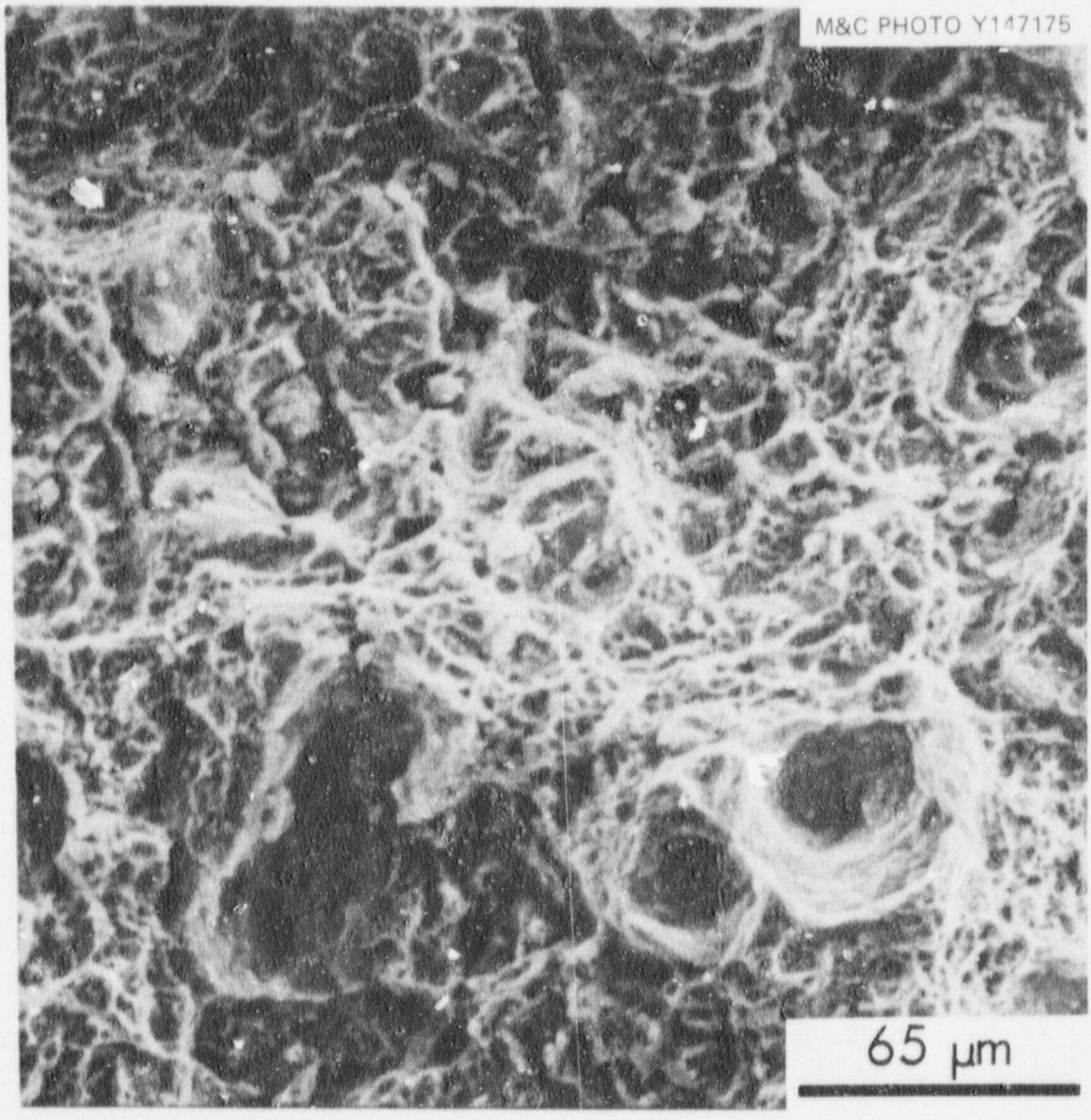

Fig. 42. Scanning electron micrograph of the propagation region identified as b in Fig. 41. The region exhibits a dimpled (ductile) appearance.

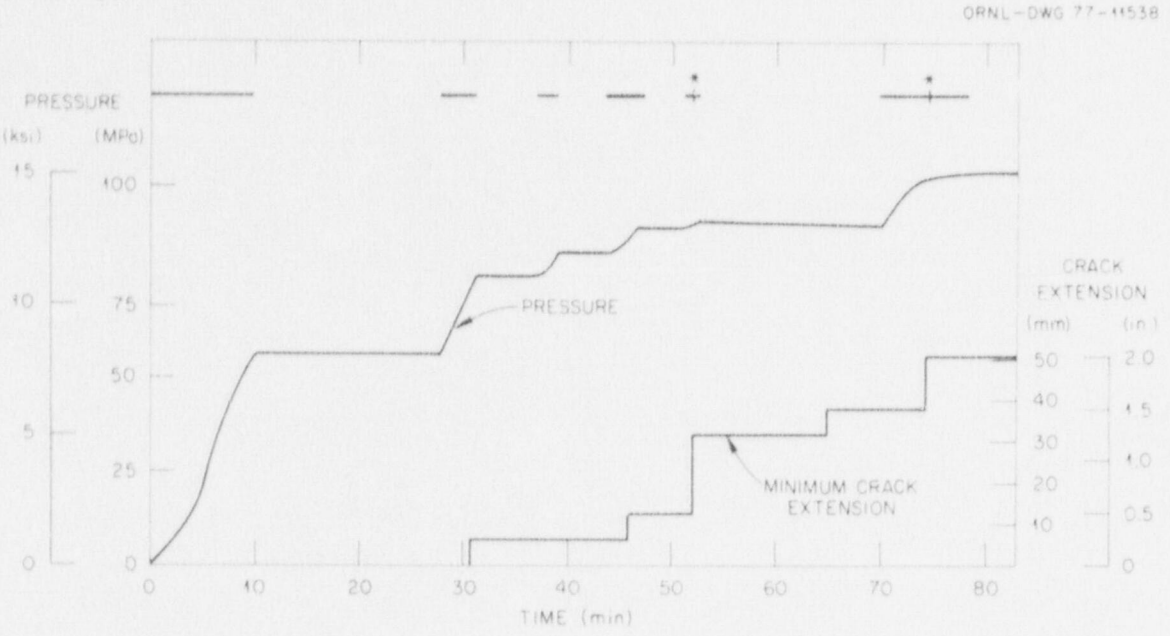

Fig. 43. Pressure and minimum indicated crack extension vs time for the second model test at 4°C (39°F). The intermittent horizontal line indicates periods when pumping occurred; the asterisks indicate the times when loud "pings" were heard.

was triggered by the breaking of the third leg of the eight-gage ladder. The step change in ladder output that occurred ∿100 μsec after the breaking of the third leg is the change in output due to the breaking of the fourth leg. The fifth leg broke approximately 5 min later (see Fig. 43). From the oscilloscope traces, the average crack velocity associated with the "ping" can be estimated to be ∿64 m/sec (2500 in./sec). This relatively low velocity is possibly a result of tunneling, which would mean that the time to break the adjacent legs of the ladder characterizes the time for the shear lip on the model outside surface to fail rather than an actual crack tip velocity. Comparable data were not obtained for the second "ping," which apparently accompanied fast fracture across the heat-affected zone of the EB weld and subsequent arrest in plate 57.

Figure 45 is a photograph of a piece cut from the second crack-arrest model and shows the fracture surface caused by the crack growth (darkened region) during pressurization. The shear lip formation is very pronounced. The crack progressed partially through the EB weld joining the brittle and tough sections of the model. The EB starter

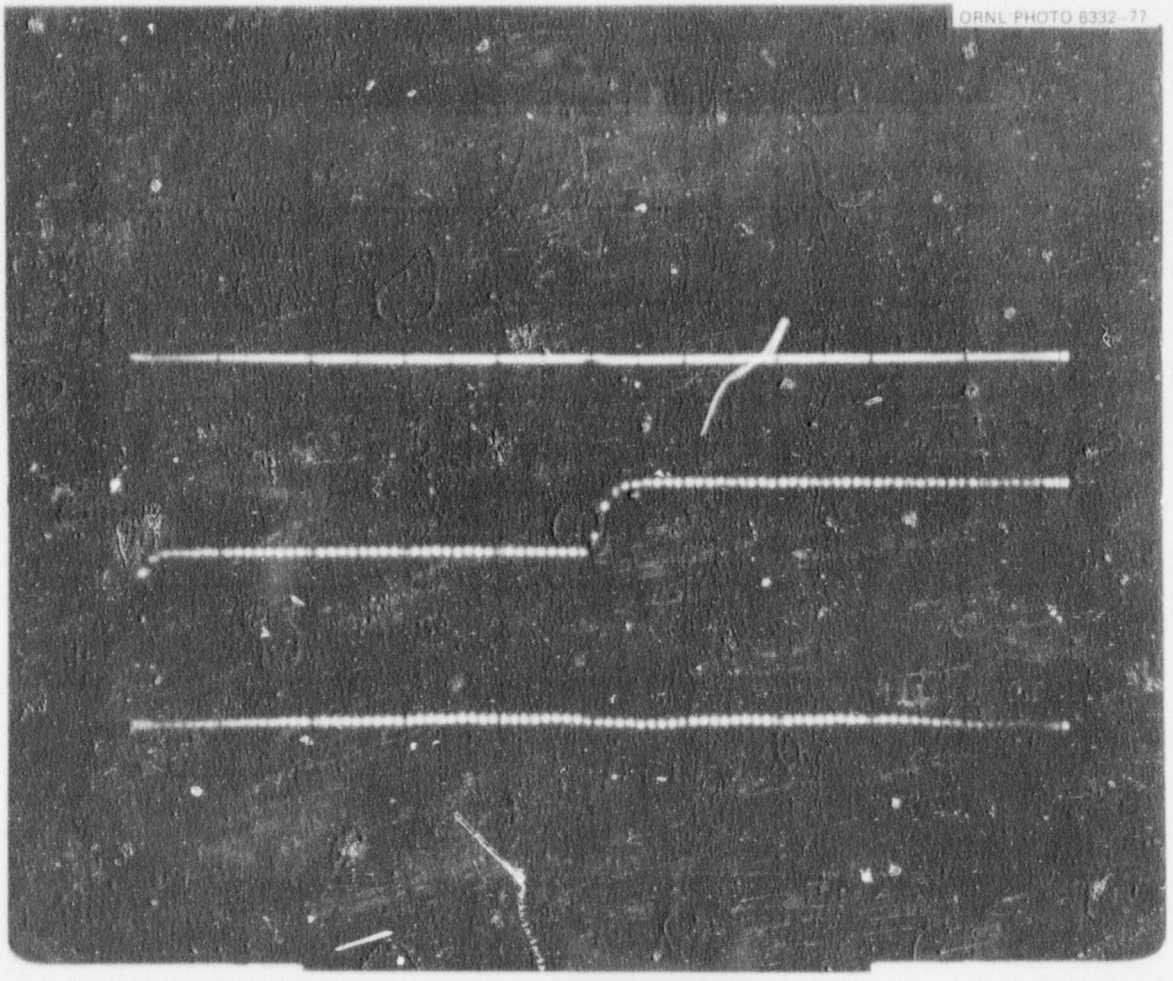

Fig. 44. Photograph of oscilloscope traces made at the time of the first audible crack extension during the second model test. The horizontal scale is 20 μsec per major division. From top to bottom, the traces are the outputs from a pressure transducer, the eight-gage ladder, and an axial strain gage 180° from the center of the flaw.

crack around the periphery of the machined slot is readily apparent. The development of the large shear lip after considerable extension is possibly the result of progressively lower yield strength caused by tempering of the brittle material close to the EB weld. The first crack-arrest model had a very similar appearance close to the weld. One of the objectives of the tests was to assess the effect of any tempering resulting from joining. It would seem from these results that there is possible tempering, which could contribute to the arrest (associated with the first "ping") prior to the crack entering the quenched and tempered material.

ORNL PHOTO 6582-77R

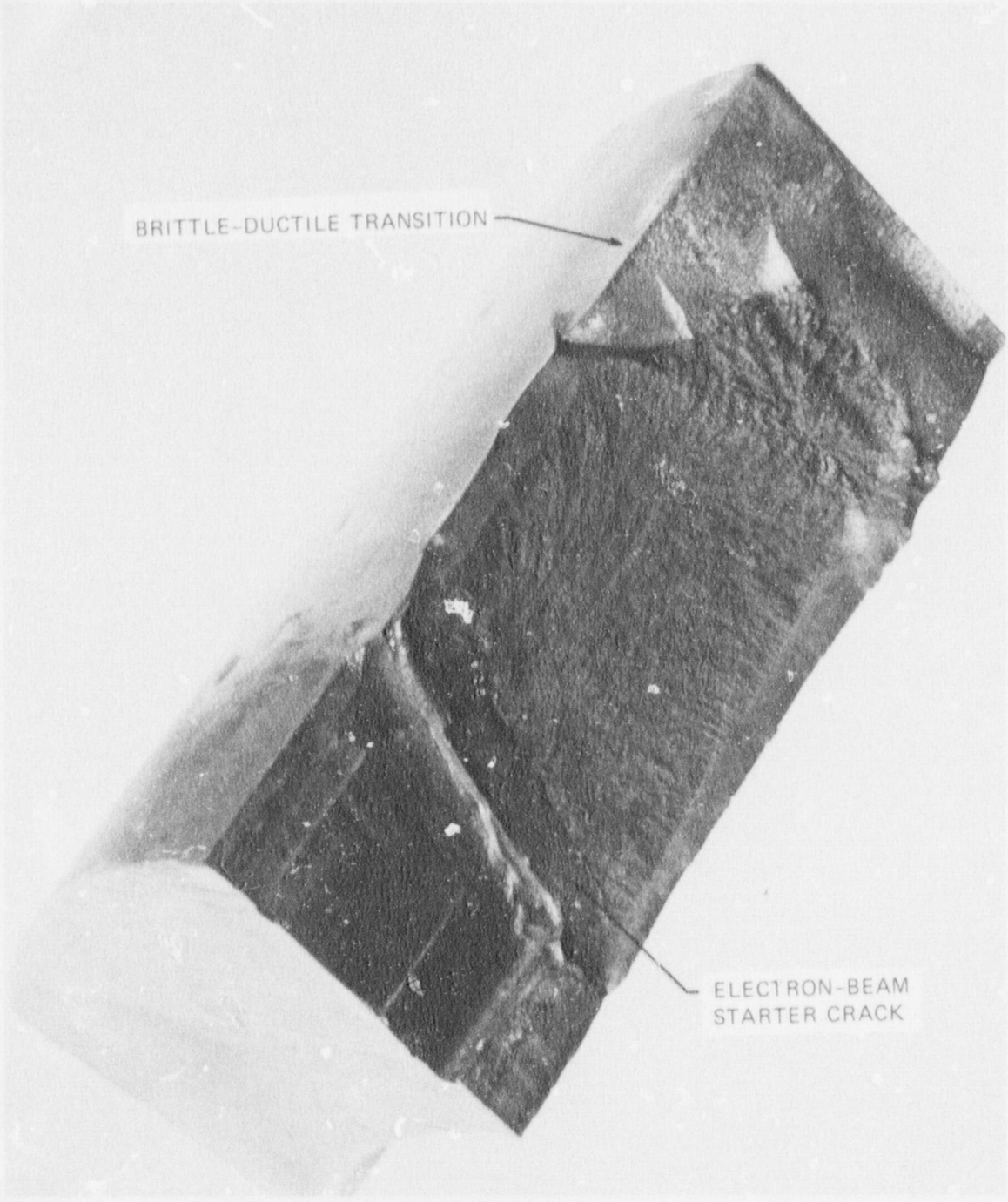

Fig. 45. Fracture surface from the second model test.

Figure 46 shows the sections (indicated by *a*, *b*, and *c*) which were used in making scanning electron micrographs of the fracture surface. The region identified as *a* in Fig. 46 exhibits a dimple mode of fracture, as indicated by the micrograph of this region shown in Fig. 47. The region identified as *b* also exhibits a predominantly dimple mode of fracture. In the region between sections *b* and *c* of Fig. 46, there are indications of both cleavage and dimple modes of fracture. It would seem that after considerable slow, stable crack extension, a pop-in occurred,

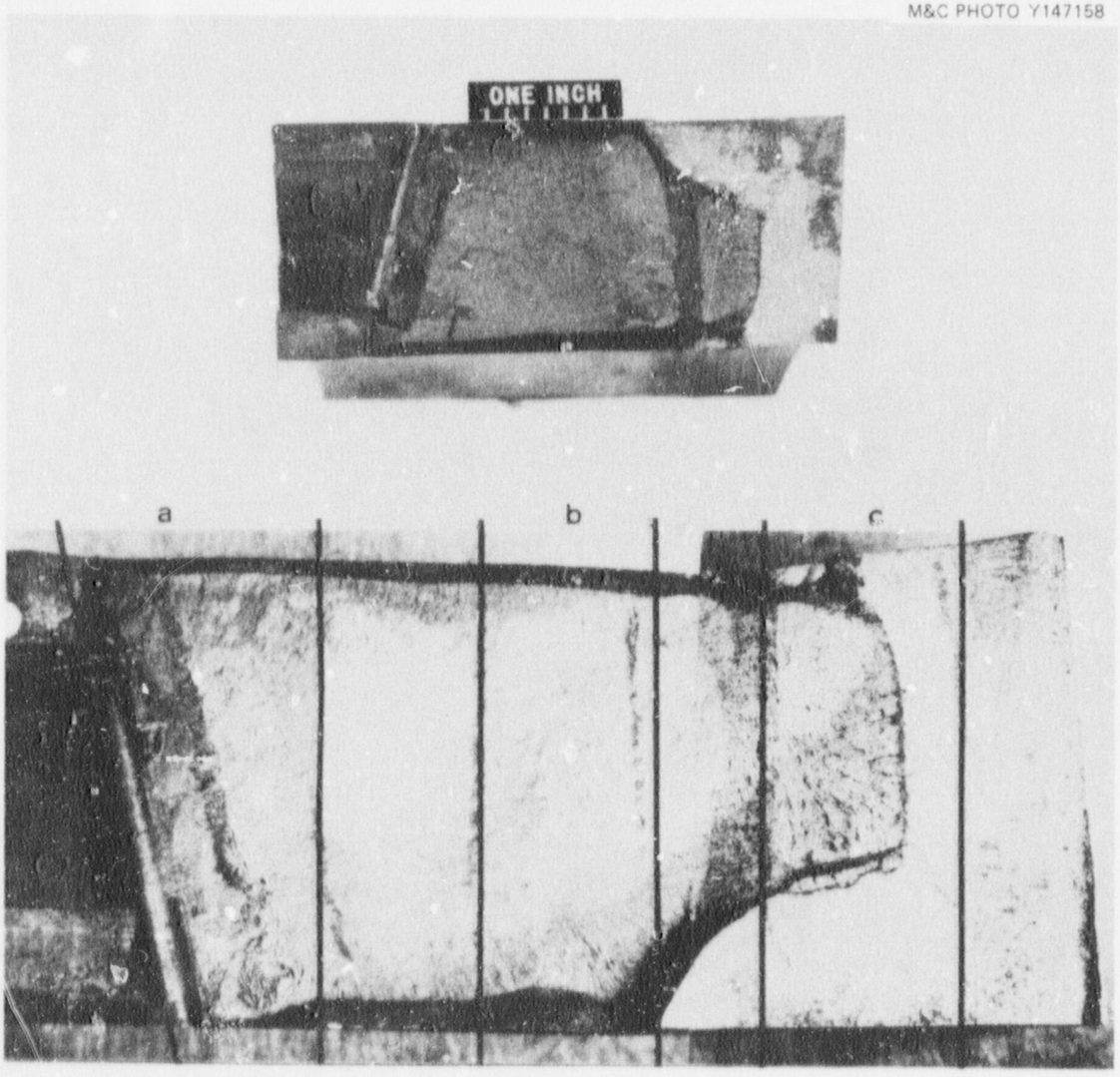

Fig. 46. Sectioning procedure for preparing samples for scanning electron microscopy in the second crack-arrest model test (1 in. = 25.4 mm).

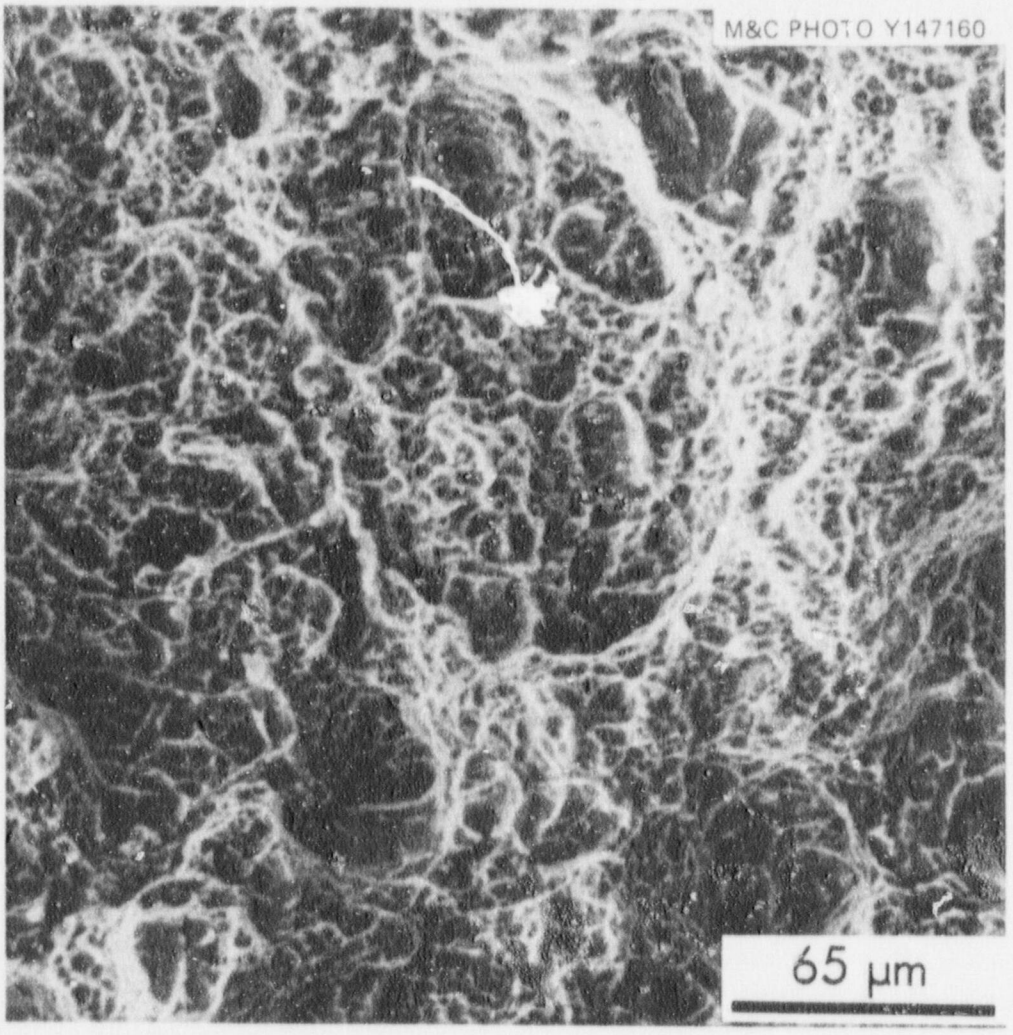

Fig. 47. Scanning electron micrograph of the propagation region identified as a in Fig. 46. The region exhibits a dimpled (ductile) appearance.

which gave the loud "ping" reported earlier and the indication of a short crack extension (Fig. 44) at a fairly low velocity. The crack apparently was arrested when it encountered the zone in the brittle material that was tempered by the EB weld joining the brittle to the tough materials. The dark gray band just to the left of section *c* (Fig. 46) that extends through the thickness of the wall has a sponge-like appearance and shows a dimple mode of fracture in the scanning electron micrographs. The dark region in section *c* exhibits a predominantly cleavage mode of fracture, which is probably associated with the second loud "ping" heard during the

test. A very narrow band at the terminus of crack extension has a dimpled appearance. The very light-colored material in section c is a fracture surface that resulted from breaking open the sample piece after it had been soaked in liquid nitrogen. These cleavage and ductile fracture surfaces are shown in Figs. 48 and 49.

8.3 Crack-Arrest Model 3

The third crack-arrest model was initially tested on May 26, 1977, at -22°C (-7°F). Stable crack extension of more than 3.5 mm (0.14 in.) but less than 9.8 mm (0.39 in.) was indicated at 91 MPa (13,200 psi) by the ladder gages. Pressurization was continued up to 103 MPa (15,000 psi), as had been done in the first two model tests. However, unlike the first two model tests, further crack extension did not occur.

Because unstable crack extension did not appear likely at the -22°C (-7°F) test temperature without resorting to a very high pressure and because the third model was intact and had experienced only slight crack extension, it was decided that fast fracture should be achieved by a subsequent retesting of the third model at a lower temperature. Crack arrest was considered unlikely at the lower test temperature in that the initiation toughness of the brittle material was close to the arrest toughnesses, as discussed in Chapter 3.

The third crack-arrest model was retested on June 2, 1977, at -47°C (-52°F), and unstable crack extension occurred at 102 MPa (14,800 psi). Figure 50 is a photograph of the failed vessel after the ladder gages had been removed. Axial cracks propagated from each end of the machined slot. The axial crack that propagated to the right of the slot emanated from the original EB-sharpened crack front which had experienced a slight extension during the initial test of the model at the higher temperature.

Although it is not readily apparent from the photograph, there were four EB circumferential welds in the model. The two welds joining the brittle center section to the tougher sections were ground flush so that the weld bead would not interfere with crack extension. The two EB weld beads that are readily apparent in Fig. 50 are between the tough sections and the flat-head caps.

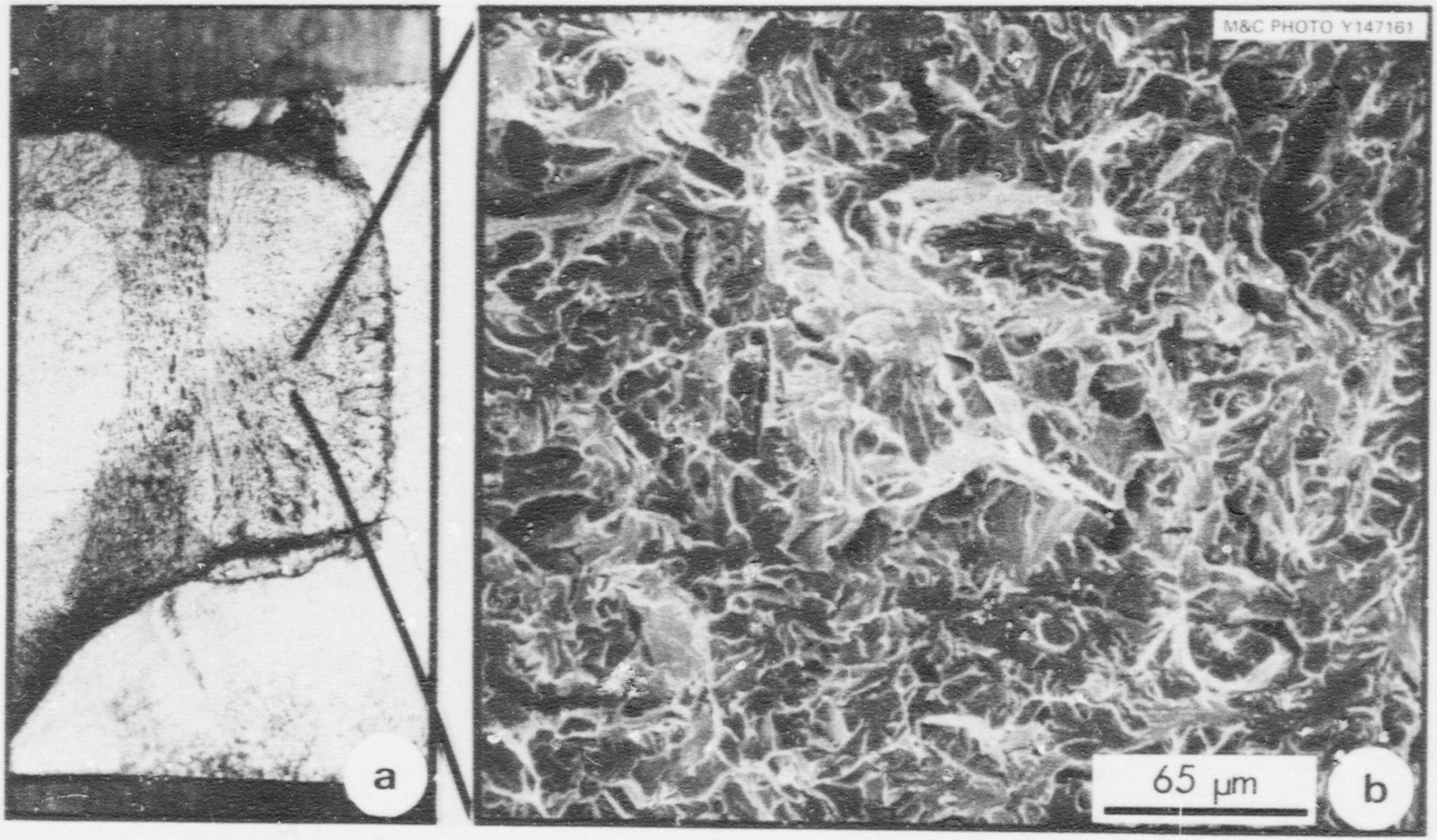

Fig. 48. Scanning electron micrograph of the fracture in the electron-beam (EB) weld near the crack terminus. The fracture mode in the EB weld was cleavage. (a) Photomacrograph of the fracture surface (i.e., section c of Fig. 46); (b) Scanning electron micrograph of typical cleavage fracture in the EB weld. (Original reduced 14%)

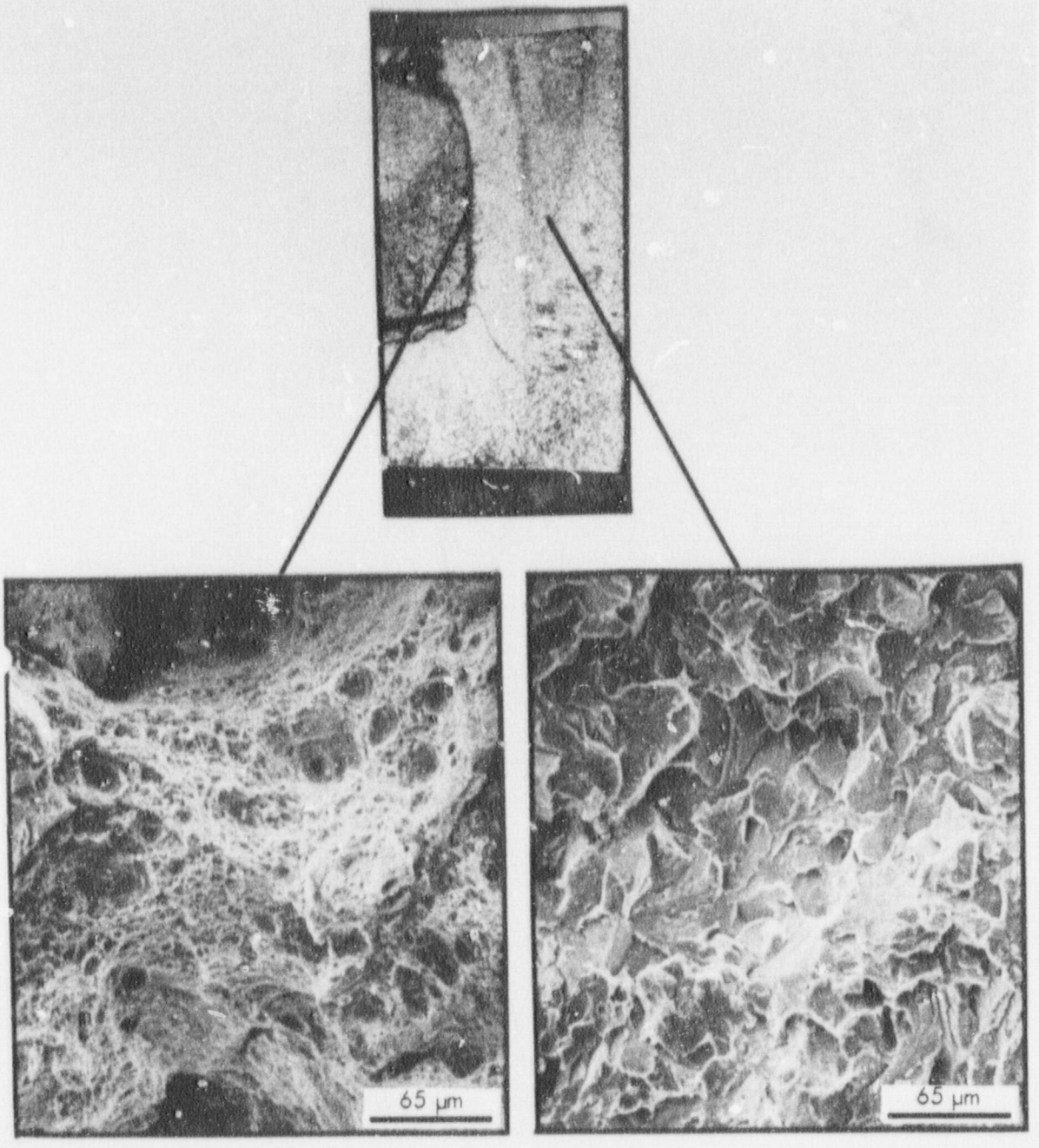

Fig. 49. Scanning electron micrographs of the narrow terminus region in the section identified as *e* in Fig. 46. The terminus (crack tip in tough material) exhibits a dimple mode of fracture. The cleavage region on the right is the fracture surface that resulted from soaking the piece in liquid nitrogen and then breaking it open. (Original reduced 18.5%)

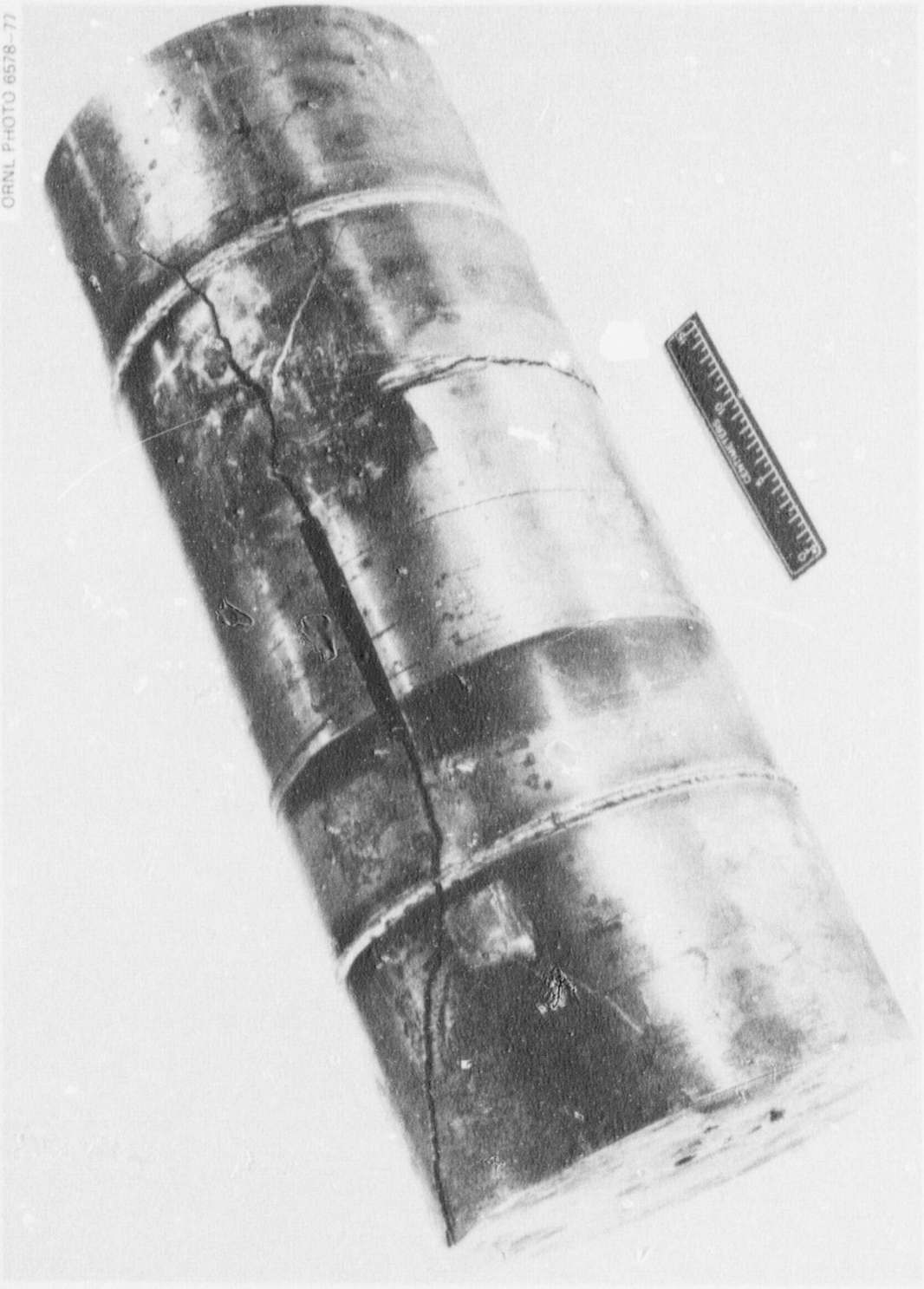

Fig. 50. Third crack-arrest model after test at -47°C (-52°F) (1 cm = 0.394 in.).

Figure 51 is a close-up photograph of the third crack-arrest model and shows segments of two circumferentially oriented cracks that propagated ~180° about the model. The crack emanating from the end of the slot is the crack that was of principal interest from the standpoint of studying crack arrest. The tip of the small arrow in Fig. 51 locates the center of the EB weld joining the brittle and tough cylindrical sections. The third model was sawed in half to provide a fracture surface for SEM. A part of the model is shown in Fig. 52. When the model was sectioned, a void, 91 by 19 mm (3.6 by 0.75 in.), was found in the EB weld that joined the brittle center cylinder to a tougher cylinder. The void was 71 mm (2.8 in.) from the line of initial crack extension; thus, because of the distance of the void from the point of crack initiation, the void probably did not affect the initial crack extension but could have been a contributing factor to crack extension through the weld. The other circumferential crack initiated at a point along the machined slot. There was no obvious flaw or stress concentrator that would contribute to the initiation of that flaw. However, multiple cracks are not an unknown phenomena and are usually attributed to stress waves.[22]

Figure 53 shows oscilloscope traces of outputs from a pressure transducer and the eight-gage ladder that was used to indicate crack extension for the third model test. Each major time division in Fig. 53 is 20 μsec. Figure 54 shows plots of crack extension as indicated by the ladder gages and the response of two circumferential strain gages located along an axial line bisecting the machined slot (shown schematically) as a function of time measured from the first indication of unstable crack extension. The plot of crack length vs time shows that the crack had an average velocity of 410 m/sec (16,140 in./sec). The reduction in strain during crack extension would seem to be due to a drop in pressure. However, since the pressure transducers used in the third model test had integral signal amplifiers which had slow response times (a millisecond or slightly less), the drop in pressure as indicated by those transducers can be considered only as an upper bound. The steep rise in strain after the initial reduction is probably due to the influence of the crack tips as they approached each gage. After the tests, it was noted that the cracks propagated through the gages. If it is assumed that the left running

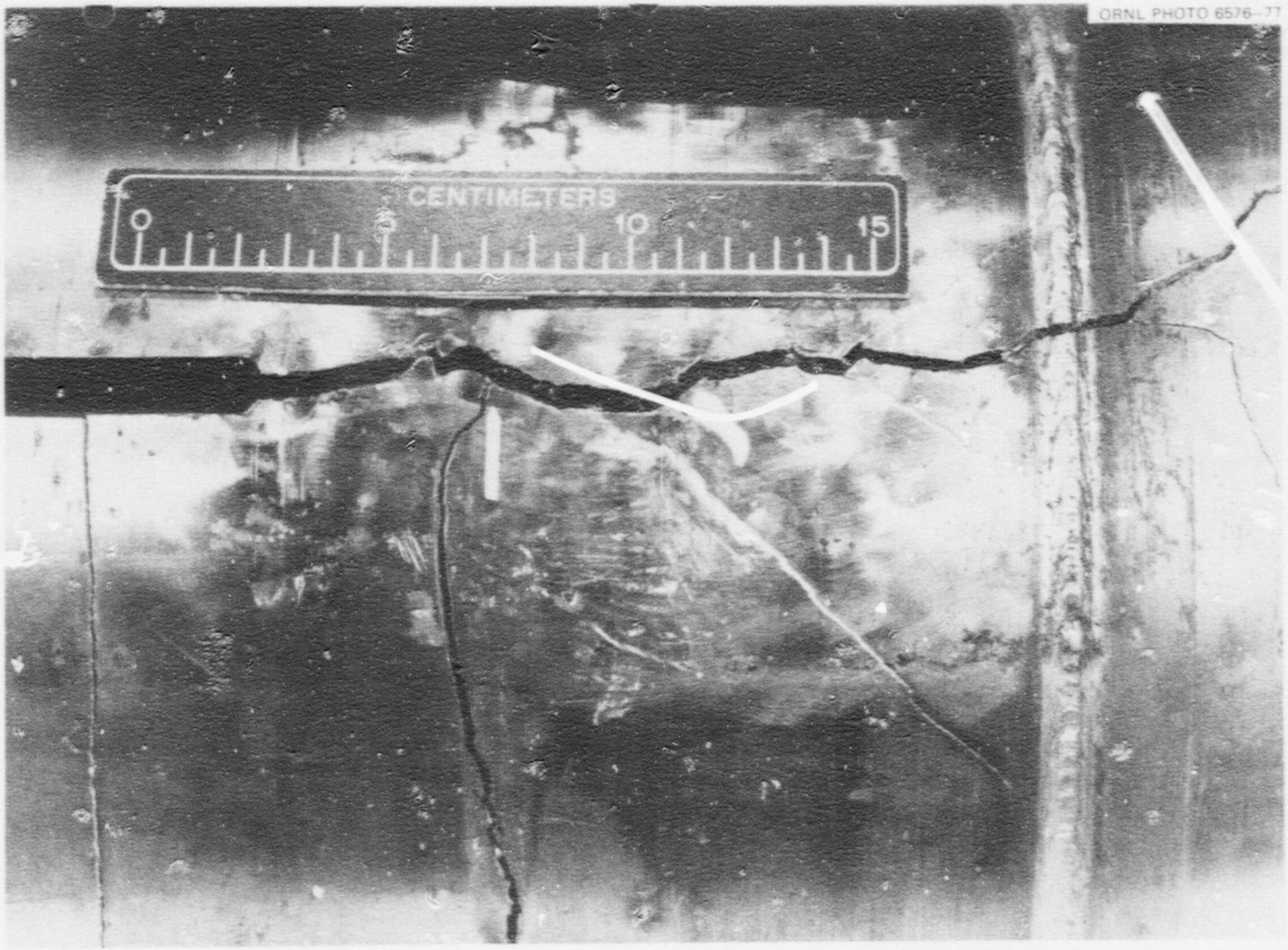

Fig. 51. Crack-initiation region of third model test after removal of ladder gage. The white arrow indicates the brittle-to-tough transition region (1 cm = 0.394 in.).

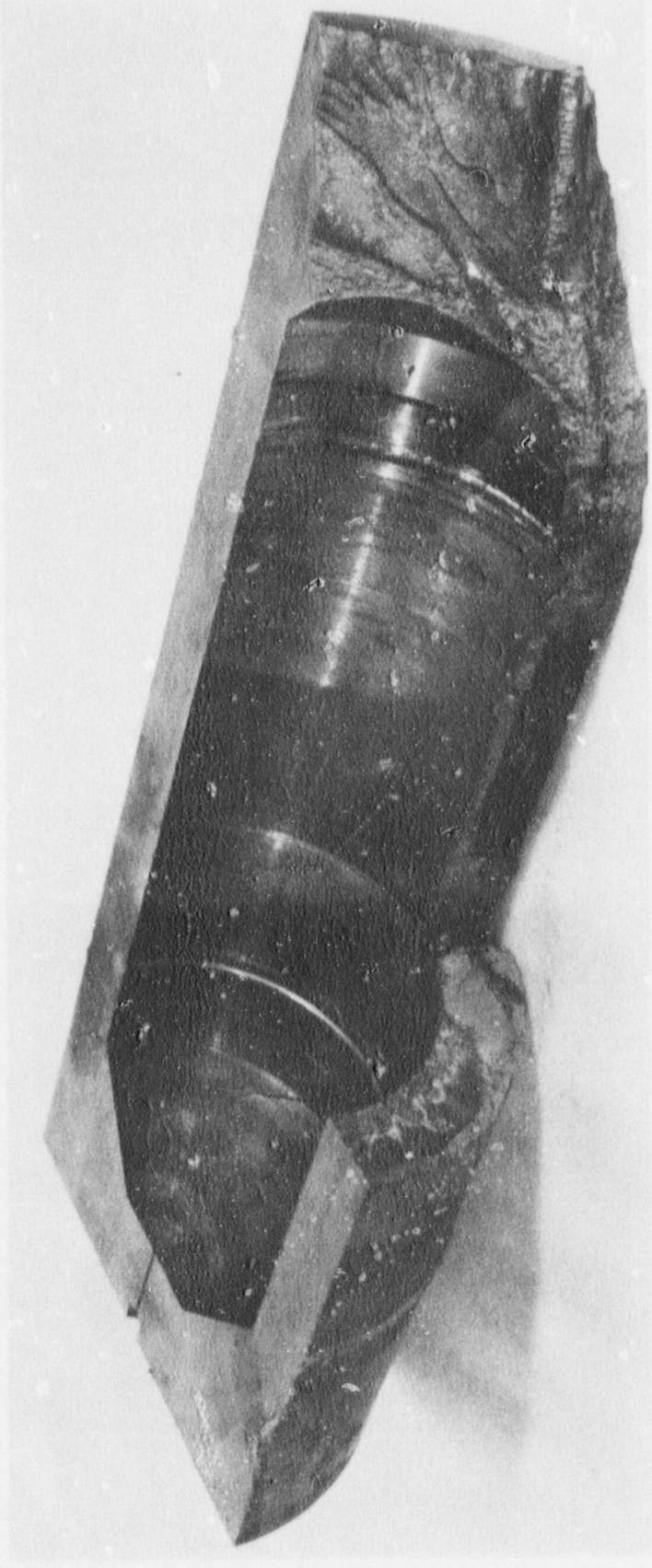

ORNL PHOTO 6767-77

Fig. 52. Third crack-arrest model after one longitudinal sawcut bisecting the model.

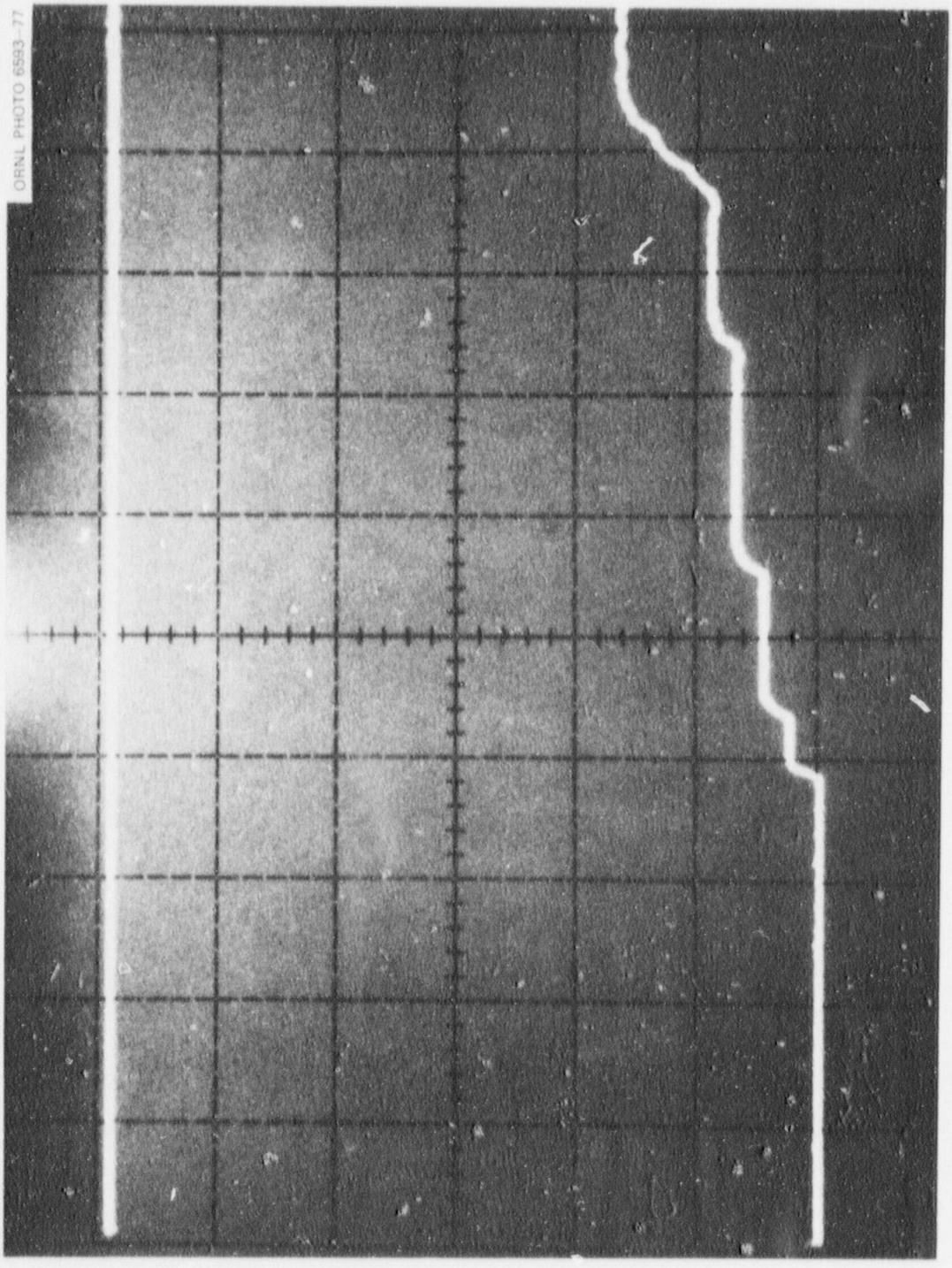

Fig. 53. Oscilloscope traces showing pressure (upper trace) and ladder gage output (lower trace) vs time. Each major horizontal division is 20 μsec.

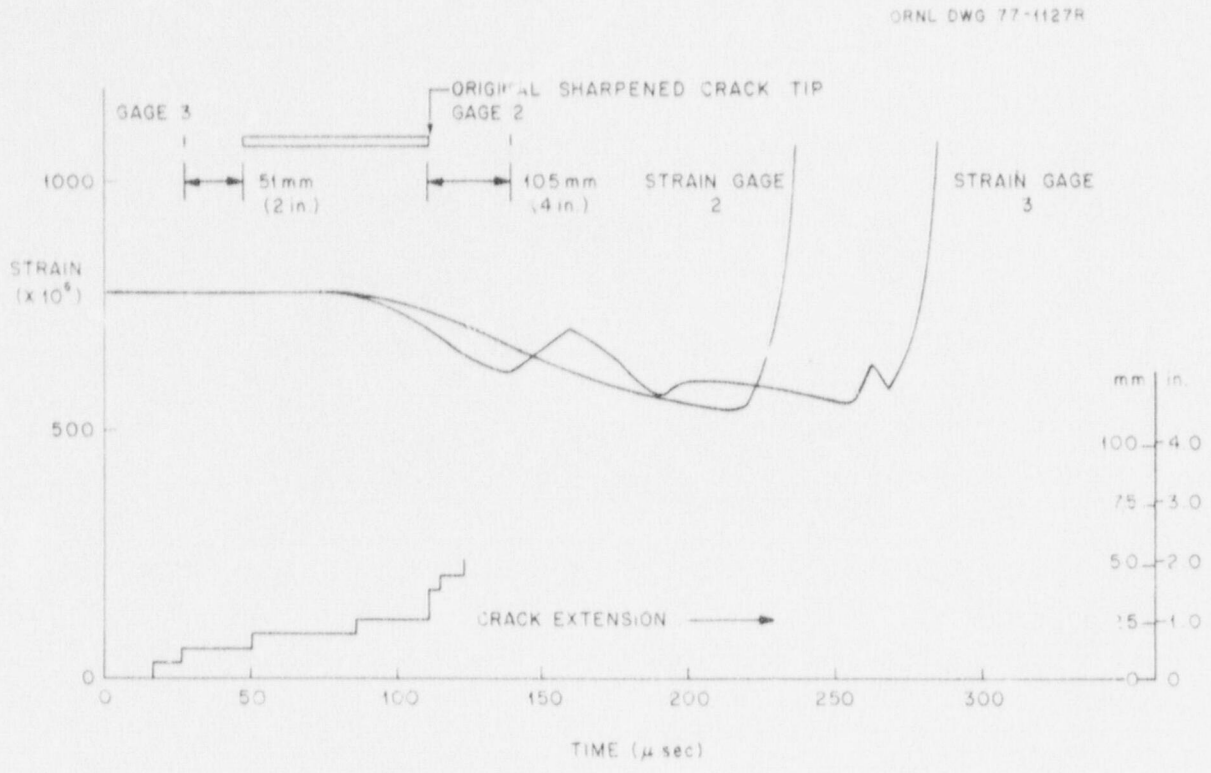

Fig. 54. Circumferential strains and crack extension as a function of time for the third crack-arrest model test. Test temperature was -47°C (-52°F).

crack (i.e., from the blunt end) had the same velocity as the right running crack, it follows that the right running crack started much earlier and, in fact, induced the subsequent cracks that are seen in Fig. 50.

Figure 55 shows the fracture plane and the sharpened starter crack for the third model test. The sharpened starter crack did not extend through the entire 38-mm (1.5-in.) thickness of the model wall; instead, it extended ∿25 mm (∿1.0 in.), measured from the outside surface of the model and along the machined slot. The fact that uncracked material existed at the base of the flaw could possibly account for the ability of the vessel to withstand much higher pressures than would be expected from the analysis and the previous two tests at higher temperatures. The dark, partly circular region adjacent to the machined notch and the rule in the upper photograph in Fig. 55 is considered to be the stable crack extension observed during the test of the third model at the -22°C (-7°F) test temperature. That region was sufficiently corroded to prevent the use of

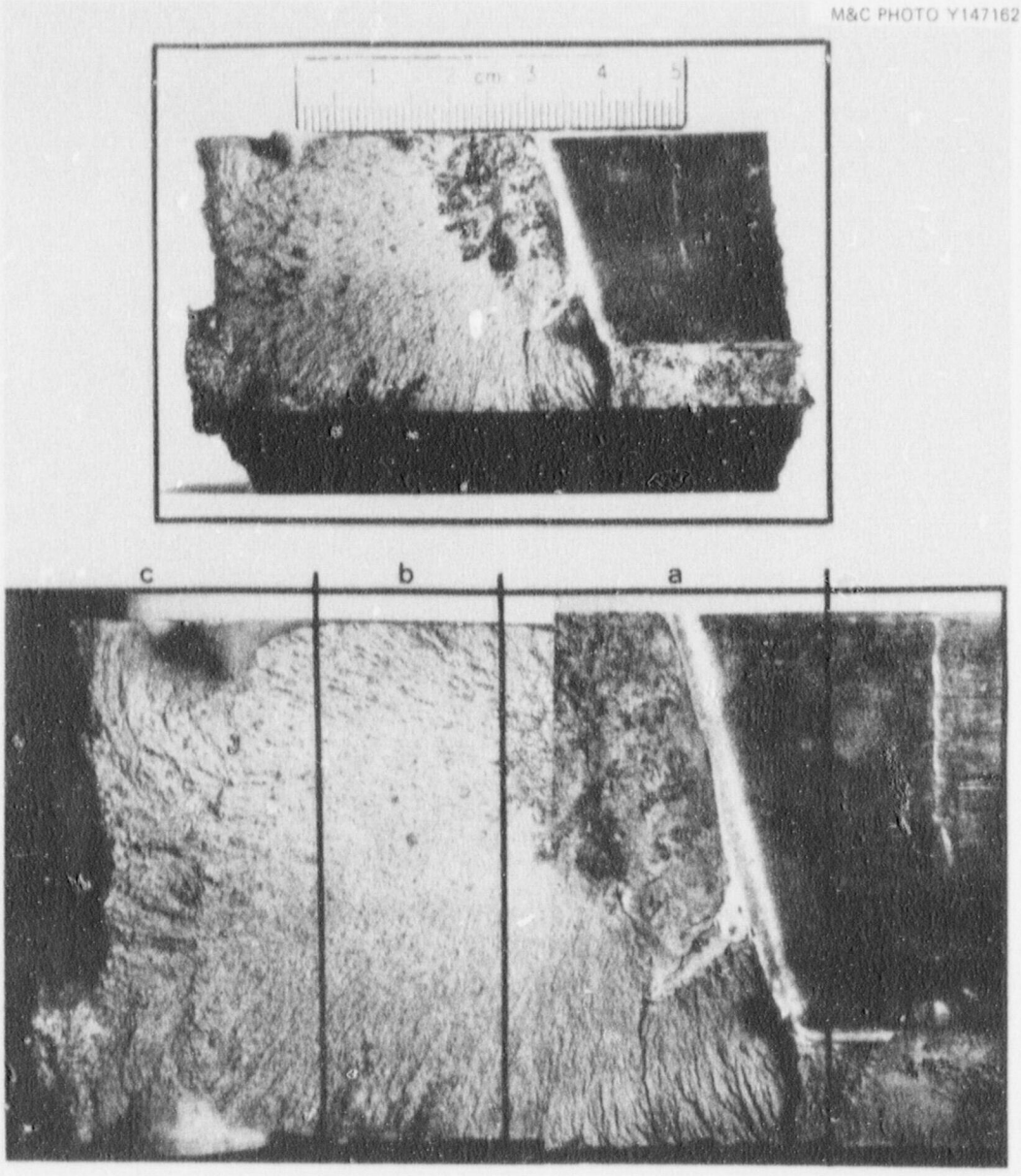

Fig. 55. Sectioning procedure for preparing samples for scanning electron microscopy in the third crack arrest model test (1 cm = 0.394 in.). (Original reduced 25%)

SEM to examine it. Figure 56 is a scanning electron micrograph taken of a region a short distance from the darkened area on the fracture surface shown in Fig. 55. The micrograph shows a cleavage mode of fracture, which seems consistent with the high crack velocity that was measured by the ladder gages.

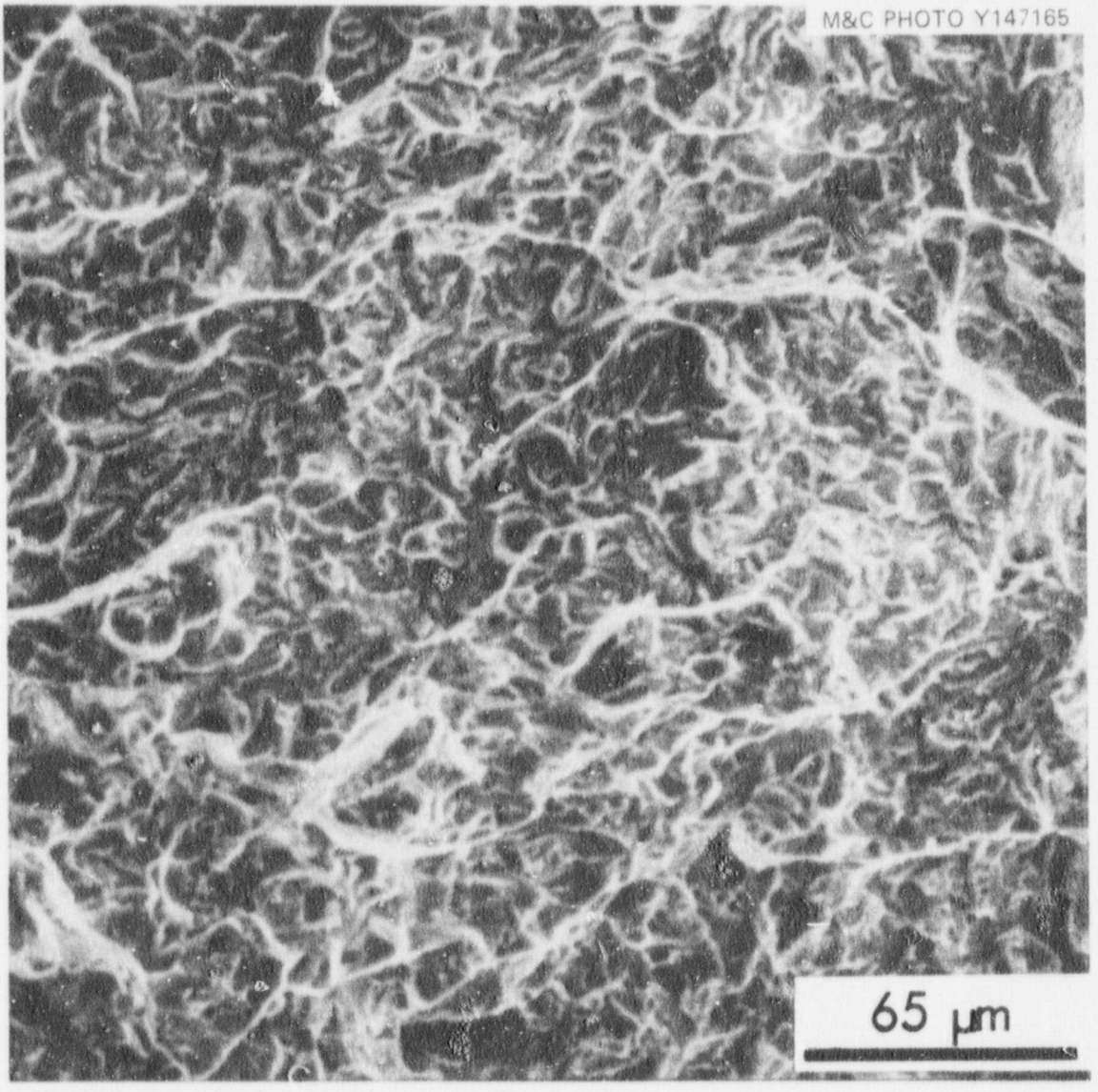

Fig. 56. Scanning electron micrograph of the region identified as *a* in Fig. 55. The region exhibits a cleavage mode.

9. DISCUSSION

Figure 57 shows stress-intensity factors for the first and second models which were calculated from the pressure and crack length at the instant the ladder gages indicated breaks (i.e., crack extension). For the purpose of making calculations, it was assumed that the progressing crack fronts remained straight. The stress-intensity factors were calculated using the previously discussed expression,

$$K_I = M\sigma\sqrt{\pi a} \ , \tag{11}$$

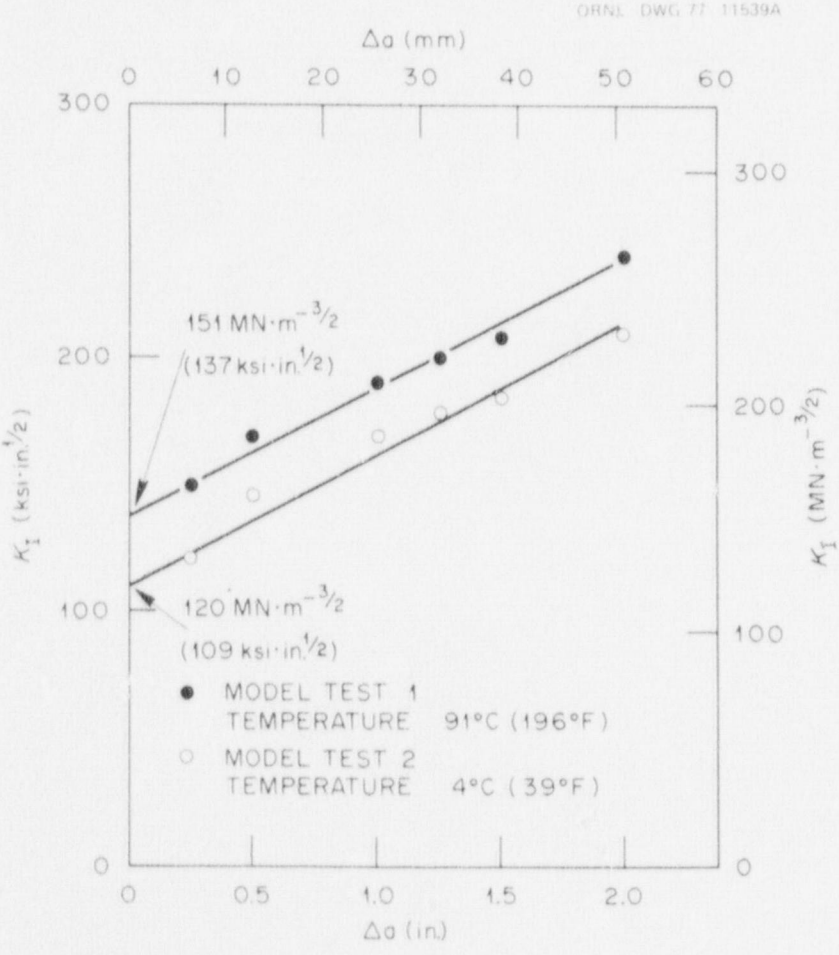

Fig. 57. Statically calculated stress-intensity factors based on instantaneous crack length and pressure during crack extension for crack-arrest model tests 1 and 2.

with M and σ given by

$$M = \left(1 + 1.61 \frac{a^2}{Rt}\right)^{1/2} \tag{12}$$

and

$$\sigma = \frac{PR}{t} , \tag{13}$$

where a, R, t, and P are, respectively, the crack half-length, the cylinder radius, the cylinder wall thickness, and the model internal pressure. The curves in Fig. 57 resemble resistance-type curves in that the toughness of the material increased with crack extension. The curves were extrapolated to zero crack extension so that an estimate could be made of the stress-intensity factor that existed at the onset of stable crack growth. The stress-intensity factors at initiation for the third model were also calculated from Eq. (11) and were found to be 152 $MN \cdot m^{-3/2}$* (138 $ksi \cdot in.^{1/2}$) at the first test temperature [-22°C (-7°F)] and 187 $MN \cdot m^{-3/2}$ (170 $ksi \cdot in.^{1/2}$) at the second test temperature [-47°C (-52°F)]. The fact that the stress-intensity factor calculated for the third model was significantly higher than those calculated for the first two models (even though the as-quenched plate 04 material used in the third model had inferior Charpy impact energies and inferior precracked Charpy specimen toughnesses relative to the as-quenched plate 03 used in the first two models) is most likely a consequence of the fact that the sharpened leading edge of the flaw in the third model did not penetrate entirely through the model wall, as previously noted. It would thus seem

---

*A factor of 0.91 was applied to the stress-intensity factor that was calculated using pressure and crack length at the instant the first leg of the ladder was broken. The value of 0.91 is equal to the ratio of the stress-intensity factor at zero crack extension to the stress-intensity factor after a crack extension of 6.3 mm (0.25 in.) for the first and second models.

that the load was redistributed to the unbroken segment of the crack front and that crack extension was thereby inhibited. It is of interest to note that the failure pressure for the third model at the -47°C (-52°F) test temperature was nearly the same pressure at which the earlier test of the same model was terminated after only slight crack extension when the model was being held at -22°C (-7°F). This type of behavior, while not conclusive, is at least consistent with warm-prestress results reported by Loss, Gray, and Hawthorne.[23]

The high yield stress of the as-quenched material implies that considerable constraint existed near the crack tips in the models. According to the ASTM E-399 validity criterion for thickness, a 38-mm-thick (1.5-in.) section of material with a 1027-MPa (149-ksi) yield stress could develop a valid K_{Ic} of up to 127 $MN \cdot m^{-3/2}$ (116 $ksi \cdot in.^{1/2}$). Thus, the values of toughness calculated from the model tests are close to being within the thickness requirement placed on plane-strain fracture toughness measurements.

Table 6 summarizes the toughnesses at the model test temperatures which were determined either directly from small specimens (e.g., precracked Charpy specimens) or by means of correlations using Charpy impact energies. For correlations requiring a yield strength or modulus, values of 1086 MPa (157 ksi) and 200 GPa (29×10^6 psi) were used, respectively. The toughness values determined from the model tests are also listed in Table 6, for purposes of comparison. It should be reemphasized that the toughness values determined from the model tests are based on extrapolations to zero crack length using large-crack-extension data. The precracked Charpy specimen toughnesses are uniformly below the toughness values determined from the model tests, although only slightly in the case of the second model test. The second model test resulted in a toughness value somewhat lower than the single 25.4-mm-thick (1.0-in.) compact-tension specimen value but easily within a scatter band. This result would tend to confirm that the EB weld did in fact provide a sharp crack tip.

The values of toughness determined from Charpy correlations spanned a considerable range. The Rolfe-Novak[24] correlation applied only to upper-shelf conditions, and thus it is applicable only to the first model

Table 6. Summary of small specimen toughness and model test results

Model No.	Test temperature [°C (°F)]	Plate No.	Charpy V-notch (CVN) energy [J (ft-lb)]	Small specimen toughness [MN·m$^{-3/2}$ (ksi·in.$^{1/2}$)]		Toughness determined from model test [MN·m$^{-3/2}$ (ksi·in.$^{1/2}$)]	Comments
				Direct	Charpy correlation		
1	91 (196)	03	41 (30)	99[a] (90)	145[b] (132)	151 (137)	Upper shelf
					172[c] (157)		
					111[d] (101)		
2	4 (39)	03	20 (15)	115[e] (105)	51[f] (49)	120 (109)	Transition
				140[e] (127)	65[g] (59)		
					130[c] (118)		
					64[h] (58)		
					90[d] (82)		
3	-22 (-7)	04	14 (10)	85[a] (77)	42[f] (38)	152 (138)	Flaw partially sharpened
					53[g] (48)		
					121[c] (110)		
					47[h] (43)		
					67[d] (61)		
3	-47 (-52)	04	11 (8)	77[a] (70)	37[f] (34)	187 (170)	Possible warm prestressing
					48[g] (43)		
					116[c] (106)		
					40[h] (36)		
					55[d] (50)		

[a] Precracked Charpy specimen.

[b] Rolfe-Novak (Ref. 24): $(K_{Ic}/\sigma_y)^2 = 5[(CVN/\sigma_y) - 0.05]$ (English units).

[c] Parry-Lazzeri (Ref. 28).

[d] Marandet-Sanz (Ref. 27).

[e] 25-mm-thick (1-in.) compact-tension specimen.

[f] Barsom-Rolfe (Ref. 24): $K_{Ic}^2/E = 5$ CVN (English units) T shift = 0°F for $\sigma_y > 140$ ksi.

[g] Corten-Sailors (Ref. 25): $K_{Ic}^2/E = 8$ CVN (English units).

[h] Barsom-Rolfe (Ref. 26): $K_{Ic}^2/E = (CVN)^{3/2}$ (English units).

test, where the correlation does agree quite well with the value determined from the model test. Three Charpy impact energy correlations[24-26] have been developed for the transition range of Charpy energies. All the toughnesses that were calculated using the transition range correlations were significantly lower than the estimates of toughness values determined from the model tests. This may, in part, be a result of the transition range correlations being intentionally conservative and intended for lower-strength steels. The Marandt-Sanz[27] correlation, which was developed for quenched-and-tempered A533 and for the transition region, depends on the construction of a toughness vs temperature curve from Charpy impact energy data; it also predicted toughnesses that were low relative to values determined from the model tests. The Begley-Longsdon[24] method is also predicated on the construction of a toughness vs temperature curve, but it was not applied in these studies because the percent of cleavage or ductile failure of the Charpy impact specimens could not be readily determined. The final correlation used was an empirical relationship established by Parry and Lazzeri[28] using Charpy impact data and the results of an extensive series of tests involving through-the-wall axial flaws similiar to those placed in the pressure vessel models discussed here. The toughnesses estimated by the Parry and Lazzeri method are in fair agreement with the first and second model tests and below that for the third model, which, as previously explained, might be expected. It is interesting to note, however, that Parry and Lazzeri also report cases of vessel failure at lower transition temperatures, where the pressures at failure were considerably above the pressures that could be predicted from their correlation.

The extensive slow, stable crack extension that occurred during the testing of the first two models and the less extensive but significant stable crack extension in the third model test at -22°C (-7°F) were not expected. The apparent toughnesses determined from the model tests were not greatly different from E-399 valid toughness for the model wall thicknesses, and thus the size of the plastic zone near the crack tips was small. The one piece of evidence that might have signaled extensive stable crack growth was that the static and dynamic precracked Charpy specimen toughnesses were not appreciably different. This suggests that rate effects would not

be significant for this quenched-only material, and thus there would be less propensity for failure by unstable fast fracture.

The two crack-run and -arrest events characterized by the loud "pings" during the second model test produced some unexpected results. The first short burst of crack extension initiated and arrested in macroscopically homogeneous material. The pressure was essentially constant during extension, and the stress-intensity factor thus increased during propagation. The crack extension was small relative to the dimensions of the vessel; therefore, the dynamic stress-intensity factor would probably not differ significantly from the static value. The same observations apply to the second run-arrest event except that the crack apparently arrested in the tough material. The stress-intensity factor at arrest, however, far exceeded the published values of toughness. This can be seen in Fig. 58, which shows the BCL data,[3] the MRL data[4] for A533, the static and dynamic precracked Charpy data for plate W57, and the statically determined stress-intensity factor for the second run-arrest event in the second model test. The static and dynamic toughness curves were included merely for comparison with generally accepted crack-arrest values. The very high arrest value suggested by the crack-arrest model data point could be a result of shear lip formation in the model test, which does not occur in standard crack-arrest specimens employing side grooves. Thus, the resistance to fast fracture in the case of the crack-arrest model could be much greater than the plane-strain values reported by BCL and MRL. The velocity at which the crack arrested could be another reason for the high apparent crack-arrest value in the model test. It has been shown[3,5,6] that the resistance to crack propagation is dependent on crack velocity. Thus, if the crack did not attain the velocity associated with the minimum on a K_{ID} vs crack velocity curve, the appropriate crack-arrest stress intensity could be much larger than the minimum values that appear in the literature.

Equation (11) was also used to calculate the stress-intensity factor for the third crack-arrest model test at -47°C (-52°F), using the crack length at the instant the running crack left the brittle material and entered the tough material. It was assumed that the model internal pressure and the hoop stress did not change appreciably during the 51-mm (2.0-in.) propagation distance. The assump ion is considered reasonable in light of

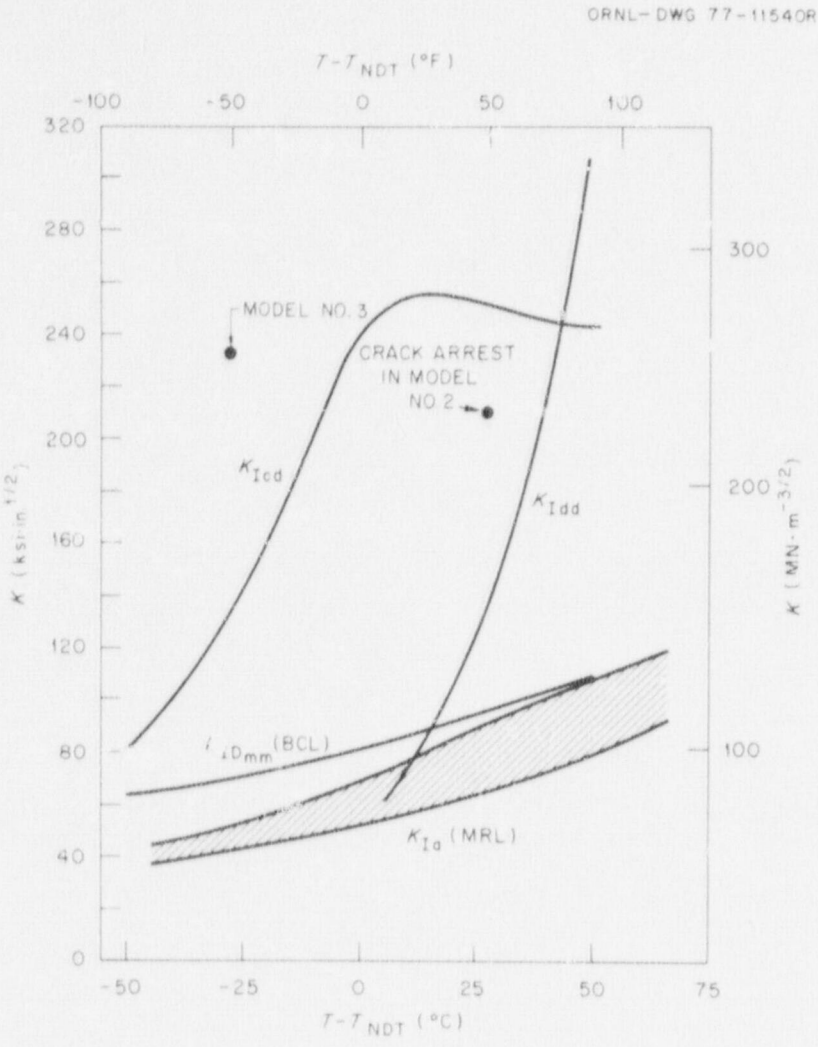

Fig. 58. Crack-arrest data vs temperature for quenched-and-tempered A533B. The crack-arrest points indicate the value of K at the instant of the second "ping" in the second model test and the value of K at the instant the rapidly propagating crack tip passed through the brittle-to-tough transition in the third model test.

the strain gage data shown in Fig. 54. The results, which are presented in Appendices A and B, indicate that the use of a statically calculated stress-intensity factor is reasonable for a crack speed of 410 m/sec (16,140 in./sec) in a representative crack-arrest model configuration. The result of this calculation is also shown in Fig. 58. The stress intensity associated with the running crack exceeded even the static fracture toughness of the tough material, and thus crack arrest would not have been expected.

The development of shear lips on the inside and outside surfaces of the second crack-arrest model and the first arrest event in that test indicate that side grooves to guide the flaw and to better maintain plane-strain conditions for the axial crack configuration would probably be required for a large-scale test if a similar configuration were to be used. Such side grooves would probably need to be deeper where tempering of the brittle center section was presumably caused by the EB welds. An example of deeper side grooves is shown in Fig. 59. The presence of such grooves would assist propagation of the crack through the fusion zone of the EB weld, thereby assuring further penetration of the crack into the quenched-and-tempered material. The second arrest event in the second model test was accompanied by partial propagation through the fusion zone, while in the third crack-arrest model there was a small circumferential excursion (6 mm, or 0.25 in.) before the crack propagated through the fusion zone. As a consequence of the stable crack growth and the shear lip formation in the models, the feasibility of the axial crack configuration remains uncertain. Thus, if an axial crack configuration is to be used on a large-scale test, further model testing should be performed.

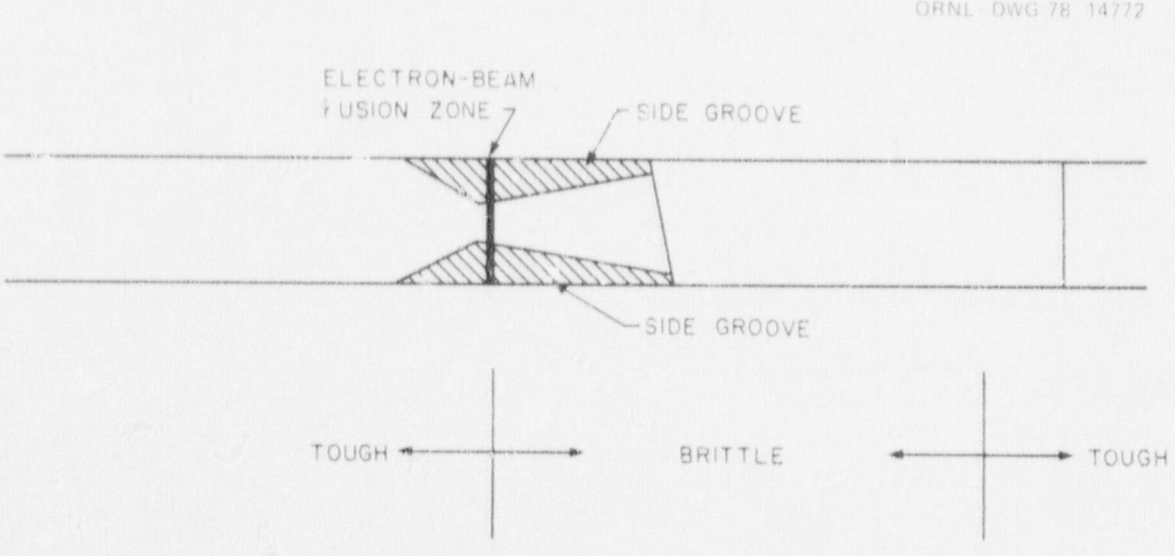

Fig. 59. An example of side grooves that may be necessary to allow a satisfactory crack-arrest experiment if the basic crack-arrest model configuration were to be used for further testing.

10. CONCLUSIONS

The goal of producing both arrest and nonarrest of a rapidly propagating crack in quenched-and-tempered A533, grade B, class 1 material for a pressurized vessel configuration was met, with qualifications. An interesting finding from these model tests was the very high resistance to unstable crack extension of the quenched-only A533 starter material. The initiation of crack extension using toughness values from small specimens was reasonably well predicted using linear elastic analysis. The analysis did not, however, lead to anticipation of the extensive stable crack extension or the increase in toughness that accompanied crack extension. The arrest and nonarrest events produced in the second and third model tests were not inconsistent with existing theories relating to crack arrest.

Appendix A

PARAMETRIC STUDY OF DYNAMIC AXIAL CRACK PROPAGATION IN A CYLINDRICAL SECTION

General Description of Analysis Method

Broberg[29,30] considered the problem of a crack suddenly appearing in a two-dimensional infinite body and propagating with arbitrary constant crack tip velocities. A particularly useful finding by Broberg was that the expansion of the stress field about the propagating crack tip contained a square-root singularity, which is normally identified as the stress-intensity factor. A discussion of Broberg's solution is contained in Ref. 31.

Freund[32-35] has considered a class of dynamic crack propagation problems and has presented results for arbitrary (spatial and temporal) tractions on the crack surfaces and for nonuniform crack tip velocities. Broberg's and Freund's stipulation of infinite bodies implies that stress wave reflections and interactions at boundaries, such as would occur in real structures, are not accounted for. In some cases, relaxing the infinite body restriction in order to apply the results from Broberg or Freund could introduce inconsequential or, at least, acceptable error. This situation would not be expected to obtain for small-scale dynamic crack test specimens with crack lengths comparable to a lateral dimension (see, for example, the discussion in Section 2 of Hahn et al.[36]). It is the thesis of the following discussion that, for axially propagating through-the-wall cracks in cylinders where the crack length is small relative to the cylinder circumference and length, the idealization of the cylinder, with an appropriate correction for bulging, as an infinite body may yield satisfactory results.

It should be pointed out that since the cylinder has a finite wall thickness, geometric dispersion of stress waves such as found in flat plates or rods[37-39] would be expected. However, since geometric dispersion tends to separate waves of different lengths, peak stresses would most likely be reduced. Therefore, geometric dispersion could be, in that sense, dissipative; and thus ignoring its effect would tend to strengthen an

otherwise adequate argument that wave reflections returning to the crack tip region from free surfaces can be neglected under some conditions. For this reason and because of the complexities associated with dispersion, its effect is assumed to be negligible for the proposed model.

If the cylinder is taken to be long relative to the crack length, then because of the assumed absence of dispersion, the only stress waves that could affect the crack tip behavior predicted by Broberg are those which completely traverse the cylinder circumference. If it could be shown that this effect is small, Broberg's solution, modified by a bulging factor, has the possibility of being a satisfactory model. However, it is reasonable to expect that variable crack tip velocities, which are not covered by Broberg's solution, would have a significant effect. The solution given by Freund, however, accommodates nonuniform velocities and a more general state of stress, but it has the limitation that stress wave reflections between crack tips must be insignificant. This latter restriction is not as severe as might be supposed, and its effect can be estimated from results shown in Fig. A.1, which was published by Freund.[32] Figure A.1 presents (for crack geometries with equivalent static strain energy-release rates and thus equivalent static stress-intensity factors) the ratio of actual dynamic to statically calculated strain energy-release rates vs the dimensionless crack tip velocity (normalized with respect to the Rayleigh speed V_R) for materials with Poisson ratios of 2/7 and 1/2. The solid lines are the results from Freund's[33] analysis, and the dashed line is from the analysis given by Broberg.[30] For dimensionless crack speeds less than 0.5,* the difference is less than 10%. Since Freund's solution has much broader applicability and seems to be not significantly different from Broberg's, the Freund solution[33] will be used exclusively in the subsequent analysis and discussion unless otherwise specified. A principal consequence of Freund's solution is the following relationship:

$$K_D(\dot{a}, a) = k(\dot{a})\, K_s(a) \ , \qquad (A.1)$$

*The maximum dimensionless crack speeds reported for steels have been of the order of 0.5 or less. See, for example, Ref. 40 or 41.

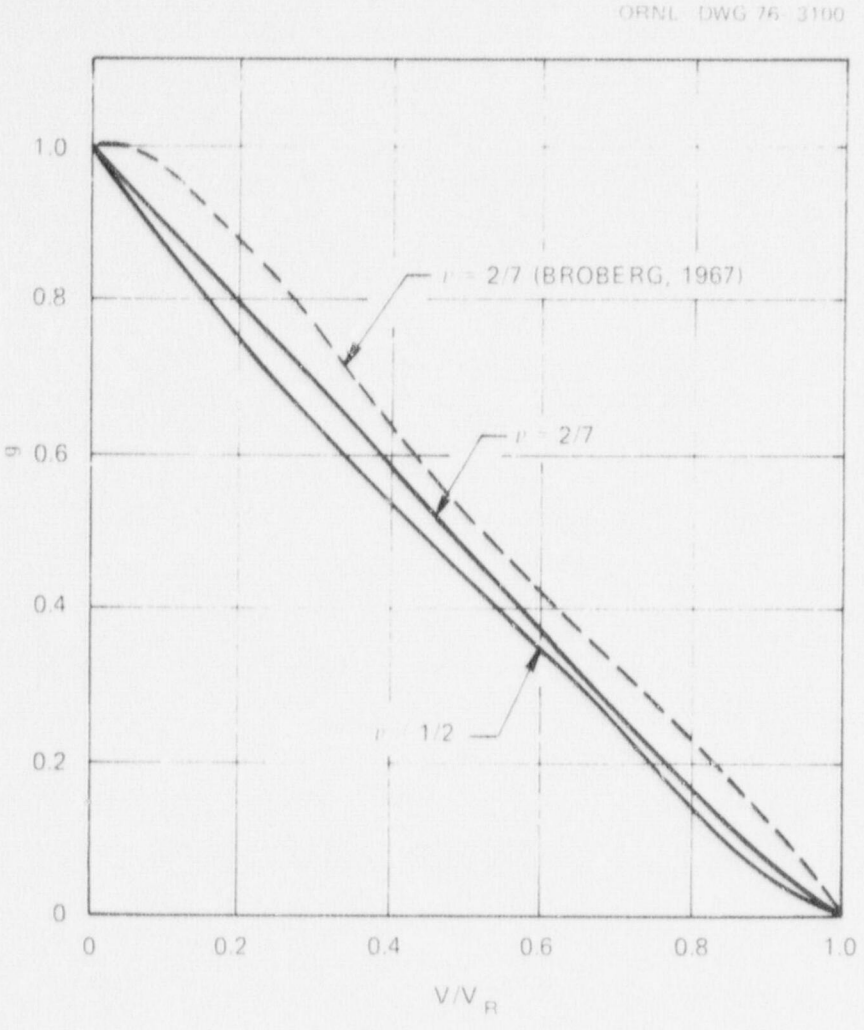

Fig. A.1. Ratio of dynamic to static energy-release rates vs dimensionless crack speed for $\nu = 2/7$ and $1/2$ (from Freund, Ref. 32).

where K_D is the dynamic stress-intensity factor; K_s is the statically calculated stress-intensity factor, which is a function of the instantaneous crack length (a); and k is a function of only the instantaneous crack tip velocity ($\dot{a}$). The latter function was found by Freund[33] to be

$$k^{-1}(\dot{a}) = \dot{a}\, S_+(1/\dot{a})\, [1/\dot{a} + 1/(V_R - \dot{a})]\, (1 - \dot{a}/V_L)^{1/2} , \qquad (A.2)$$

where $S_+(1/\dot{a})$ is a function that differs only slightly from unity, V_R is the Rayleigh wave velocity, and V_L is the longitudinal wave velocity.

Merkle[42] and Hoagland et al.[43] have presented explanations of the observed behavior of propagating cracks in terms of a material property, called dynamic toughness, which appears to be a function of the crack tip velocity only. Hoagland et al. have also discussed the relationship between dynamic toughness and the dynamic strain energy-release rate and have observed that arrest criteria based on either of these material descriptions would be essentially equivalent. The criterion suggested by Merkle (namely, that a crack will propagate as long as the dynamic stress-intensity factor exceeds some minimum toughness value and that the crack tip velocity is uniquely determined by the prevailing dynamic stress-intensity factor) is the criterion chosen for the method of analysis proposed here.

Since the material description is crucial to this model (and most likely to any other model that would yield the minimum requisite information), a brief description of a recent study of the property of one material would be appropriate. Irwin, Dalley, Kobayashi, and Etheridge[44] have studied a photoelastic polymeric material (Homalite 100) and have experimentally measured dynamic stress-intensity factors and concurrent crack tip velocities. Their Fig. 7.2 is reproduced here as Fig. A.2. Since similiar data for structural materials such as steel are as yet unavailable, the behavior of Homalite is used as a model for the subsequent analysis. This behavior is not unreasonable since steel also seems to have a limiting crack velocity. Hahn et al.[3] have demonstrated a similar relationship between dynamic toughness and crack tip velocity. The basic components of the analytic model have now been described.

An Estimate of the Effect of Stress Waves Traveling Around the Cylinder for a Through-the-Wall Axially Propagating Crack

The purpose of this section is to demonstrate that the stress waves, generated by a small, through-the-wall, axially propagating crack, which travel around the circumference of a cylinder and then impinge on the crack are likely to be negligible, as we assumed in the previous section. Sih, Embley, and Ravera[45] have considered the problem of a stationary finite crack in a two-dimensional body that is impacted by a plane stress

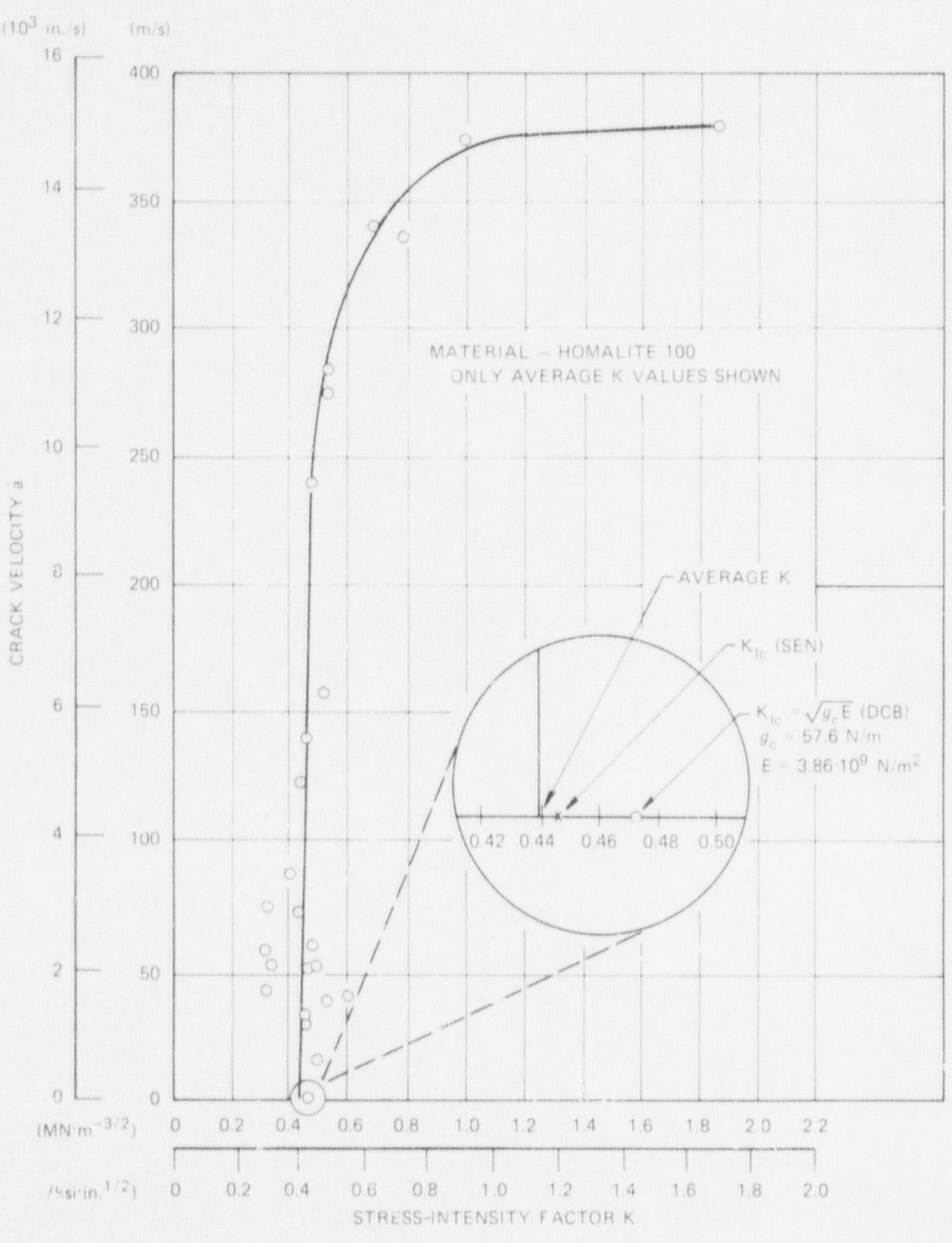

Fig. A.2. Crack velocity, ȧ, as a function of instantaneous stress-intensity factor, K (from Irwin et al., Ref. 44).

wave whose front is parallel to the crack, as shown in Fig. A.3. A principal result of their analysis was the determination of the stress-intensity factor as a function of dimensionless time. This result is shown in Fig. A.4, where the curve relevant to this discussion is labeled "Normal Impact (j = 1)." The other two solid curves pertain to a shear wave impact on finite cracks, and the dashed curves pertain to the impact of longitudinal and shear waves on semi-infinite cracks. These latter two curves would, of course, increase without bound with increasing time, because the static limit does not exist. Each of the three curves for finite-length cracks has an asymptotic value of unity, because the stress-intensity factors are normalized by the static value. Thus, for the very severe case of a step singularity in amplitude across a wave front, the dynamic stress-intensity factor overshoots the static value by approximately 25%.

Although the problem considered by Sih et al.[45] is quite different from that of the running crack impacted by stress waves which traverse the circumference of a cylinder, it can nevertheless be used to construct an estimate for the problem of interest. With that as the objective, the

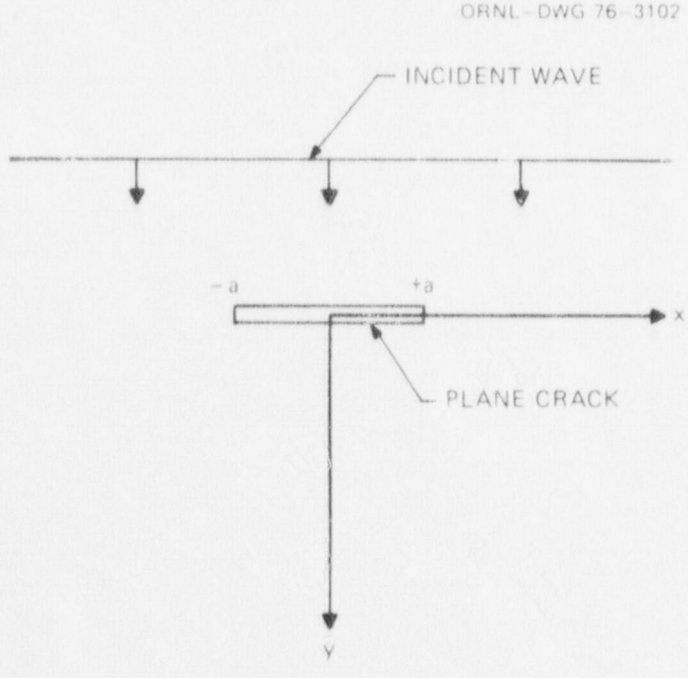

Fig. A.3. The problem considered by Sih et al.

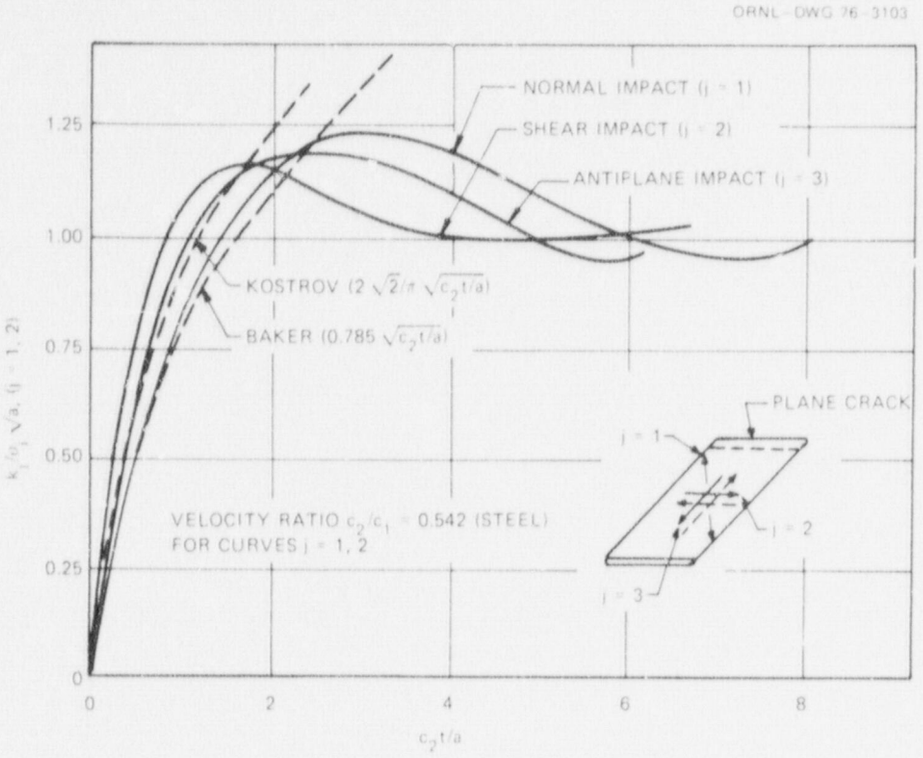

Fig. A.4. Dynamic stress-intensity factors (from Sih et al., Ref. 45).

following assumptions are made in order to facilitate such an estimate:

1. The stress wave generated by a rapidly propagating crack has a step increase in amplitude across the wave front.
2. The wave front is infinite in extent.
3. The stress level of the wave decreases with increasing distance from the crack in a manner similar to the decrease in the static stress field away from a pressurized crack under static conditions.

The reduction of the stress level of the outwardly propagating wave is a consequence of energy propagation outward from the crack tip region along the axis of the cylinder. An equivalent point of view would be that the flawed region of the cylinder is restrained by the unflawed region. It thus becomes necessary to calculate an equivalent stress level at a distance from the crack equal to the circumference of the cylinder.

Recently, Delameter, Herrman, and Barnett[46] presented a static analysis of an infinite elastic solid containing parallel rows of periodically

spaced cracks. The configuration they considered is shown in Fig. A.5. Delameter et al.[46] calculated nondimensional stress-intensity factors as a function of the quantities 2a, b, and d, which are defined in Fig. A.5. Results from the case of d/2a equal to infinity, which are shown in Table A.1, are of interest here because the cylinder is assumed to be infinitely long. If it is also assumed that a suddenly appearing flaw in the cylinder becomes subject to its static stress-intensity factor after the initial pulse and the first two subsequent reflections (caused by the initial stress wave traveling around the cylinder and encountering the crack), then it is possible to estimate the time history of the stress-intensity factor by applying the results of Sih et al.[45] and Delameter et al.[46] and by invoking the previously discussed simplifying assumptions. As examples, results are presented for two cases, with the cylinder circumference being taken first as twice the crack length and then as five times the crack length. Figure A.6 shows the dynamic stress-intensity factor as

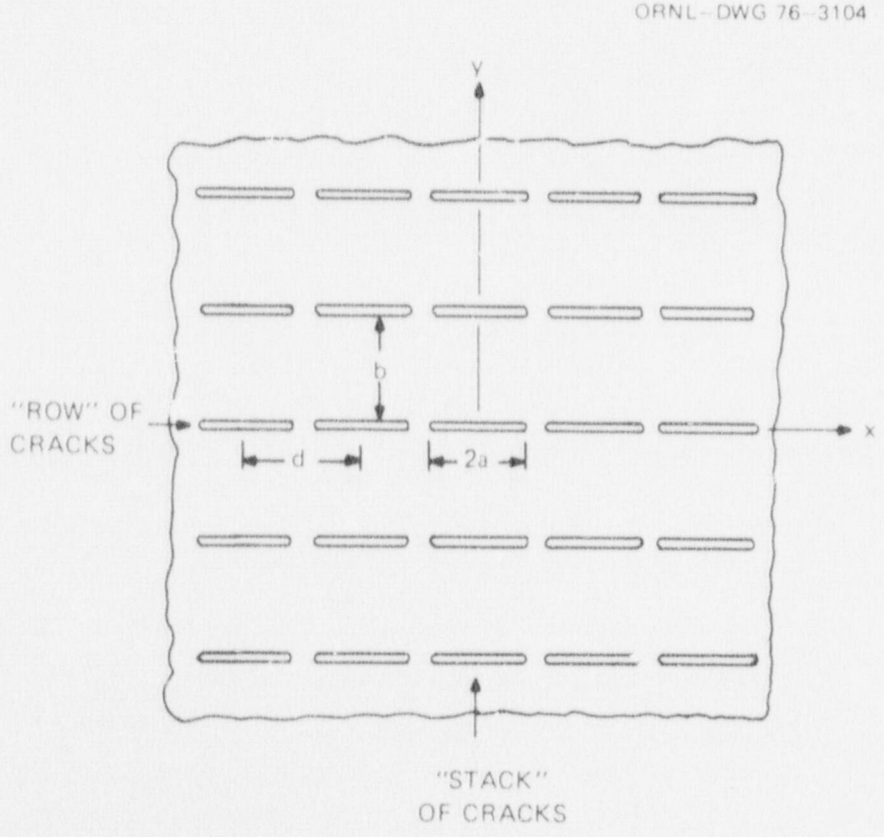

Fig. A.5. Doubly periodic rectangular array of cracks.

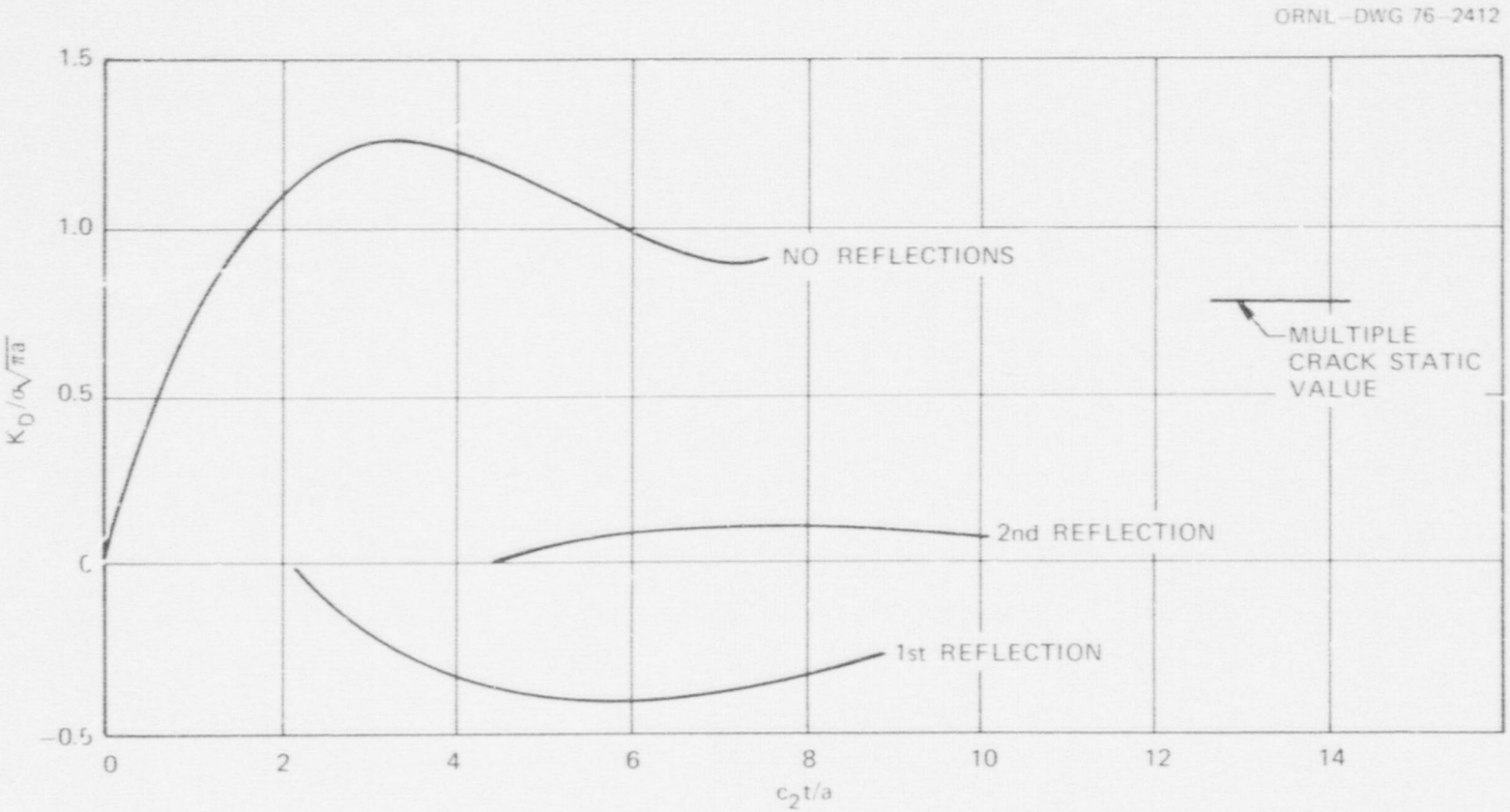

Fig. A.6. Dynamic stress-intensity factor vs time for a circumference equal to twice the crack length.

Table A.1. Nondimensional stress-intensity factor for $d/2a = \infty$ (Ref. 46)

b/2a	$K_I/\sigma(\pi a)^{1/2}$
1	0.5702
2	0.7896
3	0.8864
4	0.9309
5	0.9540
∞	1.0000

a function of nondimensionless time, considering the initial response and the first two reflected waves, for the case when the circumference is twice the crack length. The three responses are shown separately rather than superposed in order to more clearly illustrate the relative effects of the reflected waves. Figure A.7 presents similar results for the case when the circumference is five times the crack length. The results presented in Figs. A.6 and A.7 imply that the effects of reflected stress waves may be negligible for a cylinder with a circumference-to-crack-length ratio of 5 or more. Table A.2 lists the crack lengths for given types of vessels that could be analyzed by the proposed method (i.e., assuming a crack length that is small relative to the cylinder diameter).

Table A.2. Crack and vessel geometry for negligible reflections

Type of vessel	Outside diameter [m (in.)]	Maximum admissible crack length [m (in.)]
Reactor pressure vessel	4.9 (194)	3.1 (122)
Intermediate test vessel	0.99 (39)	0.52 (21)
Small-scale test vessel	0.15 (6)	0.08 (3.2)

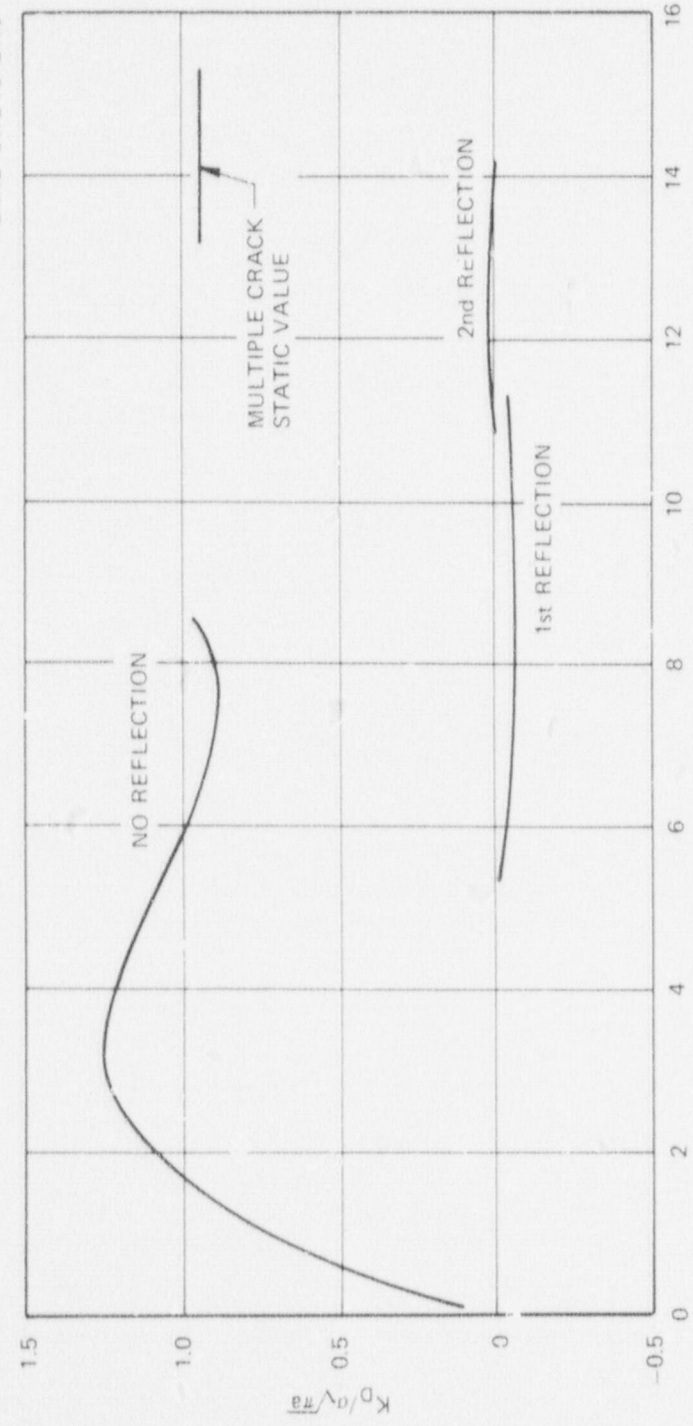

Fig. A.7. Dynamic stress-intensity factor vs time for a circumference equal to five times the crack length.

Examples

Consider a long circular cylinder composed of two materials as shown in Fig. A.8. The radius and wall thickness of the cylinder have been taken, for convenience only, to be the same as that for the HSST intermediate test vessels. It is assumed that a through-the-wall axial crack of length 2a exists in the insert material labeled A. Material B will be assumed to have the same elastic properties as A but a higher toughness. This configuration could be achieved, for example, by welding together materials with different heat treatments.

For real materials, of course, the dynamic fracture toughness (K_{ID}) vs the crack tip velocity must be determined experimentally. For the purpose of this analysis, a convenient representation will be assumed.

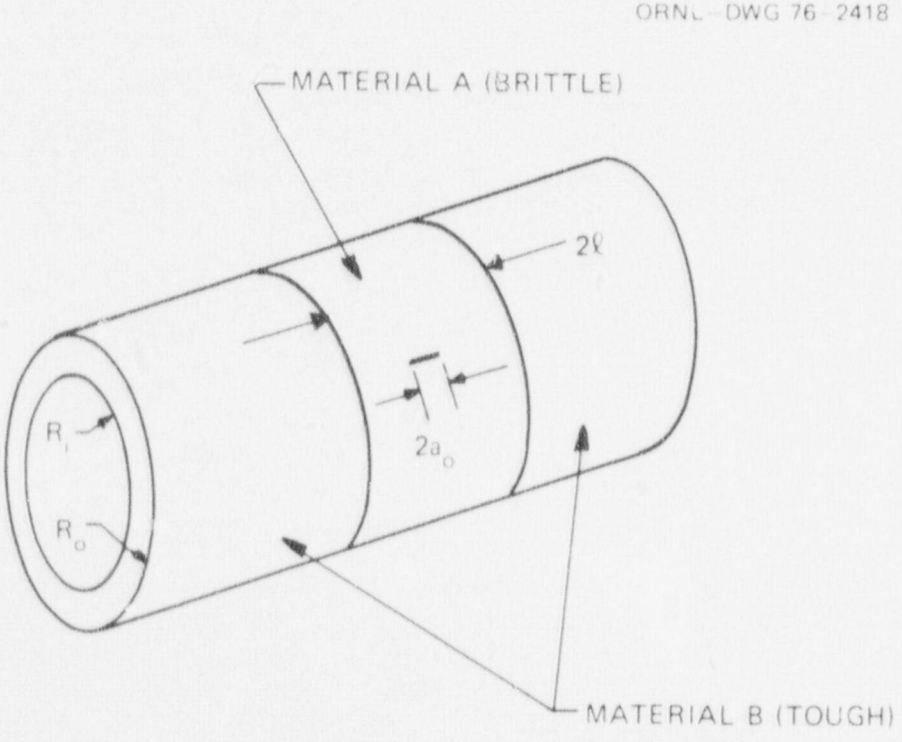

R_o = 0.495 m (19.5 in.)
R_i = 0.343 m (13.5 in.)
a_o = 0.0634 m (2.50 in.)
ℓ = 0.254 m (10 in.)

Fig. A.8. Geometry for sample problems.

The assumed relationship has the following form:

$$K_{ID}^{A,B}(\dot{a}) = \frac{K_{ID(min)}^{A,B}}{1 - \frac{\dot{a}}{V_{max}^{A,B}}}, \qquad (A.3)$$

where $K_{ID(min)}^{A,B}$ and $V_{max}^{A,B}$ are the static toughness and limiting crack tip velocities for materials A and B, respectively. For the subsequent analysis, $K_{ID(min)}$ was taken to be 100.0 MN·m$^{-3/2}$ (91.0 ksi·in.$^{1/2}$); $K_{ID(min)}^{B}$ was taken to be 350.0 MN·m$^{-3/2}$ (318.5 ksi·in.$^{1/2}$); V_{max}^{A} was taken to be 1500 m/sec (59,055 in./sec); and V_{max}^{B} was taken to be 1000 m/sec (39,370 in./sec). Figure A.9 shows curves of $\dot{a}$ vs K_{ID} for materials A and B, using Eq. (A.3) and the above values.

The dimensions of the cylinder, the initial crack length, and the length of cylindrical insert (material A) were the same for each of the three sample problems. Also, the same material characterization (i.e., the same as that shown in Fig. A.9) applied to each of the sample problems. The outside diameter was taken to be 0.990 m (38.98 in.); the inside diameter was taken to be 0.686 m (27.01 in.); the initial crack half-length was taken to be 0.0634 m (2.50 in.); and the length of the brittle insert was taken to be 0.54 m (20 in.).

The difference between the sample problems lies in either the loading or the assumed crack tip character. In the first sample problem, it is assumed that the static fracture toughness (K_{Ic}) is 1.01 times the minimum dynamic fracture toughness [$K_{ID(min)}$] and that the crack begins to propagate from each crack tip when the internal pressure in the cylinder reaches the critical pressure determined from linear elastic fracture mechanics, that is, 94.80 MN·m^{-2} (13,750 psi). The second sample problem is identical to the first, except that the static fracture toughness is 1.20 times the minimum dynamic fracture toughness. The third sample problem has the same geometry and static fracture toughness as the second, but in the third problem it is assumed that the crack propagates from only one crack tip. This situation could occur, for example, if one of the

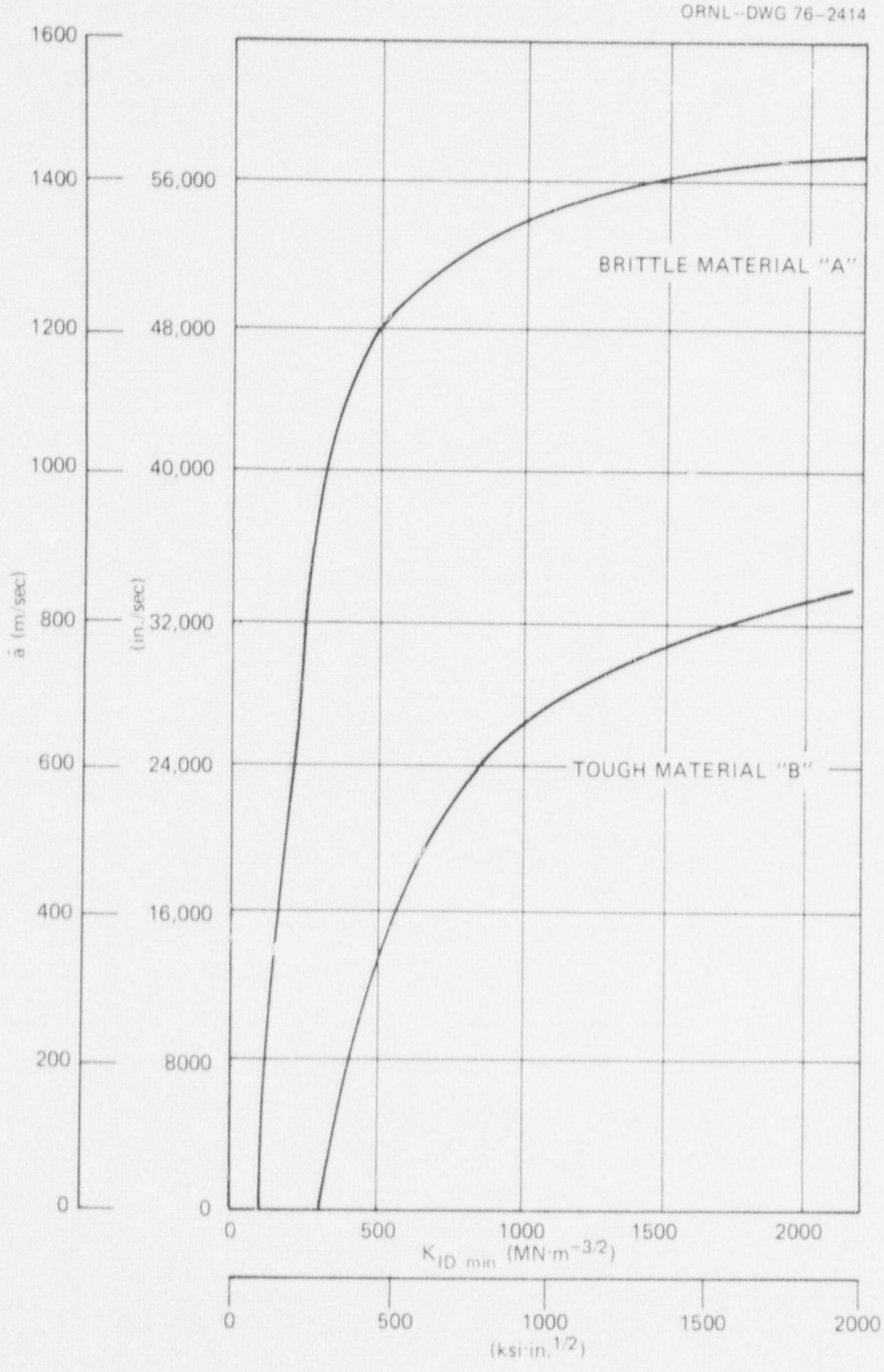

Fig. A.9. Crack tip velocity vs dynamic toughness for sample problems.

crack tips is more blunt than the other. It is also assumed (although it is not a necessary assumption) that once the crack begins to propagate, the pressure in the vessel remains constant in each of the sample problems. This would correspond either to no leak of the pressurizing fluid or perhaps to a very slight leak rate. The principal characteristics for the three sample problems are summarized in Table A.3, which also shows whether the analysis predicts arrest or nonarrest when the propagating crack encounters the tougher material.

Table A.3. Summary of sample problems

Sample problem No.	K_{Ic}	No. of moving crack tips	Crack arrest
1	1.01 $K_{ID(min)}$	2	Yes
2	1.20 $K_{ID(min)}$	2	No
3	1.20 $K_{ID(min)}$	1	Yes

The principal results from the analysis of the three sample problems are shown in Figs. A.10 to A.12. Figure A.10 is a plot of the crack tip velocity vs time measured from crack initiation for each problem. It can be seen from the plot that the crack tip velocity goes to zero for sample problems 1 and 3, which is an indication that the cracks for those two problems have arrested. The crack tip velocity for problem 2 decelerates suddenly when the crack encounters the tough material but again begins a gradual acceleration after entering the tough material. Figure A.11 is a plot of crack length vs time, and it can be seen that the arrest and sudden deceleration mentioned earlier does indeed occur at the instant the crack half-length is equal to half the length of the cylindrical insert [i.e., 0.254 m (10 in.)] for problems 1 and 2.* Figure A.12 is a plot of the dynamic stress-intensity factor vs time for each problem. When the

*For problem 3, the final crack length is actually equal to half the length of the cylinder insert plus the initial crack half-length [i.e., 0.159 m (12.50 in.)].

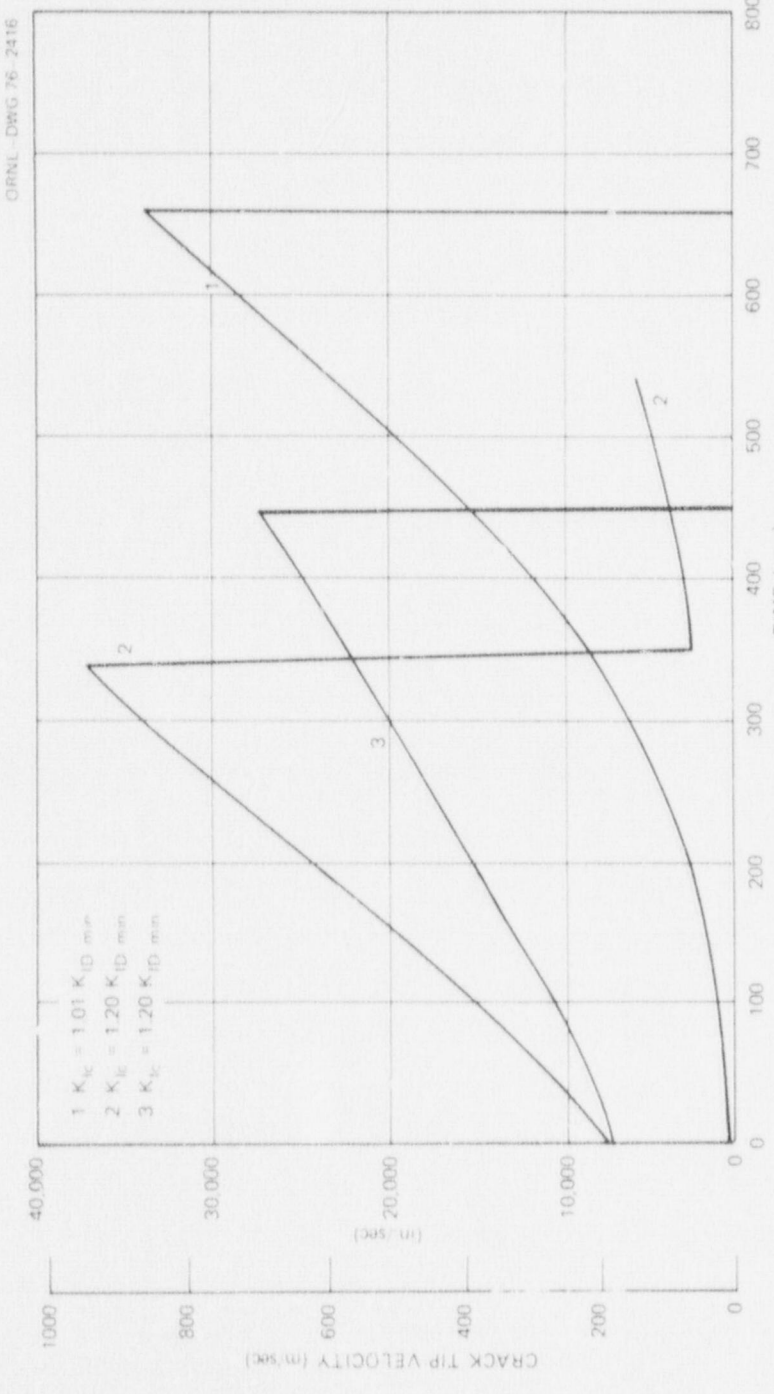

Fig. A.10. Crack tip velocity vs time.

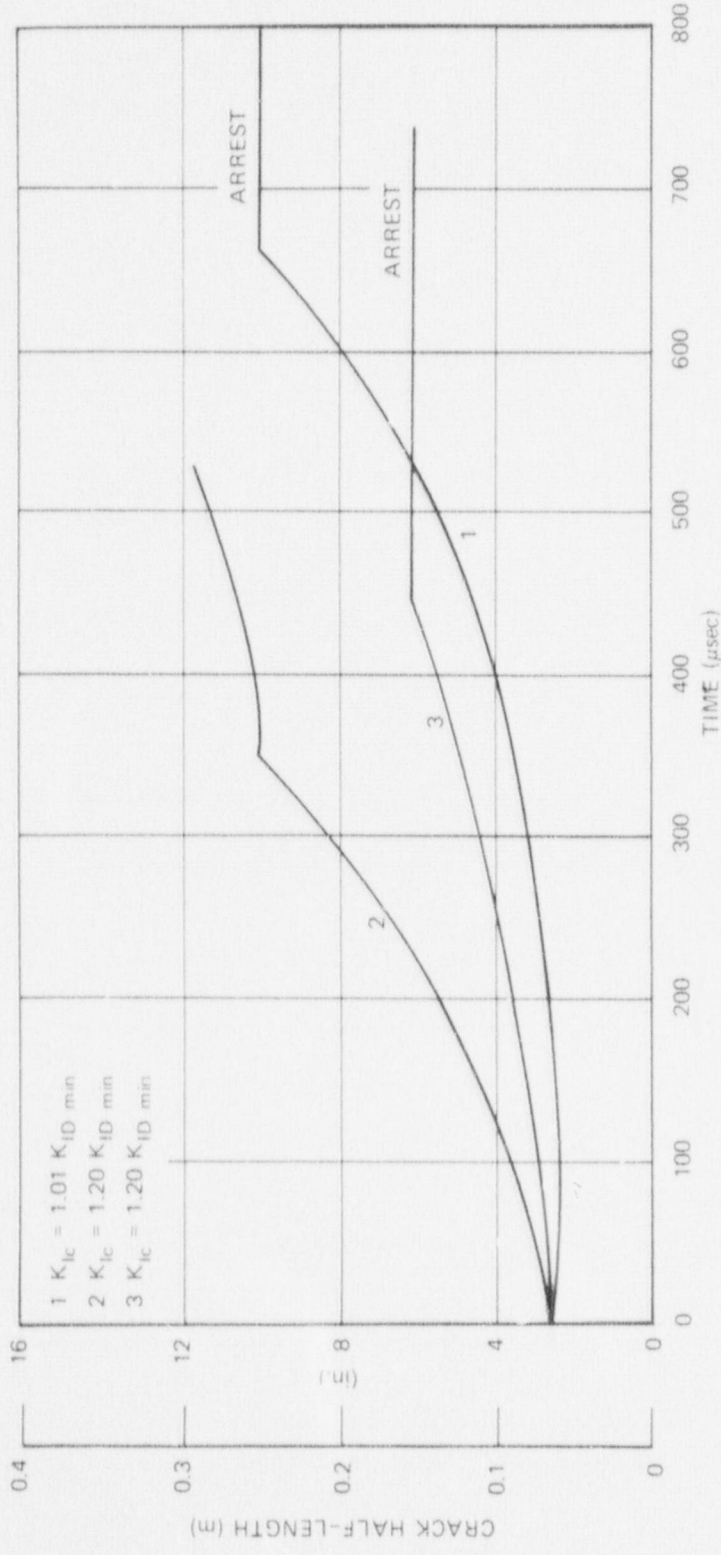

Fig. A.11. Crack half-length vs time.

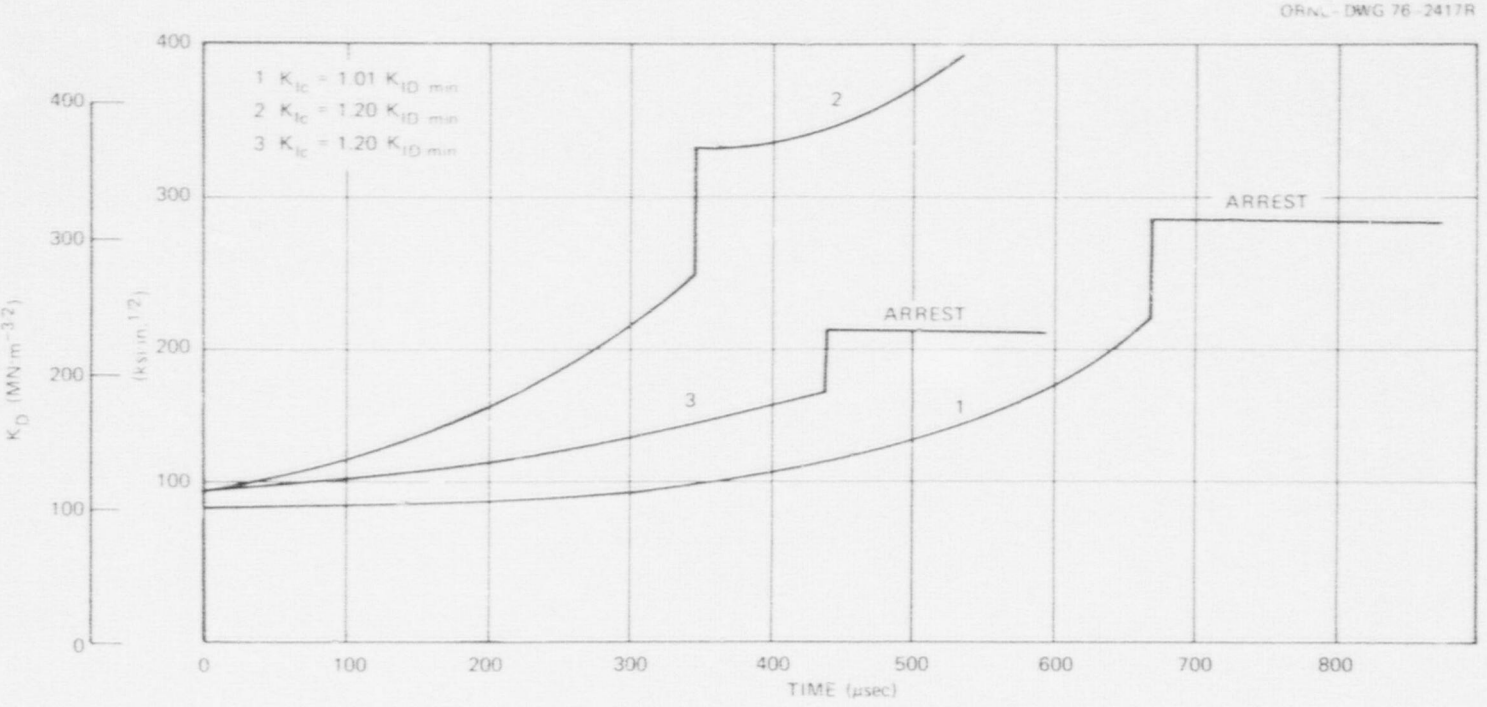

Fig. A.12. Dynamic stress-intensity factor vs time.

crack arrests, the dynamic stress-intensity factor becomes a constant and is, in fact, equal to the static stress-intensity factor. Studies are presently under way to assess the extent of possible postarrest variation of the stress-intensity factor with time, which is not predicted by the proposed model. The work by Sih et al.[45] suggests that there could be at least some damped oscillation. On the other hand, Freund[33] presents the argument that, in some circumstances, no variation in the stress-intensity factor after arrest should be expected.

The model used to analyze the three sample problems discussed here is quite versatile and can be used to gain information relating to a wide variety of problems. It is, however, based upon hypotheses which, although reasonable, have yet to be experimentally verified. In addition, the model depends on a dynamic characterization of the material of interest (i.e., a K_{ID} vs $\dot{a}$ curve). To date, such a characterization exists only for a polymer. Thus, while the approach proposed here appears to have considerable potential, considerable development work is still required for measuring material properties and determining the validity of the basic assumptions.

Appendix B

DYNAMIC FINITE-ELEMENT INVESTIGATION OF A CRACK PROPAGATING IN A CRACK-ARREST MODEL

This appendix describes a dynamic finite-element analysis of a right circular cylinder loaded by internal pressure and containing a long axial crack that begins to propagate in one direction for a specified distance and then abruptly arrests. The radii of the cylinder, the initial crack length, and the arrested crack length were chosen to be representative of the crack-arrest models.

The plane of the crack forms a plane of symmetry for the cylinder; thus, only half of the cylinder had to be included in the finite-element analysis. The elastic and mass properties used for the finite-element analysis were for A533 steel. The finite-element grid used for this work is shown in Fig. B.1. This finite-element model consists of 105 sixteen-node isoparametric bricks and 54 very stiff, massless, bars. The bars are

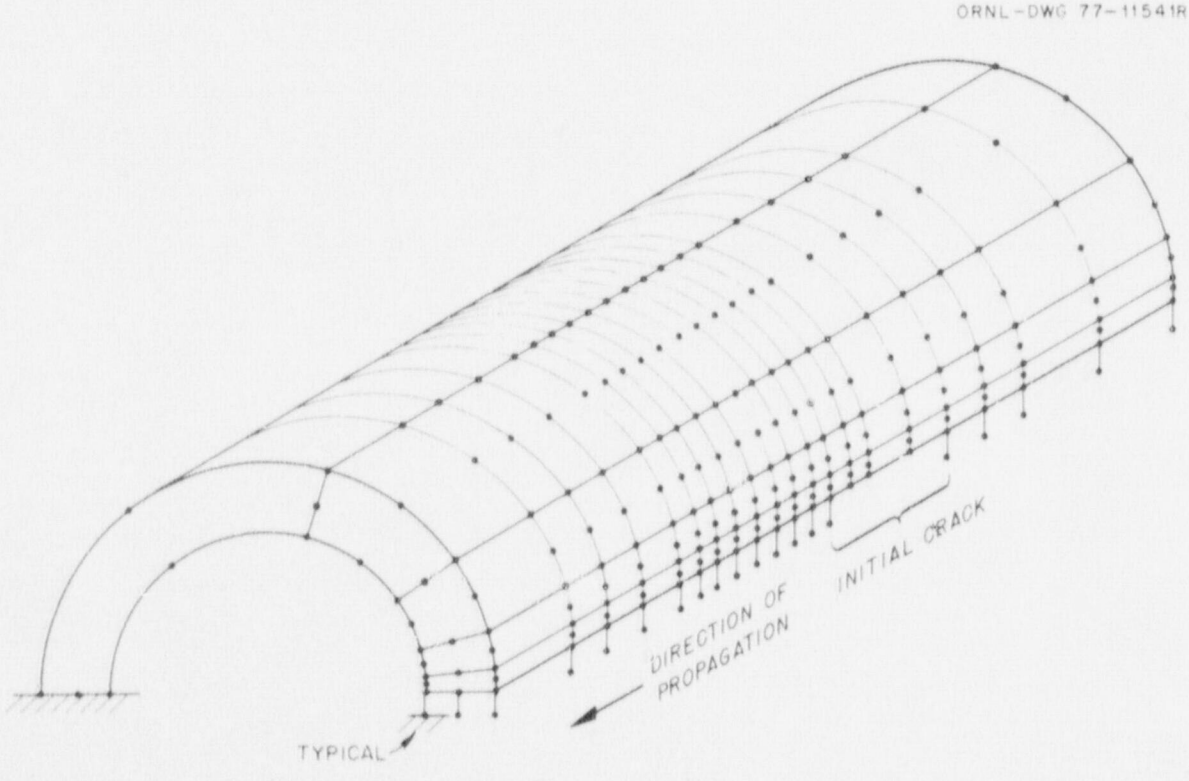

Fig. B.1 Finite-element grid used to study the effect of velocity on the dynamic stress-intensity factor during crack propagation and after arrest.

normal to the plane of the crack and thus enforce negligible displacement. Eighteen of the bars break in sequential order and at prescribed times corresponding to the imposed crack-front velocity.

The breaking of the bars was accomplished by making the stiffness of the bars time dependent. Until a bar breaks, its stiffness is very large, then, at the instant the bar is to break, its stiffness becomes zero, and the stiffness matrix for the structure is re-formed. For convenience, 90 time integration intervals were used for each of the three problems, and crack extension (i.e., the breaking of a row of three bars) occurred every 10th interval at six different times. The end caps were not included in the finite-element model. However, axial loads consistent with the internal pressure of the vessel were applied to the ends of the model. The vessel behavior was assumed to be linear elastic.

The time integration intervals were taken to be 0.64, 1.27, and 1.90 μsec, which correspond to crack velocities of 500 m/sec (19,685 in./sec), 1000 m/sec (39,370 in./sec), and 1500 m/sec (59,055 in./sec).

The displacement-basis method of calculating stress-intensity factors (i.e., relating the stress-intensity factor to the near-tip crack-opening displacement) was used for the present work. The displacements of the three nodes through the vessel wall and closest to the crack front were averaged in this calculation. The expression relating stress-intensity factor, K_I, to the nodal displacement, u, is given by

$$K_I = \frac{E}{1 - \nu^2} \frac{u}{\sqrt{r}} , \qquad (B.1)$$

where E and ν are Young's modulus and Poisson's ratio, respectively, and r is the distance from the crack tip to the node where the displacement is occurring.

For all the results reported here, the initial flaw was assumed to be 76.2 mm long (3.0 in.), and it was assumed to propagate from a single crack front with one of three constant crack-front velocities for a distance of 76.2 mm (3.0 in.), at which point it abruptly arrested. Results are also presented for the postarrest stress-intensity factor.

The stress-intensity factor normalized by the vessel internal pressure, which was assumed to be constant during crack propagation (variable pressure can be handled), is shown in Fig. B.2 for three crack-front velocities as a function of time normalized by the time integration step size, Δt. For the first 60 time steps, the crack front is propagating with a constant crack velocity indicated by the symbols in Fig. B.2 as the crack grows from 76.2 mm (3.0 in.) to 152.4 mm (6.0 in.). For the 30 time steps after the abrupt arrest, the crack length is constant, but the stress-intensity factor continues to vary as a function of time. The results indicate that the effect of crack velocity is quite large for the range of crack-front velocities expected during unstable crack extension in the crack-arrest models. The figure also shows that the stress-inter cy

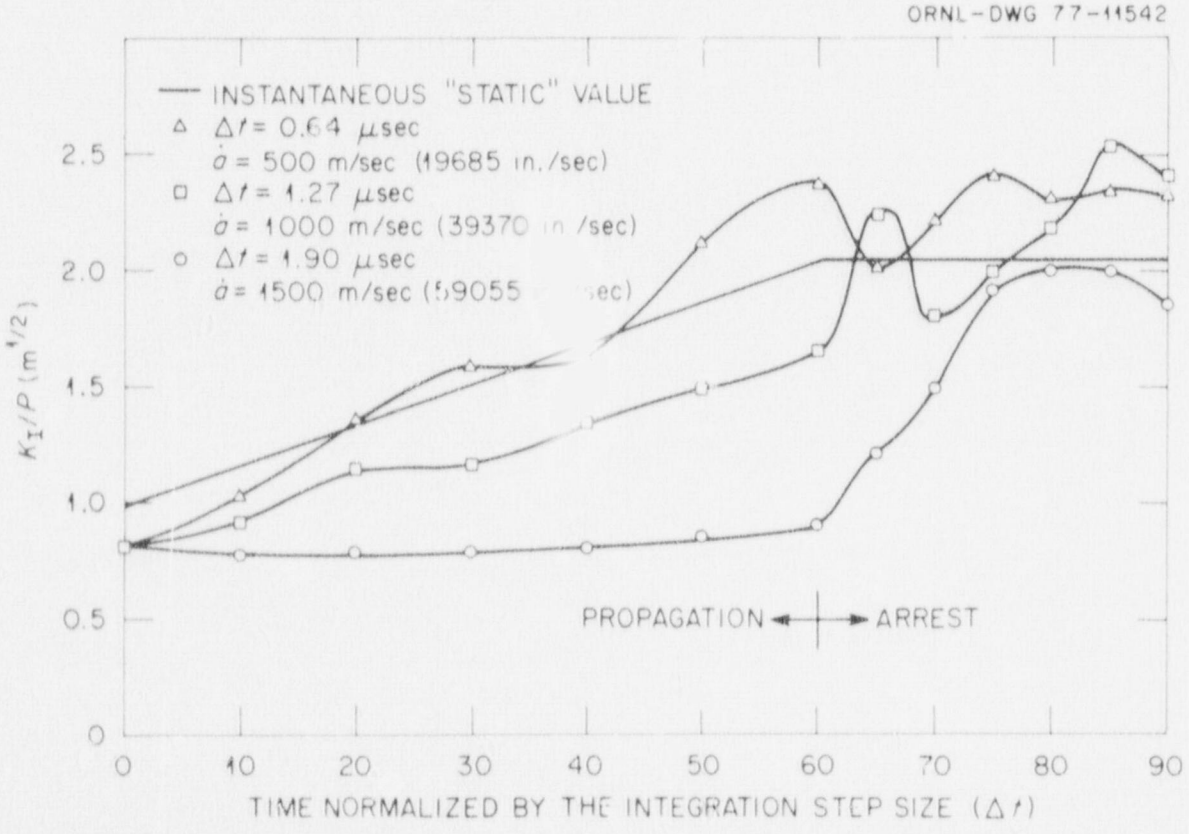

Fig. B.2. Dynamic stress-intensity factor K_I normalized by the crack-arrest model internal pressure plotted vs the number of time integration steps (time normalized by step size, Δt) for three imposed crack velocities, $\dot{a}$.

factor tends to decrease with increased velocities for a given crack length, as predicted by the simplified method discussed in Appendix A. Finally, the results shown in Fig. B.2 indicate that the postarrest stress-intensity factor can exhibit an overshoot of ~25%, which is about that predicted by Sih, Embley, and Ravera[45] in their exact solution of a suddenly appearing crack in an infinite solid.

Appendix C

MATERIAL PROPERTIES

This appendix presents (1) information on material properties in tabular form and (2) figures that permit one to locate the individual specimens in the bulk source materials and to determine both the raw data and calculated results from these specimens. A brief outline of the calculation methods used to reduce the static and dynamic fracture toughness data obtained from precracked Charpy specimens is also presented.

The Charpy V-notch specimen data and results for all material conditions are listed in Table C.1. Orientation and depth notations have been described in Chapter 5.

The static fracture toughness (K_{Icd}) data are listed in Table C.2. Specimen deflection was measured by deflectometers attached directly to the specimen. Displacement for all tests was 2.54 mm/min (0.100 in./min). All calculations for K_{Icd} were made in accordance with the expression given in ASTM E-399-74 for bend specimens,[18] with the load P_Q being given the value P_{EE} prescribed by the equivalent energy method developed by Witt and Mager,[47,48]

$$P_{EE} = \sqrt{2mE}_{max} \quad , \tag{C.1}$$

where m is the slope of the linear portion of the load-deflection curve and E_{max} is the area under the curve up to maximum load. The dimensional parameters shown in Tables C.2 and C.3 are defined in ASTM E-399-74. The function $f\left(\frac{a}{W}\right)$ was calculated from the expression,

$$f\left(\frac{a}{W}\right) = \left(1 - \frac{a}{W}\right)^{-1/2} \quad , \tag{C.2}$$

for a square beam rather than the series for a rectangular beam recommended in ASTM E-399-74. All load and deflection data were obtained from the load-displacement record.

The dynamic fracture toughness (K_{Idd}) data and results are listed in Table C.3 for an input energy of 34 J (25 ft-lb) or a contact velocity (v_0) of 1.7 m/sec (5.5 fps). Dynamic fracture toughness values were calculated by the equivalent energy procedure, with corrections made for machine compliance and hammer velocity.[49] The dynamic "J" integral (J_{Id}) was calculated from the expression,

$$J_{Id} = \frac{2.2\ \overline{\Delta E}_m}{\phi B} , \qquad (C.3)$$

where $\overline{\Delta E}_m$ is the energy absorbed by deformation of the specimen up to maximum load, corrected for machine compliance. The dimensional parameters b and B correspond to the remaining ligament below the fatigued crack and the thickness of the specimen, respectively. The dynamic fracture toughness was calculated from the "J" integral (K_{Jd}) using the expression,

$$K_{Jd} = (E\ J_{Id})^{1/2} , \qquad (C.4)$$

where E is the elastic modulus of the specimen material.

The drop weight data are listed in Table C.4 and were determined in accordance with ASTM E-208-69.[20]

The specimen number may be used to determine the location of each specimen in the original plate section. Tables C.5 to C.8 locate the slab number and location of the specimen strip in the slab shown in Figs. C.1 through C.3 and the location of the specimens in the specimen strip from the appropriate cutting scheme and specimen position shown in Fig. C.4.

Table C.1. Charpy impact data from base plate W57 and plates AQ 03JZ and AQ 04BE

(Conversion factors: 1 ft-lb = 1.36 J; 1 mil = 0.0254 mm)

Specimen No.	Depth t	Depth T	Specimen orientation	Test temperature [°C (°F)]	Total energy (ft-lb)	Lateral expansion (mils)	Fracture appearance (% fibrous)
				As-received W57 base plate			
57V 17		0.5	RT	-17.8 (0)	40	31	20
57V 18		0.6	RT	149 (300)	127.5	83	100
57V 19		0.7	RT	37.8 (100)	126	83	100
57V 20		0.3	RT	10.0 (50)	65	47	35
57V 21		0.4	RT	204 (400)	127	77	100
57V 22		0.5	RT	93.3 (200)	127	85	100
57V 23		0.6	RT	23.9 (75)	102	72	65
57V 24		0.7	RT	-45.6 (-50)	16	12	8
57V 25		0.8	RT	-73.3 (-100)	8	4	0
57V 39		0.7	WT	93.3 (200)	113.5	79	100
57V 40		0.3	WT	23.9 (75)	89	63	65
57V 41		0.4	WT	-17.8 (0)	33	27	20
57V 42		0.5	WT	204 (400)	108.5	66	100
57V 43		0.6	WT	-45.6 (-50)	23.5	19	5
57V 44		0.7	WT	-73.3 (-100)	4	3	0
				Plate AQ 03JZ (quenched only)			
03JZ 18	0.7	0.6	RT	51.7 (125)	25	9	
03JZ 19	0.7	0.7	RT	10.0 (50)	16	13	
03JZ 20	0.7	0.8	RT	121 (250)	24	6	
03JZ 28	0.7	0.2	RT	-45.6 (-50)	7.5	0	
03JZ 29	0.7	0.3	RT	-73.3 (-100)	7	5	
03JZ 30	0.7	0.4	RT	93.3 (200)	33	15	
03JZ 31	0.7	0.5	RT	37.8 (100)	19.5	7	
03JZ 32	0.7	0.6	RT	-17.8 (0)	14	3	
03JZ 33	0.7	0.7	RT	149 (300)	24	10	

Table C.1 (continued)

Specimen No.	Depth		Specimen orientation	Test temperature [°C (°F)]	Total energy (ft-lb)	Lateral expansion (mils)	Fracture appearance (% fibrous)
	t	T					
			Plate AQ 03JZ (quenched only)				
03JZ 34	0.7	0.8	RT	204 (400)	23	8	
03JZ 36	0.3	0.3	WT	37.8 (100)	21	7	
03JZ 37	0.3	0.4	WT	93.3 (200)	29	9	
03JZ 39	0.3	0.6	WT	149 (300)	30.5	12	
			Tempered plate AQ 03JZ (2 hr at 1200°F, air cooled)				
03JZ 61	0.3	0.2	RT	10.0 (50)	104	69	
03JZ 62	0.3	0.2	RT	65.6 (150)	104	59	
03JZ 63	0.7	0.2	RT	-73.3 (-100)	92	58	
03JZ 64	0.7	0.2	RT	-129 (-200)	25.5	13	
			Reaustenitized plate AQ 03JZ (1 hr at 1600°F; cooling rate, 0.91°R/sec)[a]				
03JZ 49	0.3	0.1	RT	-17.8 (0)	10	3	
03JZ 50	0.3	0.1	RT	37.8 (100)	37	27	
03JZ 51	0.3	0.2	RT	93.3 (200)	78	60	
03JZ 52	0.3	0.2	RT	149 (300)	92.5	68	
03JZ 53	0.3	0.3	RT	204 (400)	90	63	
03JZ 54	0.3	0.3	RT	-73.3 (-100)	4	0	
03JZ 55	0.3	0.4	RT	65.6 (150)	44	31	
03JZ 56	0.3	0.4	RT	10.0 (50)	18.5	13	
			Reaustenitized plate AQ 03JZ (1 hr at 1600°F; cooling rate, 1.6°R/sec)[a]				
03JZ 65	0.7	0.1	RT	93.3 (200)	85.5	65	
03JZ 66	0.7	0.1	RT	37.8 (100)	35	29	
03JZ 67	0.7	0.2	RT	65.6 (150)	57	44	
03JZ 68	0.7	0.2	RT	-17.8 (0)	13.5	7	
03JZ 69	0.7	0.3	RT	204 (400)	88	61	
03JZ 70	0.7	0.3	RT	149 (300)	85	60	

Table C.1 (continued)

Specimen No.	Depth t	Depth T	Specimen orientation	Test temperature [°C (°F)]	Total energy (ft-lb)	Lateral expansion (mils)	Fracture appearance (% fibrous)
Reaustenitized plate AQ 03JZ (1 hr at 1600°F; cooling rate, 17.0°R/sec)[a]							
03JZ 77	0.3	0.7	RT	93.3 (200)	27	11	
03JZ 79	0.3	0.8	RT	10.0 (50)	10.5	2	
03JZ 81	0.3	0.9	RT	204 (400)	30.5	13	
Plate AQ 04BE (quenched only)							
04BE 11	0.3	0.5	WT	-73.3 (-100)	7.5	0	
04BE 12	0.3	0.6	WT	-17.8 (0)	10.5	2	
04BE 13	0.3	0.7	WT	37.8 (100)	17	5	
04BE 14	0.3	0.8	WT	93.3 (200)	21.5	9	
04BE 15	0.7	0.2	WT	204 (400)	31.5	14	
04BE 16	0.7	0.3	WT	149 (300)	21.5	5	

[a]Heat treatment done in DATA TRAK.

Table C.2. Precracked Charpy V stat

(Conversion factors

Specimen No.	Depth t	Depth T	Specimen orientation	Test temperature [°C (°F)]	K_{Icd} [MN·m$^{-3/2}$ (ksi·in.$^{1/2}$)]	(i
57V 5		0.3	RT	37.8 (100)	261 (237)	0.
57V 6		0.4	RT	93.3 (200)	225 (205)	0.
57V 7		0.5	RT	149 (300)	218 (198)	0.
57V 8		0.6	RT	-17.0 (0)	280 (255)	0.
57V 9		0.7	RT	-73.3 (-100)	87 (79)	0.
57V 10		0.3	RT	-45.6 (-50)	164 (149)	0.
57V 35		0.3	WT	93.3 (200)	180 (164)	0.
57V 36		0.4	WT	-17.0 (0)	251 (228)	0.
03JZ 21	0.3	0.2	RT	10.0 (50)	115 (105)	0.
03JZ 22	0.3	0.3	RT	-17.0 (0)	115 (105)	0.
03JZ 23	0.3	0.4	RT	-73.3 (-100)	86 (78)	0.
03JZ 24	0.3	0.5	RT	-129 (-200)	65 (59)	0.
03JZ 25	0.3	0.6	RT	93.3 (200)	99 (90)	0.
03JZ 26	0.3	0.7	RT	204 (400)	77 (70)	0.
03JZ 27	0.3	0.8	RT	-73.3 (-100)	78 (71)	0.
03JZ 42	0.7	0.2	WT	-73.3 (-100)	84 (76)	0.
03JZ 43	0.7	0.3	WT	18.9 (66)	130 (118)	0.
03JZ 44	0.7	0.4	WT	93.3 (200)	113 (103)	0.
					Reaustenitized plate	
03JZ 57	0.3	0.5	RT	-17.0 (0)	81 (74)	0.
03JZ 58	0.3	0.5	RT	-73.7 (-100)	41 (37)	0.
03JZ 59	0.3	0.6	RT	37.8 (100)	131 (119)	0.
03JZ 60	0.3	0.6	RT	149 (300)	179 (163)	0.
					Reaustenitized plate	
03JZ 71	0.7	0.4	RT	-73.3 (-100)	47 (43)	0.
03JZ 72	0.7	0.4	RT	-17.0 (0)	76 (69)	0.
03JZ 73	0.7	0.5	RT	37.8 (100)	157 (143)	0.
03JZ 74	0.7	0.5	RT	93.3 (200)	196 (178)	0.
03JZ 75	0.7	0.6	RT	10.0 (50)	85 (77)	0.
03JZ 76	0.7	0.6	RT	149 (300)	188 (171)	0.
					Reaustenitized plate	
03JZ 78	0.3	0.7	RT	-73.3 (-100)	63 (57)	0.
03JZ 80	0.3	0.8	RT	149 (300)	95 (86)	0.
03JZ 82	0.3	0.9	RT	-17.0 (0)	82 (75)	0.
04BE 1	0.7	0.2	WT	18.9 (66)	107 (97)	0.
04BE 2	0.7	0.3	WT	-3.9 (25)	104 (95)	0.
04BE 3	0.7	0.4	WT	-3.9 (25)	87 (79)	0.
04BE 4	0.7	0.5	WT	-17.0 (0)	78 (71)	0.
04BE 5	0.7	0.6	WT	-45.6 (-50)	88 (80)	0.
04BE 6	0.7	0.7	WT	93.3 (200)	102 (93)	0.
04BE 7	0.7	0.8	WT	149 (300)	92 (84)	0.
04BE 8	0.3	0.2	WT	37.8 (100)	102 (93)	0.
04BE 9	0.3	0.3	WT	-45.6 (-50)	86 (78)	0.
04BE 10	0.3	0.4	WT	-101 (-150)	58 (53)	0.

[a]Heat treatment done in DATA TRAK.

ic fracture toughness of base plate W57 and plates AQ 03JZ and AQ 048E

1 in. = 25.4 mm; 1 lb = 0.454 kg; 1 ft-lb = 1.36 J)

Average crack data				Load (lb)			Deflection (in.)		Energy (ft-lb)		Slope of linear load-displacement curve (10^4 lb/in.)
a (in.)	b (in.)	a/W	f(a/W)	Maximum	Start of fracture	Fracture arrest	Maximum load	Start of fracture	Maximum load	Start of fracture	
As-received W57 base plate											
213	0.180	0.542	3.23	1220			0.079		6.8		12.5
214	0.180	0.542	3.22	1170			0.067		5.4		11.9
228	0.166	0.578	3.55	975			0.062		4.2		11.1
205	0.189	0.521	3.02	1410			0.079		7.9		14.4
208	0.186	0.529	3.09		1030	300		0.015		1.0	10.7
211	0.183	0.536	3.16		1170	490		0.035		2.7	13.1
213	0.181	0.541	3.22	1150			0.072		5.9		6.9
218	0.176	0.554	3.36	1210			0.065		5.5		13.3
Plate AQ 03JZ (quenched only)											
216	0.177	0.550	3.31		1650	1560		0.015		1.2	13.8
207	0.186	0.527	3.07		1600	1570		0.015		1.2	15.3
214	0.179	0.545	3.25		1270	980		0.011		0.7	13.4
217	0.177	0.551	3.32		980	320		0.008		0.3	14.4
214	0.180	0.543	3.24		1450	1430		0.012		0.9	14.2
215	0.179	0.545	3.26	1190			0.009		0.5		14.0
203	0.190	0.517	2.98		1300	830		0.010		0.6	14.4
205	0.189	0.521	3.02		1420	1000		0.010		0.6	15.6
211	0.183	0.535	3.15		1675	1655				1.7	9.2
211	0.183	0.536	3.16		1650	1475		0.015		1.2	14.6
AQ 03JZ (1 hr at 1600°F; cooling rate, 0.91°R/sec)[a]											
199	0.195	0.504	2.87		1275	975		0.012		0.7	14.7
199	0.196	0.504	2.86		800	715		0.007		0.2	10.8
199	0.194	0.507	2.89	1525	1440	1000	0.018	0.034	1.6		16.4
197	0.196	0.501	2.83	1750			0.290		3.2		16.1
AQ 03JZ (1 hr at 1600°F; cooling rate, 1.6°R/sec)[a]											
201	0.192	0.511	2.92		890	830		0.007		0.3	11.9
208	0.186	0.528	3.08		1100	1000		0.010		0.6	13.8
207	0.188	0.524	3.05		1535	1480		0.026		2.5	13.8
212	0.183	0.536	3.17	1635			0.035		3.7		13.8
205	0.190	0.519	3.00		1335	1260		0.011	0.7		14.8
204	0.190	0.517	2.98	1820			0.030		3.3		15.8
AQ 03JZ (1 hr at 1600°F; cooling rate, 17.0°R/sec)[a]											
186	0.199	0.483	2.69		1175	1150		0.009		0.5	14.0
206	0.187	0.524	3.04	1415			0.012		0.8		14.1
198	0.196	0.503	2.85		1440	1375		0.011		0.7	15.0
Plate AQ 048E (quenched only)											
193	0.201	0.490	2.75	1850			0.016		1.4		14.0
194	0.192	0.493	2.77	1900			0.012		1.0		17.7
184	0.290	0.467	2.57	1660			0.010		0.8		18.3
214	0.181	0.542	3.23	1190			0.013		0.7		10.9
178	0.214	0.453	2.47	1690			0.012		1.0		17.3
184	0.210	0.467	2.57	1790			0.013		1.2		17.7
183	0.210	0.466	2.57	1730			0.011		0.9		18.4
193	0.201	0.488	2.73	1775			0.013		1.1		17.2
182	0.211	0.464	2.55		1730	1000		0.010		0.8	18.9
196	0.198	0.498	2.82		1225	500		0.008		0.4	12.7

Table C.3. Precracked Charpy V dynamics fracture toughness of base plate W57 and plates AQ 03JZ and AQ 04BE

(Conversion factors: 1 in. = 25.4 mm ; 1 ksi·in.$^{1/2}$ = 1.10 MN·m$^{-3/2}$)

Specimen No.	Depth t	Depth a	Specimen orientation	Test temperature [°C (°F)]	K_{Icd} (ksi·in.$^{1/2}$)	J_{Id} (in.-lb/in.^{2})	K_{JD} (ksi·in.$^{1/2}$)	Average crack data a (in.)	b (in.)	a/W	f(a/w)
Plate AQ 03JZ (quenched only)											
03JZ 8	0.3	0.3	RT	20.0 (68)	116	448	116	0.194	0.199	0.493	2.77
03JZ 9	0.3	0.4	RT	65.6 (150)	124	521	125	0.213	0.181	0.541	3.22
03JZ 11	0.3	0.6	RT	-17.8 (0)	110	404	110	0.191	0.203	0.484	2.70
03JZ 12	0.3	0.7	RT	-45.6 (-50)	91	274	91	0.187	0.207	0.476	2.63
03JZ 13	0.3	0.8	RT	-73.3 (-100)	76	191	76	0.191	0.202	0.486	2.71
03JZ 15	0.7	0.3	RT	-101 (-150)	79	206	79	0.201	0.193	0.511	2.92
03JZ 45			WT	-101 (-150)	67	152	67	0.212	0.182	0.538	3.18
03JZ 46			WT	-45.6 (-50)	67	151	67	0.208	0.185	0.529	3.10
03JZ 47			WT	20.0 (68)	117	456	117	0.207	0.187	0.526	3.06
03JZ 48			WT	65.6 (150)	102	347	102	0.215	0.179	0.545	3.26
Plate AQ 04BE (quenched only)											
04BE 17	0.7	0.4	WT	20.0 (68)	112	418	112	0.208	0.186	0.528	3.08
04BE 19	0.7	0.6	WT	65.6 (150)	100	333	100	0.188	0.204	0.479	2.66
04BE 20	0.7	0.7	WT	-17.8 (0)	99	326	99	0.182	0.212	0.463	2.54
04BE 21	0.7	0.8	WT	-73.3 (-100)	72	174	72	0.185	0.208	0.471	2.60
As-received W57 base plate											
057V 11		0.4	RT	93.3 (200)	335	3650	331	0.209	0.186	0.530	3.10
057V 12		0.5	RT	37.8 (100)	337	3650	331	0.212	0.181	0.540	3.21
057V 13		0.6	RT	-17.8 (0)	62	126	62	0.217	0.175	0.553	3.35
057V 14		0.7	RT	10.0 (50)	160	835	158	0.220	0.174	0.559	3.41
057V 15		0.3	RT	23.9 (75)	292	2780	289	0.218	0.176	0.554	3.35
057V 16		0.4	RT	149 (300)	345	3860	340	0.213	0.181	0.540	3.21
057V 26		0.4	RT	-45.6 (-50)	60	121	60	0.194	0.200	0.493	2.77
057V 27		0.5	RT	-73.3 (-100)	61	123	61	0.182	0.212	0.462	2.53
057V 37		0.5	WT	10.0 (50)	186	1120	184	0.221	0.174	0.559	3.42
057V 38		0.6	WT	93.3 (200)	300	2960	298	0.215	0.180	0.545	3.25

Table C.4. Drop-weight data from W57 base plate

Specimen No.	Depth	Specimen orientation	Test temperature [°C (°F)]	Result of test[a]
57V57	1/4 T	RT	-17.8 (0)	NB
57V65	1/4 T	RT	-23.3 (-10)	NB
57V62	1/4 T	RT	-26.1 (-15)	NB
57V66	1/4 T	RT	-28.9 (-20)	B
57V61	1/4 T	RT	-31.7 (-25)	B
57V58	1/4 T	RT	-45.6 (-50)	B
57V64	3/4 T	RT	-23.3 (-10)	NB
57V63	3/4 T	RT	-26.1 (-15)	B
57V67	3/4 T	RT	-26.1 (-15)	B
57V68	3/4 T	RT	-26.1 (-15)	NB
57V60	3/4 T	RT	-31.7 (-25)	B
57V59	3/4 T	RT	-45.6 (-50)	B
57V69	1/4 T	WT	-26.1 (-15)	NB
57V71	1/4 T	WT	-28.9 (-20)	NB
57V73	1/4 T	WT	-34.4 (-30)	B
57V74	3/4 T	WT	-26.1 (-15)	NB
57V72	3/4 T	WT	-28.9 (-20)	B
57V70	3/4 T	WT	-31.7 (-25)	B

[a] B denotes break; NB denotes no break.

Table C.5. Specimen tabulation for base material from HSST submerged-arc weldment W57

Slab No.	Cutting scheme[a]	Specimen numbers for blank position				
		1	2	3	4	5
57V1A	A	57V1[b]				
57V1B	A	57V2[b]				
57V1C1	C	57V3[b]	57V4[b]			
57V1D1	D	57V5	57V6	57V7	57V8	57V9
57V1D2	D	57V10	57V11	57V12	57V13	57V14
57V2A	D	57V35	57V36	57V37	57V38	57V39
57V2B	D	57V40	57V41	57V42	57V43	57V44
57V2C	D	57V53[c]	57V54[c]	57V46	57V47	57V48
57V3A	D	57V15	57V16	57V17	57V18	57V19
57V3B	D	57V20	57V21	57V22	57V23	57V24
57V3C	D	57V25	57V26	57V27	57V28	57V29
57V3D	D	57V30	57V31	57V32	57V33	57V34
57V4A	D	57V49[c]	57V50[c]	57V51[c]	57V52[c]	57V45
57V4B	C	57V55[b]	57V56[b]			
57V5A	H	57V57	57V59			
57V5B	H	57V58	57V60			
57V6A	H	57V61	57V63			
57V6B	H	57V62	57V64			
57V7A	H	57V65	57V67			
57V7B	H	57V66	57V68			
57V8A	H	57V69	57V70			
57V9A	H	57V71	57V72			
57V10A	H	57V73	57V74			

[a] See Fig. A.4.

[b] Compact specimens.

[c] Subsize tensile specimens.

Table C.6. Specimen tabulation for HSST plate section 03JZ

Slab number	Cutting scheme[a]	Specimen numbers for blank position						
		1	2	3	4	5	6	7
03R1A	B	03JZ 1[b]	03JZ 2[b]					
03R1E1	E	03JZ 7[c]	03JZ 8	03JZ 9	03JZ 10[c]	03JZ 11	03JZ 12	03JZ 13
03R1B2	E	03JZ 14[c]	03JZ 15	03JZ 16	03JZ 17[c]	03JZ 18	03JZ 19	03JZ 20
03R2A1	C	03JZ 3[b]	03JZ 5[b]					
03R2A2	C	03JZ 4[b]	03JZ 6[b]					
03R1D1	E	03JZ 21	03JZ 22	03JZ 23	03JZ 24	03JZ 25	03JZ 26	03JZ 27
03R1D2	E	03JZ 28	03JZ 29	03JZ 30	03JZ 31	03JZ 32	03JZ 33	03JZ 34
03W1A1	E	03JZ 35[c]	03JZ 36	03JZ 37	03JZ 38[c]	03JZ 39	03JZ 40	03JZ 41
03W1A2	E	03JZ 42	03JZ 43	03JZ 44	03JZ 45	03JZ 46	03JZ 47	03JZ 48

[a] See Fig. A.4.

[b] Compact specimens.

[c] Subsize tensile specimens.

Table C.7. Specimen tabulation for HSST plate section 03JZ receiving DATA TRAK heat treatments

Slab number	Cutting scheme[a]	Bar number	Bar position	
			A	B
03R2B1	F	1	03JZ 49	03JZ 50
03R2B1	F	2	03JZ 51	03JZ 52
03R2B1	F	3	03JZ 53	03JZ 54
03R2B1	F	4	03JZ 55	03JZ 56
03R2B1	F	5	03JZ 57	03JZ 58
03R2B1	F	6	03JZ 59	03JZ 60
03R2B1	F	7	03JZ 77	03JZ 78
03R2B1	F	8	03JZ 79	03JZ 80
03R2B1	F	9	03JZ 81	03JZ 82
03R3A1	G	1		
03R3A1	G	2	03JZ 61	03JZ 62
03R3A1	G	3		
03R3A1	G	4		
03R2B2	F	1	03JZ 65	03JZ 66
03R2B2	F	2	03JZ 67	03JZ 68
03R2B2	F	3	03JZ 69	03JZ 70
03R2B2	F	4	03JZ 71	03JZ 72
03R2B2	F	5	03JZ 73	03JZ 74
03R2B2	F	6	03JZ 75[b]	03JZ 76
03R2B2	F	7	03JZ 83[b]	03JZ 84
03R2B2	F	8	03JZ 85[b]	03JZ 86
03R2B2	F	9	03JZ 87[b]	03JZ 88
03R3A2	G	1	03JZ 89[b]	03JZ 90
03R3A2	G	2	03JZ 91	03JZ 92
03R3A2	G	3	03JZ 63[b]	03JZ 64
03R3A2	G	4	03JZ 93[b]	03JZ 94

[a] See Fig. A.4.

[b] Subsize tensile specimens.

Table C.8. Specimen tabulation for HSST plate section 04BE

Part number	Cutting scheme[a]	Specimen numbers for blank position						
		1	2	3	4	5	6	7
04BEA1A	E	4BE1[b]	4BE2[b]	4BE3	4BE4	4BE5	4BE6	4BE7
04BEA1B	E	4BE8[b]	4BE9[b]	4BE10	4BE11	4BE12	4BE13	4BE14
04BEA2A	E	4BE15	4BE16	4BE17	4BE18	4BE19	4BE20	4BE21

[a] See Fig. A.4.

[b] Subsize tensile specimen (remainder Charpy V).

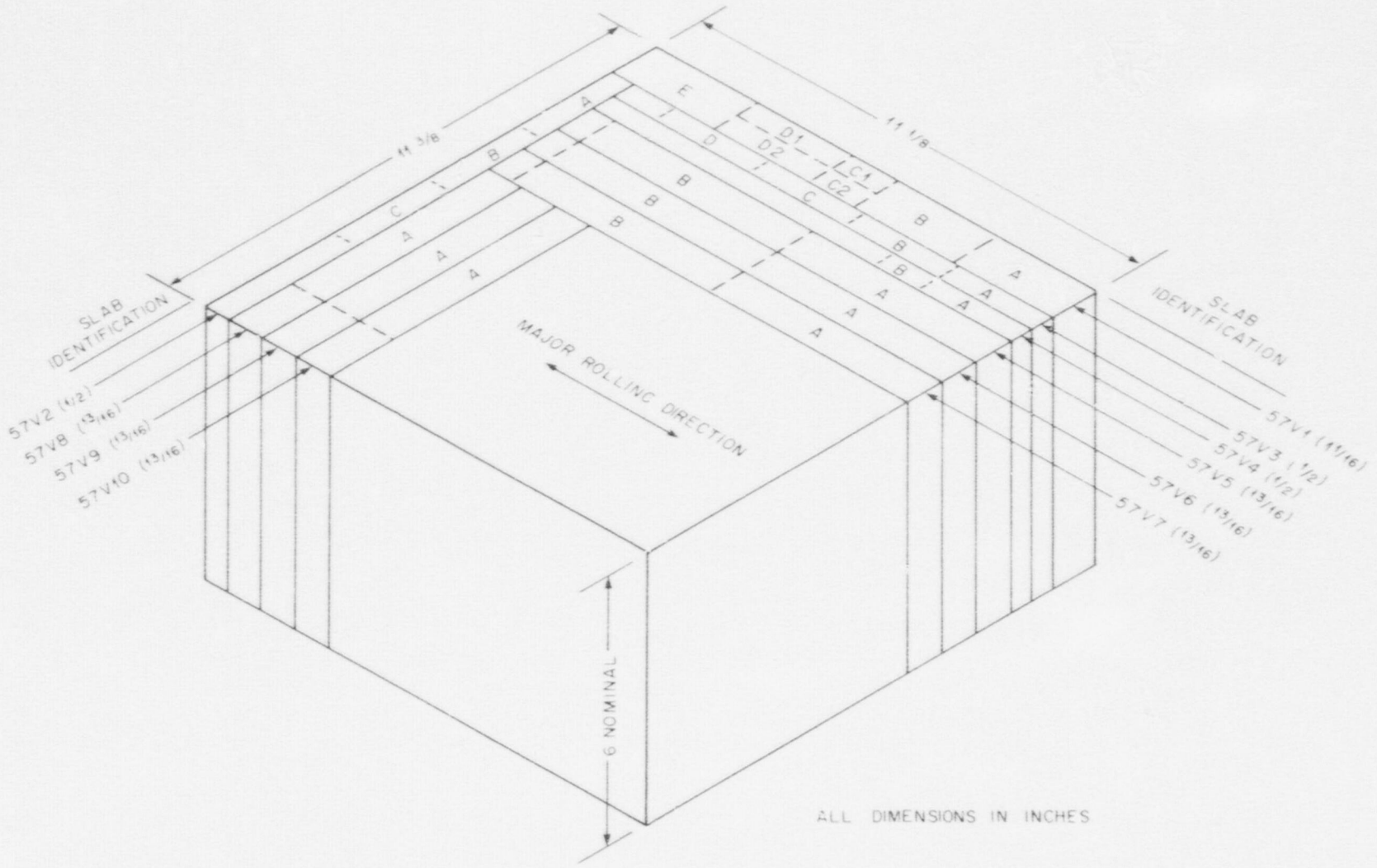

Fig. C.1. Cutting plan for base material from HSST submerged-arc weldment W57 (1 in. = 25.4 mm).

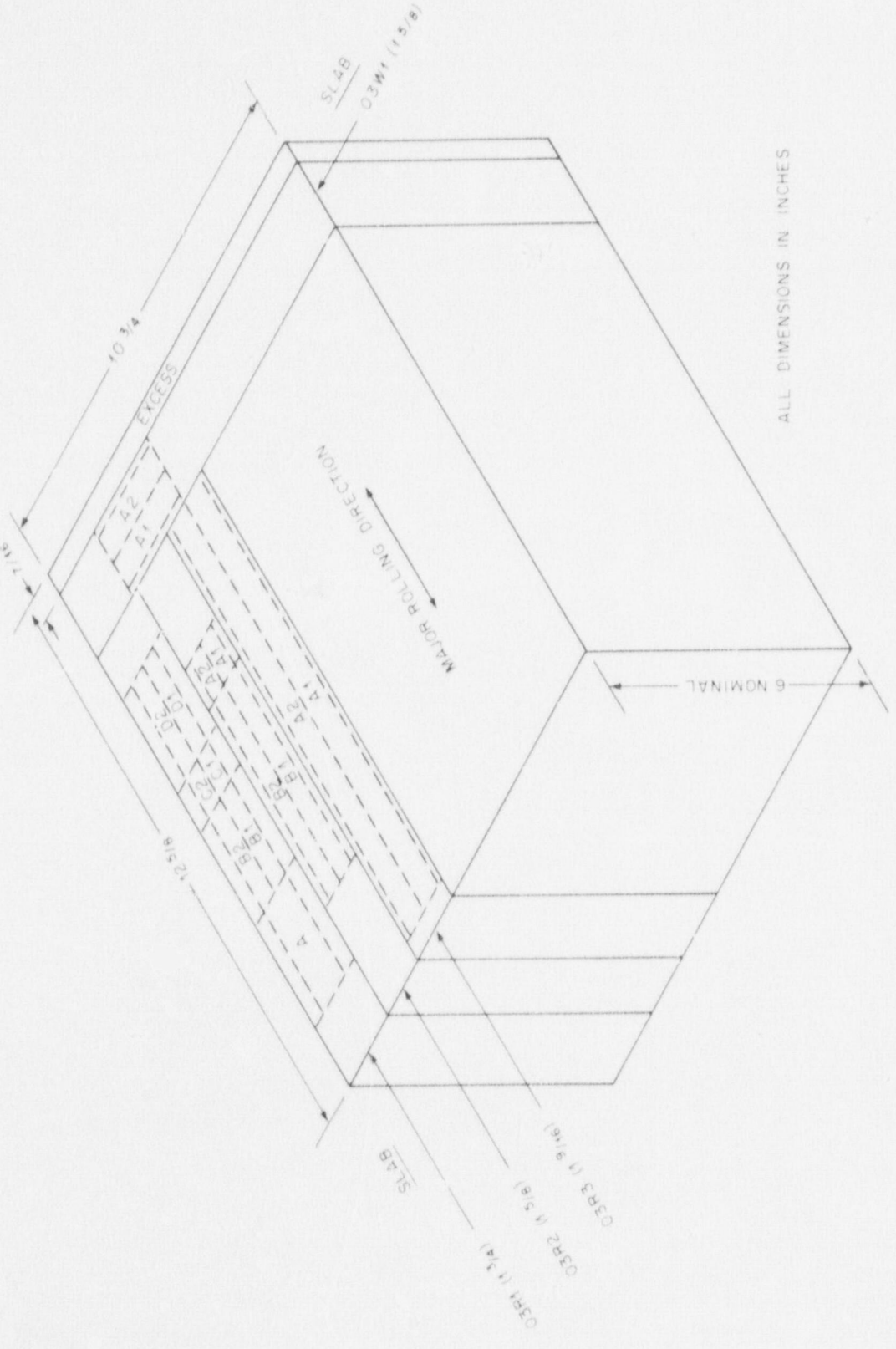

Fig. C.2. Cutting plan for HSST plate section 03JZ (1 in. = 25.4 mm).

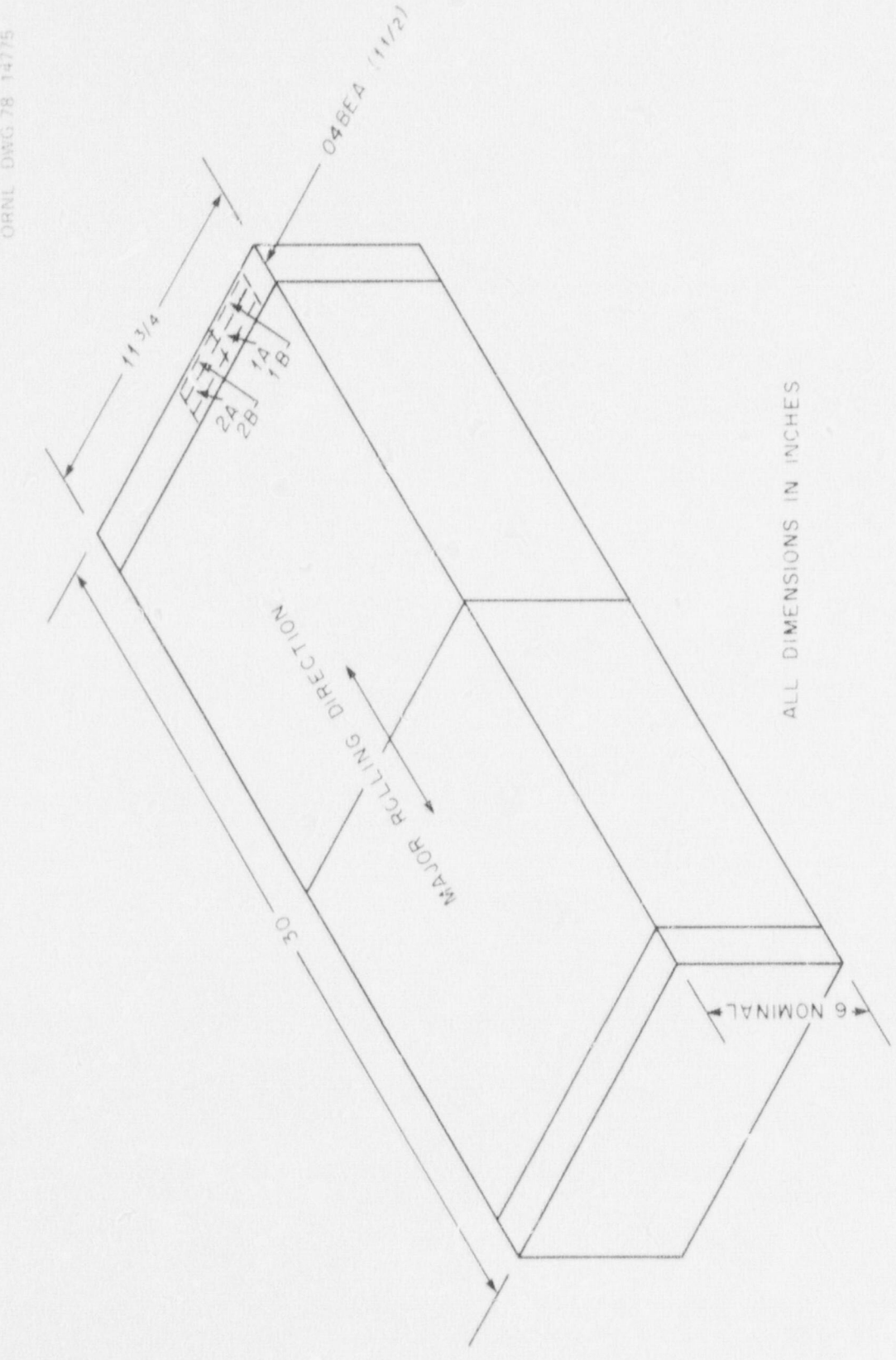

Fig. C.3. Cutting plan for HSST plate section C4BE (1 in. = 25.4 mm).

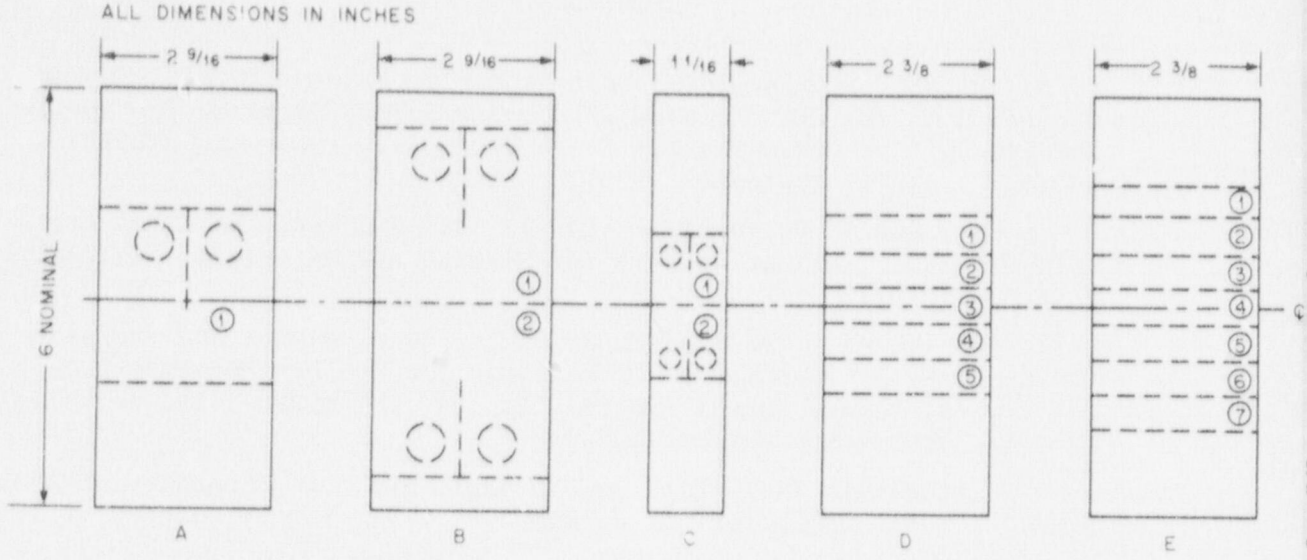

(a)

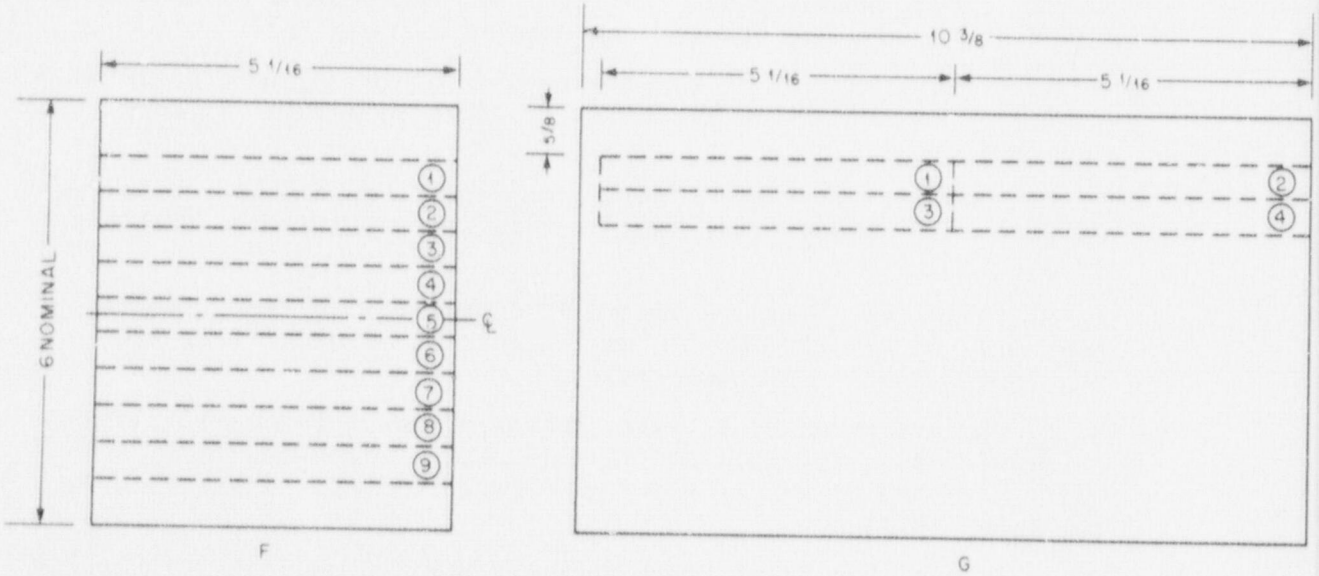

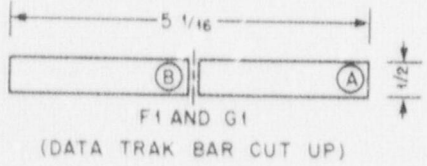

(b)

Fig. C.4. Specimen cutting schemes (1 in. = 25.4

ORNL-DWG 78-15181

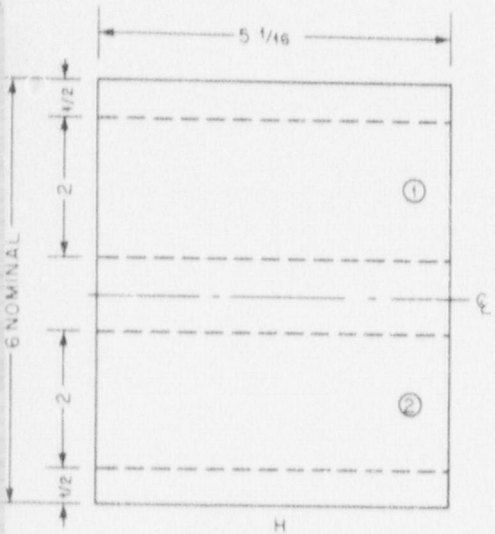

(P-2 DROP WEIGHT)

c)

REFERENCES

1. G. D. Whitman, *Quarterly Progress Report on Reactor Safety Programs Sponsored by the NRC Division of Reactor Safety Research for April–June 1975, II. Heavy-Section Steel Technology Program*, ORNL/TM-5021, pp. 14–15 (September 1975).

2. G. T. Hahn and M. F. Kanninen (Eds.), *Fast Fracture and Crack Arrest*, ASTM STP 627, American Society for Testing and Materials, Philadelphia, July 1977.

3. G. T. Hahn et al., *Critical Experiments, Measurements and Analyses to Establish a Crack Arrest Methodology for Nuclear Pressure Vessel Steels, Second Annual Progress Report*, BMI-NUREG-1959, Battelle Memorial Institute (October 1976).

4. P. B. Crosley and E. J. Ripling, "Dynamic Fracture Toughness of A533 Steel," *Trans. ASME, Ser. D, J. Basic Eng.* 91, 525–34 (September 1969).

5. J. F. Kalthoff, J. Beinert, and S. Winkler, "Measurements of Dynamic Stress Intensity Factors for Fast Running and Arresting Cracks in Double-Cantilever-Beam Specimens," pp. 161–76 in *Fast Fracture and Crack Arrest*, ASTM STP 627, ed. by G. T. Hahn and M. F. Kanninen, American Society for Testing and Materials, July 1977.

6. G. R. Irwin et al., *A Photoelastic Study of the Dynamic Fracture Behavior of Homalite 100*, NUREG-75/107, Nuclear Regulatory Commission (September 1975).

7. G. R. Irwin et al., *Photoelastic Studies of Crack Propagation and Crack Arrest*, NUREG-0342, Nuclear Regulatory Commission (October 1977).

8. R. D. Cheverton, *Pressure Vessel Fracture Studies Pertaining to a PWR LOCA-ECC Thermal Shock: Experiments TSE-1 and TSE-2*, ORNL/NUREG/TM-31 (September 1976).

9. R. D. Cheverton and S. E. Bolt, *Pressure Vessel Fracture Studies Pertaining to a PWR LOCA-ECC Thermal Shock: Experiments TSE-3 and TSE-4, and Update of TSE-1 and TSE-2 Analysis*, ORNL/NUREG-22 (December 1977).

10. E. S. Folias, "An Axial Crack in a Pressurized Cylindrical Shell," *Int. J. Fract. Mech.* 1, 104–113 (1965).

11. G. T. Hahn, M. Sarrate, and A. R. Rosenfield, "Criteria for Crack Extension in Cylindrical Pressure Vessels," *Int. J. Fract. Mech.* 5, 187–210 (1969).

12. R. W. Derby et al., *Test of 6-in.-Thick Pressure Vessels, Series 1: Intermediate Test Vessels V-1 and V-2*, ORNL-4895 (February 1974).

13. R. H. Bryan et al., *Test of 6-inch-Thick Pressure Vessels, Series 2: Intermediate Test Vessels V-3, V-4 and V-6*, ORNL-5059 (November 1975).

14. J. G. Merkle et al., *Test of 6-in.-Thick Pressure Vessels. Series 3: Intermediate Test Vessel V-7*, ORNL/NUREG-1 (August 1976).

15. American Society of Mechanical Engineers, *ASME Boiler and Pressure Vessel Code, Section III, Division 1, Subsection NA, Nuclear Power Plant Components*, 1974 edition, ASME, New York, 1974.

16. C. E. Childress, *Fabrication History of the Third and Fourth ASTM A533 Steel Plates of the Heavy Section Steel Technology Program*, ORNL-4313-2, pp. 2–34 (February 1970).

17. C. E. Childress, *Fabrication Procedures and Acceptance Data for ASTM A533 Welds and a 10-in.-Thick ASTM A543 Plate of the Heavy Section Steel Technology Program*, Documentary Report 3, ORNL-4313-3, pp. 64–80 (January 1971).

18. American Society for Testing and Materials, "Method of Test for Plane-Strain Fracture Toughness of Metallic Materials," ANSI/ASTM E-399-74, pp. 505–24, in *1977 Annual Book of ASTM Standards, Part 10: Metals – Mechanical, Fracture, and Corrosion Testing; Fatigue; Erosion; Effect of Temperature*, American Society for Testing and Materials, Philadelphia, July 1977.

19. J. G. Merkle and H. T. Corten, "A J Integral Analysis for the Compact Specimens, Considering Axial Force as Well as Bending Effects," *Trans. ASME, Ser. J, J. Pressure Vessel Technol.* 96, 286–92 (November 1974).

20. American Society for Testing and Materials, "Standard Method for Conducting Drop-Weight Test to Determine Nil-Ductility Transition Temperature of Ferritic Steels," ASTM E-208-69, pp. 363–82 in *1977 Annual Book of ASTM Standards, Part 10: Metals – Mechanical, Fracture, and Corrosion Testing; Fatigue; Erosion; Effect of Temperature*, American Society for Testing and Materials, Philadelphia, 1977.

21. R. Crouse and D. A. Canonico, "Metallographic Examinations of Crack Arrest Models," in *Heavy Section Steel Technology Program Quarterly Progress Report for April–June 1977*, ORNL/NUREC/TM-147, pp. 60–67 (December 1977).

22. J. Miklowitz, "Elastic Waves Created During Tensile Fracture – The Phenomenon of a Second Fracture," *J. Appl. Mech.* 20, 122–130 (1953).

23. F. J. Loss, R. A. Gray, and J. R. Hawthorne, *Significance of Warm Prestress to Crack Initiation During Thermal Shock*, NRL/NUREG Report 8165, Naval Research Laboratory (September 1977).

24. S. R. Rolfe and J. M. Barsom, *Fracture and Fatigue Control in Structures, Applications of Fracture Mechanics*, pp. 167–207, Prentice Hall, Inc., Englewood Cliffs, N.J., 1977.

25. R. H. Sailors and H. T. Corten, "Relationship Between Material Fracture Toughness Using Fracture Mechanics and Transition Temperature Tests," pp. 164–91 in *Fracture Toughness, Part II*, ASTM STP 514, American Society for Testing and Materials, Philadelphia, 1972.

26. J. M. Barsom and S. T. Rolfe, "Correlations Between K_{Ic} and Charpy V-Notch Test Results in the Transition Temperature Range," pp. 281–302 in *Impact Testing of Materials*, ASTM STP 466, American Society for Testing and Materials, Philadelphia, 1970.

27. B. Marandet and G. Sanz, "Evaluation of the Toughness of Thick Medium-Strength Steels by Using Linear Elastic Fracture Mechanics and Correlations Between K_{Ic} and Charpy V-Notch," pp. 72–95 in *Flaw Growth and Fracture*, ASTM STP 631, American Society for Testing and Materials, Philadelphia, 1977.

28. G. W. Parry and L. Lazzeri, "The Application of Fracture Mechanics to the Assessment of Failure of Cylindrical Pressure Vessels Under Yielding Conditions," *Eng. Fract. Mech.* 1, 519–37 (1969).

29. K. B. Broberg, "The Propagation of a Brittle Crack," *Ark. Fys.* 18(10), 159–92 (1960).

30. K. B. Broberg, "Discussion of Fracture from the Energy Point of View," pp. 125–51 in *Recent Progress in Applied Mechanics*, ed. by B. Broberg, J. Hult, and N. Fritthoif, Almquist and Wiksell, Stockholm, 1967.

31. G. C. Smith, "Dynamic Crack Investigations," in *HSST Quarterly Progress Report for July–September 1975*, ORNL/TM-5170, Vol. II, pp. 51–57.

32. L. B. Freund, "Crack Propagation in an Elastic Solid Subjected to General Loading – I. Constant Rate of Extension," *J. Mech. Phys. Solids* 20, 129–40 (1972).

33. L. B. Freund, "Crack Propagation in an Elastic Solid Subjected to General Loading – II. Non-Uniform Rate of Extension," *J. Mech. Phys. Solids* 20, 141–52 (1972).

34. L. B. Freund, "Crack Propagation in an Elastic Solid Subjected to General Loading – III. Stress Wave Loading," *J. Mech. Phys. Solids* 21, 47–61 (1973).

35. L. B. Freund, "Crack Propagation in an Elastic Solid Subjected to General Loading – IV. Obliquely Incident Stress Pulse," *J. Mech. Phys. Solids* 22, 137–46 (1974).

36. G. T. Hahn et al., "Critical Experiments, Measurements and Analyses to Establish a Crack Arrest Methodology for Nuclear Pressure Vessel Steels," in *First Annual Progress Report*, BMI-1937, Battelle Memorial Institute (August 1975).

37. R. D. Mindlin, "Waves and Vibrations in Isotropic, Elastic Plates," pp. 199–232 in *Structural Mechanics, Proceedings of the First Symposium on Naval Structural Mechanics*, ed. by J. N. Goodier and N. J. Hoff, Pergamon Press, New York, 1960.

38. J. Miklowitz, "The Propagation of Compressional Waves in a Dispersive Elastic Rod – Part I," *J. Appl. Mech.* 24, 231–39 (June 1957).

39. J. Miklowitz and C. R. Insewanger, "The Propagation of Compressional Waves in a Dispersive Rod – Part II, Experimental Results and Comparison with Theory," *J. Appl. Mech.* 24, 240–44 (June 1957).

40. J. Effis and J. M. Krafft, "A Comparison of the Initiation with the Rapid Propagation of a Crack in a Mild Steel Plate," *Trans. ASME, Ser. D, J. of Basic Eng.* 87, 257–63 (March 1965).

41. J. I. Bluhm, "Fracture Arrest," pp. 1–64 in *Fracture, An Advanced Treatise*, ed. by H. Liebowitz, Academic Press, New York, 1968.

42. J. G. Merkle, "Crack-Arrest Concepts," in *HSST Quarterly Progress Report for October–December 1974*, ORNL/TM-4805, Vol. II, pp. 19–21.

43. R. G. Hoagland et al., *Rectangular-DCB Specimens for Fast Fracture and Crack Arrest Measurements*, BMI-1933, Battelle Memorial Institute (December 1974).

44. G. R. Irwin et al., *A Photoelastic Study of the Dynamic Fracture Behavior of Homalite 100*, NUREG-75/107, Nuclear Regulatory Commission (September 1975).

45. G. C. Sih, G. T. Embley, and R. S. Ravera, "Impact Response of a Thin Crack in Plane Extension," *Int. J. Solids Structures* 8, 977–93 (1972).

46. W. R. Delameter, G. Herrman, and D. M. Barnett, "Weakening of an Elastic Solid by a Rectangular Array of Cracks," *Trans. ASME, Ser. E, J. Appl. Mech.* 42, 74–80 (March 1975).

47. F. J. Witt and T. R. Mager, "Fracture Toughness, K_{Icd}, Values at Temperatures up to 550°F for ASTM A533, Grade B, Class 1 Steel," *Nucl. Eng. Des.* 7(1), 91–102 (August 1971).

48. F. J. Witt and T. R. Mager, *A Procedure for Determining Bounding Values on Fracture Toughness, K_{Icd}, at Any Temperature*, ORNL/TM-3894 (October 1972).

49. *PVRC/MPC Task Group on Fracture Toughness Properties of Nuclear Components – Final Report*, pp. 157–98, Welding Research Council (1977).

NUREG/CR-0126
ORNL/NUREG/TM-196
Dist. Category R5

Internal Distribution

1. R. G. Berggren
2. S. E. Bolt
3. R. H. Bryan
4. J. H. Butler
5. J. P. Callahan
6. D. A. Canonico
7. R. D. Cheverton
8. J. M. Corum
9. W. B. Cottrell
10. M. H. Fontana
11. W. L. Greenstreet
12. R. C. Gwaltney
13-17. P. P. Holz
18. H. W. Hoffman
19. S. K. Iskander
20. K. K. Klindt
21. Milton Levenson
22. R. E. MacPherson
23. J. R. McGuffey
24. J. G. Merkle
25. C. A. Mills
26. S. E. Moore
27. F. R. Mynatt
28. H. A. Pohto (Y-12)
29. G. C. Robinson
30. C. D. St. Onge (Y-12)
31. Myrtleen Sheldon
32. G. M. Slaughter
33. J. E. Smith
34. I. Spiewak
35. W. J. Stelzman
36. D. G. Thomas
37. H. E. Trammell
38. J. R. Weir, Jr.
39-40. G. D. Whitman
41. Patent Office
42-43. Central Research Library
44. Y-12 Document Reference Section
45-47. Laboratory Records Department
48. Laboratory Records, RC

External Distribution

49. C. Z. Serpan, RSR, Nuclear Regulatory Commission, Washington, D.C. 20555
50. Director, Research and Technical Support Division, Department of Energy, Oak Ridge Operations Office
51-110. Special ORNL distribution (by NRC)
111-268. Special HSST distribution (by NRC)
269-563. Given distribution under category R5 (25 copies — NTIS)

U.S. GOVERNMENT PRINTING OFFICE : 1977-748-189/252